ON EXPLOSIONS OF EXTENDED STARS AS TYPE I SUPERNOVAE

by

© WILLIAM THOMAS GRAHAM GLEN

A Thesis

Submitted to the School of Graduate Studies

in Partial Fulfilment of the Requirements

for the Degree

Doctor of Philosophy

McMaster University

August, 1985

MODELS FOR TYPE I SUPERNOVAE

DOCTOR OF PHILOSOPHY (1985)
(Physics)

McMASTER UNIVERSITY
Hamilton, Ontario

TITLE: On Explosions of Extended Stars as Type I Supernovae

AUTHOR: William Thomas Graham Glen, B.Sc., 1977 (McGill)
M.Sc., 1979 (McMaster)

SUPERVISOR: Dr. P. G. Sutherland

NUMBER OF PAGES: viii, 164

ABSTRACT

Despite great theoretical progress the nature of the progenitors of Type I supernovae is still in doubt. In recent years much attention has been focussed on accreting white dwarf models. This thesis examines another class of possible progenitors: extended helium stars. The computer code BOMB was written to hydrodynamically evolve the models.

A total of seventeen models are examined. Five of them resemble R Cor Bor stars which are hydrogen-deficient pulsational variables of roughly 1.5 - 2.0 $M_\odot$ named after the archetype R Corona Borealis. Ten other models are variations on these, used to explore the parameter space of possible models. The remaining two models are of the bare white dwarf type which constitute the current orthodoxy in the field.

It is found that the R Cor Bor stars are not viable as Type I supernova progenitors. The bare white dwarf models fit the available data better than do any of the envelope models, although stars with relatively small, low-mass envelopes could also provide reasonable fits.

ACKNOWLEDGEMENTS

I would like to thank my supervisor Dr. Peter Sutherland for guiding my researches these past few years and for financial support along the way.

I also thank the members (and de facto members) of the theory group for providing a congenial atmosphere for my studies at McMaster, particularly David Jeffery and Roger Patterson.

I am also grateful to the Natural Sciences and Engineering Research Council of Canada, the Ontario Government, and McMaster University for financial support.

Finally, I would like to thank Helen Kennelly for typing the bulk of this thesis and to Cheryl McCallion for kindly finishing it off.

TABLE OF CONTENTS

LIST OF FIGURES

CHAPTER I

OBSERVATIONAL BACKGROUND

Introduction

A supernova is literally a very bright new star. It is a rare, ephemeral, but spectacular event. Rarity is of course relative: throughout the universe supernovae occur at a rate of perhaps one per second; of these about ten per year are currently detected, but only about five per millenium are visible to the naked eye. On an astronomical scale a supernova is certainly ephemeral, rising to maximum brightness in a fortnight and fading over a period of months. A supernova is certainly spectacular; at maximum its luminosity may rival the output of an entire galaxy (i.e. $\sim 10^{10}\ L_{\odot}$), most of which is radiated in the visible spectrum. As seen from Earth, the supernova of A.D. 1006 was nearly as bright as the full moon (Clark and Stephenson, 1982).

Despite its name, a supernova is not actually a 'new' star. It merely appears so because its progenitor is generally too distant and too faint to be seen. Recent investigations have shown that a supernova results from a cataclysmic explosion of an old star at the end of its life. Yet despite a proliferation of both observational and theoretical results in recent years there remain many unresolved questions about both the progenitors and the resultant explosions.

Understanding supernovae is a central problem in modern astrophysics. Supernovae play a prominent role in the chemical evolution of the universe, enriching the interstellar medium with heavy elements (from carbon on up-

wards) which may later be incorporated into new stars and planets. Supernovae produce shock waves in the interstellar medium which are thought to trigger star formation. Supernovae are of interest to the physicist as 'laboratories' where theories may be tested under conditions not reproducible on Earth. Finally, supernovae have intrinsic interest; we see them but do not yet fully understand them.

Although it is widely acknowledged that supernovae come from relatively old stars (i.e. ones that have processed most of their nuclear fuel), little else is known for certain about the progenitors. As supernova progenitors have not been directly observed, their nature must be inferred from the observed properties of supernovae. This thesis attempts to shed some light in this direction. To this end a computer code has been developed to follow hydrodynamically the evolution of supernovae. A selection of feasible progenitors was chosen and the characteristics of the resultant explosions were calculated. Comparison of these models to observations permits certain conclusions about the nature of the progenitors to be drawn.

Historical Perspective

Mankind has long shown interest in observing and mapping the heavens, and various civilizations have left written accounts of transient astrophysical phenomena. The Chinese records are the most extensive, comprising a synopsis of naked-eye sky surveys over the last two millenia. The records recount innumerable 'new stars', the vast majority of which were comets, as evidenced by their proper motion. Of these new stars only seventy-five can be classified as novae, perhaps seven or eight of these

as supernovae (Clark and Stephenson, 1982). The most recent of these so-called 'historical supernovae' was seen in A.D. 1604, tantalizingly close (but prior) to the invention of the telescope. All of the historical supernovae occurred in a sector comprising about one-eighth of the Galaxy (Tamann, 1982), extinction rendering the (supposed) supernovae outside this sector too faint to be noticed.

The development of the telescope had a singular lack of effect on supernova astronomy for nearly three hundred years. The first record of an extragalactic supernova didn't come until 1885, when a rather bright one (of seventh magnitude) was seen in the Andromeda galaxy. Several more examples followed over the next forty years, but because the 'spiral nebulae' in which they occurred were thought to be relatively nearby objects within the Galaxy, these supernovae were mis-classified as ordinary novae. The distinction between novae and supernovae followed the establishment of the extragalactic distance scale by Hubble in the late 1920s and was quantified by Baade and Zwicky (1934). The 1930s marked the dawn of extragalactic supernova astronomy. With the aid of periodic sky surveys new supernovae have been discovered steadily since then, at a rate of roughly ten per year. Nearly five hundred supernovae have now been observed (Barbon,1980), along with a few hundred supernova remnants (discussed later in this chapter).

On the other hand Galactic supernovae have proven to be exceptionally elusive. None have been seen for more than three hundred years. One supernova remnant has been found (Cas A) which has been dated circa 1667

by kinematic extrapolation. Judging from its distance ($\sim$ 3 kpc) Cas A should have been readily visible at the time, perhaps even the brightest star in the sky, if it had a typical supernova luminosity. No report of such an event exists, leading to speculation that Cas A might be an example of a 'dark', or very underluminous supernova. Recently a report of a new star seen in 1680 near the position of Cas A has come to light (Ashworth, 1980). This new star (of sixth magnitude) has been identified with the supernova despite a small discrepancy in the reported position. There are certain selection effects responsible for the paucity of Galactic supernova observations. A major difficulty is the obscuration of Galactic supernova by dust and gas, which blocks out our view of most of the Galactic disk. This problem of obscuration is such that at visible wavelengths more detail can be seen of distant galaxies than of most of our own galaxy, despite the greater distances. Another factor is our internal perspective of the Galaxy; extensive sky surveys are needed to cover it, hence potentially detectable supernovae may be missed. This is not a problem with other galaxies, which may be quickly scanned in their entirety. Although Galactic supernova have thus proven elusive, a number of Galactic supernova remnants have been detected (mainly by radio astronomy) and are discussed further in a later section.

Nomenclature

Originally supernovae were named according to either the galaxy or the constellation in which they appeared. In the 1930s catalogues were compiled in which the supernovae were enumerated chronologically; these were periodically updated. However, such a system eventually

proved unworkable as supernovae were often discovered long after their occurrence by searches of old photographic plates. The present system of nomenclature was proposed by Zwicky et al (1963) to alleviate this problem.

Under the current system each supernova's name consists of a year followed by a letter (or two). The year corresponds to the time of maximum light and the letter reflects the order of discovery, rather than the order of occurrence. Thus for example the bright supernova seen in 1937 in the galaxy IC 4182, being the third discovered which occurred in that year, is named 1937c, or SN 1937c . For years which contain only one known supernova the letter is sometimes dropped: hence SN 1572 represents Tycho's supernova.

It is not practical to use separate systems of nomenclature for Type I and Type II supernovae as only a minority of all supernovae have been distinguished as such. Also, classification as to type is somewhat subjective and is therefore not a reliable basis for the objective task of assigning names.

Spectra

The bifurcation of supernovae into Types I and II was proposed by Minkowski (1941) and is now universally acknowledged to have a physical basis. The distinction is based on spectral features. Type I supernovae (SN I) are recognized by their similarity to the spectrum of SN 1937c, which serves as a standard. More recently SN 1972e has also been used as a standard as its spectrum is remarkably similar to that of 1937c and has been measured in greater detail. The most notable feature

of the Type I spectrum is the weakness (or complete lack) of the hydrogen Balmer lines (Minkowski, 1941). Conversely, Type II supernovae are characterized by strong hydrogen Balmer lines. The progenitors of SN I and SN II are believed to be quite distinct from each other in both mass and composition (see Chapter II for more detail). This thesis focuses on models for Type I supernovae; thus most of the data presented below is specific to SN I. When mentioned, data for SN II is clearly labelled as such.

Periodically suggestions have been made that certain supernovae fit neither class, but constitute separate classes. Due to a dearth of data this question is still under debate.

Estimates of the amount of hydrogen present in SN I have varied widely (see Kirshner et al, 1973; Kirshner and Oke, 1975; Branch and Tull, 1979). Current opinion is that very little (if any) hydrogen is present (see Wheeler, 1981; papers in Rees and Stoneham, 1982). The recent creation of synthetic spectra (without hydrogen) which closely resemble Type I spectra supports this view (Branch, 1982).

Near maximum light most of the energy in the SN I spectrum is carried in an optical continuum on which are superimposed broad spectral lines. Branch (1982) fit the spectrum of SN 1981b at maximum light to a colour temperature of 17,000±3000 K. But Branch also sounds a note of caution with this estimate: the lines of Si III and O II are weaker respectively than the lines of Si II and O I, indicative of a lower temperature or else a violation of LTE. The continuum reddens steadily for four to five weeks after maximum light by which time the colour tem-

perature has fallen to about 7000 K. After this the colour slowly moves back toward the blue but by this time most of the luminosity comes from the line emission above the photosphere (Branch et al , 1983).

Despite the approximate blackbody shape of the spectrum in visible light, significant deviations do occur. The most notable is the paucity of flux in the ultraviolet (Minkowski, 1938; Holm, Wu and Caldwell, 1974; Branch et al, 1983). A blackbody at 17,000 K would radiate $\sim$ 80% of its luminosity in the ultraviolet (i.e. below 4000 Å). If Branch's temperature estimate is correct then the ultraviolet deficiency is an extremely pronounced effect. Another region of deficiency is in the near infrared (Kirshner et al, 1973). No radio frequency signals from SN I near maximum light have yet been detected (Weiler et al, 1982), but significant radio emission is seen to start several months after the explosion in some cases. Early time observations at X-ray and gamma-ray frequencies would be very useful for constraining SN I models, but so far such observations have not been made.

The spectral lines superimposed on the continuum show a characteristic P Cygni shape (Branch, 1980a). The P Cygni shape consists of a Doppler-broadened emission band with a blueshifted absorption band. Branch (1981; 1982) has identified most of the spectral features: near maximum light calcium, silicon, sulphur, magnesium, and oxygen are seen in roughly solar proportions moving at $\sim$ 11,000 - 12,000 km-s^{-1}; one to two months later calcium, sodium, silicon, and iron are seen moving at 8000 km-s^{-1} and faster, also iron and cobalt are seen moving at $\leq$ 8000 km-s^{-1}. The identification of these elements is evidence for incomplete

nuclear burning, an important constraint which rules out several previously proposed models (see Chapter II). The velocities provide constraints on the explosion energy and on the photospheric radius and indirectly on the Hubble constant (Branch, 1982).

As indicated above the spectrum evolves during the course of the supernova. Thus even a single spectrum from a new event allows its age to be estimated without the necessity of accumulating data on the light curve.

As a class, Type I supernovae show strikingly little variation in their spectra. Some exceptions exist, for example SN 1962A and SN 1964A which are silicon deficient (Branch, 1980b) but otherwise look like standard SN I. The uniformity of the 'fingerprints' of standard SN I argues for a common progenitor with uniquely defined features (such as mass). The unusual SN I may arise from distinct, yet also fairly uniform progenitor classes which are just statistically rarer than the standard Type I progenitor. Plausible SN I models which are close to, but not quite the standard SN I may actually be valid models for some of these unusual supernovae. Nevertheless the attention of theorists is naturally focussed on determining the correct progenitor of the standard Type I supernova.

Light Curves

The light curve is the graphical representation of luminosity versus time. Most commonly the luminosity is measured in stellar magnitudes, which is a logarithmic scale, inherited from antiquity. Either monochromatic (i.e. narrow bandwidth) or bolometric (integrated over all wavelengths) luminosity may be used. Typically, measured light curves are

monochromatic whereas theoretically calculated light curves are bolometric and hence must be converted to allow comparison. This would be straightforward if the spectrum were truly blackbody but such is not the case. A commonly used prescription is to assume the spectrum is blackbody down to a cutoff wavelength of say 4000 Å, below which there is negligible flux. The most commonly used wavelength for monochromatic light curves is the blue band centered on 4400 Å.

The light curve rises to a maximum in about 15 ± 2 days (Pskovskii, 1977). On average the absolute blue magnitude peaks at

$$M_B = -19.73 + 5 \log (H/50) \qquad (1.1)$$

where H is the Hubble constant in units of km-s^{-1}-Mpc^{-1} (Sandage and Tammann, 1982). This corresponds to an output of roughly 2×10^{43} erg-s^{-1} at maximum. After maximum the luminosity drops by $\sim$ 2.7 magnitudes in the next thirty days (Barbon et al, 1973), followed by an exponentially decaying tail with half-life $\sim$ 55 days which lasts at least two years (Kirshner and Oke, 1975).

The Hubble constant enters equation (1.1) through the distance modulus. Estimates of the Hubble constant based on the interpretation of supernova observations favour a value near H = 50 km-s^{-1}-Mpc^{-1} (Branch, 1985). (Branch argues that the value of H = 100 km-s^{-1}-Mpc^{-1} favoured by certain astronomers is incompatible with completely disrupting white dwarf models for SN I, such as the models considered in this thesis.)

The light curve can be summarized as being comprised of a 'hump' followed by a 'tail'. The transition point from hump to tail occurs about

thirty days after maximum light and is significant for several reasons. It coincides with the peak of the colour curve: the star is bluer both before and after this point. Also, according to Branch (1982) this roughly coincides with the maximum of the photospheric radius. It is likely that these points are not just coincidental but mark a shift in the predominant radiative transfer processes. During the tail phase much of the gamma-ray energy is deposited above the photosphere (in an optically thin environment) and hence is not completely thermalized. (Such processes are not considered by the computer code developed for this work, so the calculations are terminated close to the hump-tail transition).

As-is true for their spectra, the light curves of SN I are fairly homogeneous and are quite distinctive. Strictly speaking, supernovae types are distinguished by their spectra, but light curves have also been so used when spectra were not available. In this fashion both SN 1572 and SN 1604 have been classified as Type I events from the shape of their light curves (Baade, 1943; 1945). Despite the aforementioned homogeneity, Barbon et al (1973) proposed dividing SN I light curves into two classes labelled 'fast' and 'slow'. The fast supernovae have relatively narrower peaks and greater drops in luminosity prior to the exponential tails than do slow supernovae. Pskovskii (1977) tried to quantify this distinction by introducing a parameter which reflects the slope of the light curve as it declines from maximum. He finds (as does Branch, 1982) that the slow group tends to have higher photospheric velocities than does

the fast group. Also (Branch, 1982) the slow group seems to be intrinsically brighter than the fast group. If in fact SN I (or subgroups thereof) are not all identical but show a range of characteristics, then their usefulness as standard candles for establishing extragalactic distances would be undermined. Tammann (1982) argues that the Pskovskii-Branch correlations are not statistically significant and that in fact all SN I are identical within errors of measurement. Even if the Pskovskii-Branch correlations are significant it is not clear from the data (Branch, 1982) that a strict bifurcation into fast and slow types is possible.

Remnants

The distinction between a supernova and a supernova remnant (SNR) is not sharply drawn; the former eventually evolves into the latter. Supernovae are pointlike sources which emit predominantly in the visible spectrum whereas remnants are extended sources which are relatively weak optically and are most prominent at radio or X-ray frequencies. The study of SNRs involves both the physics of the supernova explosion and the properties of the interstellar medium. The mass, composition, and kinematics of SNRs provide constraints for theoretical models of supernovae. Statistics on the number and distribution of SNRs help determine the overall supernova rate and may provide insight into the nature of the progenitors. This is discussed in detail in the section on rates and distribution.

With the exception of the Crab nebula, SNRs remained undetected until the advent of radio astronomy. At present about 130 Galactic radio

SNRs are known (Blair,1982), but relatively few extragalactic ones. Typically the radio emission is non-thermal and shows polarization (Blandford,1982). Radio SNRs are relatively easy to identify but the lack of spectral lines limits the information obtainable from them.

Optical emission from filaments has been detected from about one quarter of the radio SNRs (Blair, 1982). Qualitative information about composition is easily obtained from the spectral data but quantitative estimates of abundances are fraught with uncertainties. Lines of oxygen, nitrogen, neon, argon, and sulphur have been seen in putative Type II remnants (Dopita, 1982). On the other hand the remnants of SN 1572 and SN 1006 show only the hydrogen Balmer lines (Dopita, 1982); this is ironic as there is reason to believe (from the light curves) that these were Type I events. This hydrogen was presumably swept up from the interstellar medium and was shock heated. Estimates of the initial explosion energy of various remnants give results of the order of 10^{51} ergs (with large scatter) both from Sedov theory and from estimates of the internal energy (Blair, 1982).

Great advances in X-ray astronomy were made with the advent of the Einstein Observatory. Roughly forty Galactic SNRs have been observed with it (Seward; 1982) and many extragalactic sources as well (Helfand and Long, 1982). Observations made with the Solid State Spectrometer (SSS) on the Einstein Observatory show evidence of silicon, sulphur, argon, calcium, iron, and magnesium in most remnants. When normalized to silicon, the latter two elements are significantly underabundant relative to solar

abundances, whereas the other three are overabundant (Becker et al, 1980). This is discrepant with theoretical models of SN I which overproduce iron (Wheeler, 1982). However, the assumption of ionization equilibrium used to determine the abundances in SNRs is dubious; the Fe/Si ratio in the remnant of SN 1572 determined using the proportional counter on the Einstein Observatory differs by a factor of ten from the same ratio determined from the SSS data (Szymkowiak, 1980). The SSS data has been re-interpreted by Shull (1982) who considered nonionization equilibrium effects. His results show that magnesium, calcium, argon, and iron are present in roughly solar abundances relative to each other, with the silicon and sulfur abundances somewhat higher. The Fe/Si ratio agrees with the proportional counter estimate. Shull's results support Branch's identification of intermediate mass elements in the visible spectrum. This implies that nuclear burning during supernova ignition does not go to completion throughout the star.

In determining the mass range for supernova progenitors it helps to consider the estimated masses of the historical SNRs. The mass of Cas A is at least 10 $M_\odot$ (Wheeler, 1981), which is consistent with it being an underluminous Type II event. The estimated mass of SN 1572 is 0.9-2.8 $M_\odot$ (Dopita, 1982) and it is identified as a Type I event from its light curve (Baade, 1943), which supports the hypothesis that SN I have progenitors of relatively low mass. The Crab progenitor mass is estimated at 8 $M_\odot$ (Davidson, 1982) and contains a pulsar, which are both consistent with current Type II models, although the data on the light curve are insufficient to determine the Type.

The existence of the Crab pulsar highlights an interesting point. Pulsars are now firmly identified as neutron stars. Baade and Zwicky (1934) predicted that neutron stars could be formed in supernovae. Theory now suggests that SN II always produce neutron stars (or black holes) whereas SN I never do. To test this hypothesis various SNRs have been searched for both pulsars and also thermal radiation from neutron stars or pulsars not beamed at Earth. The data collected so far (Shapiro and Teukolsky, 1983) show no definite pointlike thermal emission at temperatures down to $\sim$ 1-2x10^6 K, although some faint interpulse emission was seen in the Crab and Vela pulsars (Harnden et al, 1979a;b). Neutron star cooling calculations (Glen and Sutherland, 1980; Van Riper and Lamb, 1981; Nomoto and Tsuruta, 1981) show that SN 1006 cannot contain a neutron star if standard cooling processes apply. The Tycho and Cas A remnants are marginal cases, but the data suggest no neutron stars are present. These results unfortunately are open to more than one interpretation: either no neutron stars are present, or the surface emission is non-thermal (due to strong magnetic fields), or else exotic cooling mechanisms are at work (due to pion condensates or quark matter). As Tycho's supernova (SN 1572) and SN 1006 have been identified as SN I the results are not surprising; the exploding white dwarf models for SN I do not create neutron stars. The case of Cas A is not so clear as it is (tentatively) identified as a Type II event. Both further observations and more stringent theoretical limits are needed to make an unequivocal statement on Cas A in particular and on the presence of neutron stars in SNRs in general.

Rates and Distribution

With sufficient statistics on the rates and distribution of supernovae it should be possible to determine the nature of their progenitors. The data for SN II are fairly consistent with their being young massive stars, but the situation for SN I is less clear. The fact that SN I occur in elliptical galaxies where star formation has (or is thought to have) ceased (Tammann, 1982) has led to the belief that their progenitors are old, low mass stars. Confirming this is the observation of Maza and van den Bergh (1976) that SN I in spiral galaxies are not concentrated in spiral arms where active star formation takes place. The implication is that their lifetimes exceed 3×10^7 years, hence the progenitors had an original mass $\leq 6\ M_\odot$ (Biermann and Tinsley, 1974). On the other hand Oemler and Tinsley (1979) argue that the SN I rate is correlated to the star formation rate which suggests that the progenitors may come from a relatively young population (i.e. perhaps $\leq 10^9$ years, or $\geq 2\ M_\odot$). Furthermore, SN I are not halo objects as they are concentrated near the disks in spiral galaxies (Tammann, 1982). Thus they come from an intermediate age or old disk population (and also from the population found in elliptical galaxies).

An important clue into the nature of supernova progenitors is their overall rate of occurrence. Tammann (1982) has calculated a Galactic frequency of 0.050 SN per year, composed of partial rates of 0.027 SN I per year and 0.023 SN II per year. Lyne (1982) has calculated the Galactic pulsar formation rate at 0.02-0.05 yr^{-1}. This range is consistent (barely) with the assumptions that all pulsars come from SN II and all

SN II result in pulsars. This is consistent with both the exploding white dwarf models for SN I (which do not leave central remnants) and the non-detection of any neutron stars associated with Type I remnants. Unfortunately there are other possibilities. Some fraction of neutron stars and pulsars may be formed in events not classified as supernova (say, an event with a relatively low optical luminosity), and it is possible that some SN II produce black holes, rather than neutron stars. Thus the conclusion that SN I do not result in neutron stars is not iron-clad.

The above data on the Galactic supernova rate are based on observations of current supernovae. Alternatively one may use the number of SNRs observable to estimate this rate. From their X-ray search of the Large Magellanic Cloud (LMC), Helfand and Long (1982) found roughly fifty SNRs. They translate this into a SN rate of 1 per 110 to 350 years, which is in agreement with the rate of 1 per 268 years for the LMC calculated by Tammann (1982). The data on SN II rates provide a lower bound on the SN II progenitor masses. The SN I rates tell rather less about the SN I progenitors as only a fraction of the stars in the appropriate mass range ($\sim$ 2-6 $M_\odot$) are needed to produce the observed SN I rate. The SN I rates are however relevant to the calculation of Galactic iron production.

Supernovae play a crucial role in the chemical evolution of the universe. The big bang theory restricts the initial chemical composition of stars to be essentially just hydrogen and helium; other elements are formed in stellar interiors and released through supernovae. Of particular interest to SN I calculations is the production of ^{56}Fe, which is

the most tightly bound nucleus in nature and which accounts for $\sim$ 0.1% of the matter in the Galaxy. As SN II are not thought to eject much iron, this iron abundance is thought to have accrued solely through ejection from SN I. The models examined in Chapter II typically produce 0.5-1.4 $M_\odot$ of ^{56}Ni per event, which beta decays to iron via

$$^{56}Ni \rightarrow {}^{56}Co \rightarrow {}^{56}Fe \quad . \qquad (1.2)$$

However, from the SN I rate and the estimated Galactic iron content the allowed production of ^{56}Fe is only 0.3 $M_\odot$ per SN I, within perhaps a factor of three (Tinsley, 1980; Twarog and Wheeler, 1982). This amount would be raised somewhat if the Galaxy is losing a significant fraction of its iron to the intergalactic medium. The most recent models for SN I produce less iron ($\sim$ 0.5-0.8 $M_\odot$) than do the earlier models (typically 1.0-1.4 $M_\odot$), which to a large extent mitigates the iron overproduction problem.

Summary

The remarkable homogeneity of SN I (compared to SN II, say) suggests that their progenitors are rather uniquely defined. White dwarf stars near the Chandrasekhar mass provide such a population, as first suggested by Schatzman (1963). White dwarf progenitors are also indicated by the constraints on the original stellar mass (i.e. $\sim$ 2-6 $M_\odot$); stars in this range usually evolve into white dwarfs (Wheeler, 1981). (Note that this mass range represents the initial mass of the progenitor. At the time of supernova ignition the star may have lost an appreciable fraction of this mass either as a stellar wind or by accretion onto a binary companion.)

SN I do not appear to form neutron stars, although the data are not conclusive in this regard.

At maximum light the material at the photosphere is of roughly solar composition (apart from the lack of hydrogen), and moves outward at $\sim$ 11,000 km-s^{-1}. Several weeks later slower ($\lesssim$ 8,000 km-s^{-1}) iron and cobalt are seen as well.

Estimates of the Galactic iron abundance favour a relatively small output of ^{56}Fe (i.e. $<<$ 1 $M_\odot$). So do the observations of low iron abundance in SN I remnants. On the other hand the light curve suggests the presence of at least 0.3 $M_\odot$ of iron. So do the estimates of the kinetic energy of the ejecta (if this energy derives from nucleosynthesis).

The light curve consists of a hump followed by a tail. The hump rises to maximum light ($M_B \simeq -19.7$) in $\sim$ 15 days and then falls somewhat less steeply. The exponential tail (half-life $\sim$ 55 days) starts about 30 days after maximum light.

This concludes the review of the observational constraints applicable to models of Type I supernovae. In the next chapter we pass to a review of past progress of such theoretical models.

CHAPTER II

THEORETICAL WORK ON SUPERNOVAE

Degenerate Cores

Matter at high density ($\rho > 50\ T_6^{2/3}$ g-cm^{-3}, where T_6 is the temperature in millions of degrees Kelvin) is supported primarily by the pressure of degenerate electrons. Stellar evolution calculations indicate that degenerate cores form at the centre of certain stars. A white dwarf is an example of such a degenerate core in isolation.

One of the most important advances in theoretical astrophysics was the realization that such degenerate cores have a maximum mass (Chandrasekhar, 1931) above which collapse occurs. This limit is

$$M_{cr} = 5.6\ \mu_e^{-2}\ M_\odot\ , \qquad (2.1)$$

where μ_e is the ratio of the number of nucleons to the number of electrons. As a degenerate core approaches this mass the matter becomes highly compressible (the adiabatic index drops to 4/3) resulting in very high densities. For convenience such degenerate cores close to the Chandrasekhar mass are hereby referred to as 'critical cores'.

A critical core exists on the verge of instability and is essentially a disaster waiting to happen. Some of the possible fates which await it are detailed below.

The simplest fate is that further accretion of matter pushes the critical core over the Chandrasekhar mass whereupon it collapses to a

neutron star (releasing much gravitational binding energy in the process). The accreted matter may come from one of two possible sources: either a diffuse envelope surrounding the core (as is possible with red giant stars), or from a binary companion star (if the orbit brings them sufficiently close together to permit significant mass transfer).

As the mass of a degenerate core is increased the density increases and hence so does the electron Fermi momentum. At high enough density the nuclei may become susceptible to electron capture. Electron capture will raise μ_e and hence lower the Chandrasekhar mass, again causing collapse to a neutron star. (This is the triggering mechanism in current Type II models.)

If the critical core is composed of relatively light elements such as helium or carbon then the possibility of a thermonuclear runaway exists. If the matter is heated beyond $\sim 10^8$ K (for helium) or $\sim 10^9$ K (for carbon) the matter will ignite, resulting in either a detonation or a deflagration which consumes most of the core. (For details of these processes see the section on incineration mechanisms.) The explosive nature of this ignition led Hoyle and Fowler (1960) to suggest it as a viable supernova triggering mechanism. (Note that for pure helium, degenerate core ignition may occur at the relatively low mass of 0.7 $M_\odot$ (Chevalier, 1981). The definition of critical cores must be stretched somewhat to include this particular case.)

Even if there is an efficient cooling mechanism that prevents the requisite ignition temperatures from being reached, both helium and carbon will ignite due to pycnonuclear reactions if sufficiently compressed (see

Salpeter and Van Horn, 1969). For carbon this density is $\sim 3\times10^{9}$ g-cm^{-3} (Nomoto, 1984). (Earlier estimates of the pycnonuclear carbon ignition density were significantly larger, $\sim 10^{10}$ g-cm^{-3}). The results of this process are similar to those of thermonuclear runaway as mentioned above.

The motivation for defining critical cores is primarily to draw attention to the similarities exhibited by all putative supernova progenitors, be they compact (like white dwarfs) or extended (like the helium stars). Virtually all supernova models utilise critical cores as their ultimate energy sources. The connection between cores and supernovae is reciprocal: not only are critical cores the only practical source of supernova-scale energies ($\sim 10^{51}$ ergs), but a supernova-scale catastrophe is almost inevitable once a critical core has formed.

Energetics

From the details in the previous chapter the energetics of SN I may be quantitatively studied. There are three phases in a Type I supernova which require (possibly distinct) sources of energy. The first is the kinetic energy of the explosion itself, in which $\sim 10^{33}$ g of matter are accelerated to an average velocity near 10^{9} cm-s^{-1}, requiring $\sim 10^{51}$ ergs to be released. The second phase is the hump of the light curve, in which a luminosity averaging 10^{43} ergs-s^{-1} is maintained for $\sim 10^{6}$ s, requiring $\sim 10^{49}$ ergs of energy to be radiated over this time. The third phase is the exponential tail of the light curve, during which a further $\sim 10^{49}$ ergs is radiated over a period of many months. These phases are discussed in turn.

The kinetic energy given to the disrupting star ($\geq 10^{51}$ ergs) represents $\sim$0.1% of the total rest-mass energy of the star. Only two sour-

ces of this much energy are available: one is the gravitational energy released in forming a neutron star, and the other is the nearly instantaneous release of the remaining nuclear fusion energy. (A third potential source of the requisite energy is from the collision of two stars. This hypothesis is in disrepute since the calculated stellar collision rate is much lower than the observed supernova rate.) The starting point for both viable processes is a critical core as described in the previous section.

The former source (gravitational collapse) was suggested quite early on by Baade and Zwicky (1934). The detailed calculations of critical core collapse remained intractable until computers were developed to perform them numerically. The first such calculations were those of Colgate and White (1966) which involved a high density ($\rho > 10^{11}$ g-cm^{-3}) core which collapsed due to electron capture. Despite the plentitude of energy available ($\sim 10^{53}$ ergs) it was not clear how to transfer the necessary 1% of it to the outer layers (which were ejected). Colgate and White proposed that neutrinos effected this transfer. However, the physics of neutrino interactions was not well understood at the time and has undergone revision since the discovery of neutral currents in the 1970s. It is now believed that the neutrinos get trapped in the infalling core. In current models the energy transfer is effected by a hydrodynamical shock caused by the 'bounce' or rebound which happens when the infalling matter surpasses nuclear density (Brown, 1982; Bethe, 1982). These models are now used primarily for Type II supernovae.

As pointed out by Hoyle and Fowler (1960) thermonuclear runaway is a viable alternative to gravitational collapse. They proposed that the explosive burning of degenerate carbon, oxygen etc. would occur in critical cores prior to gravitational collapse. It is now believed that either thermonuclear or pycnonuclear runaway is inevitable prior to collapse in a critical core composed of low mass elements such as carbon and oxygen (see reviews by Mazurek and Wheeler, 1980; Sugimoto and Nomoto, 1980). The SN II models mentioned above bypass this state by burning their fuels before degeneracy sets in.

The incineration of the nuclear fuel provides an adequate energy source for the first phase of the supernova. But the peak of the light curve occurs about fifteen days later, when the radius of the nebula exceeds 10^{15} cm. If the progenitor was compact (initial radius $\lesssim 10^{9}$ cm) then cooling due to adiabatic expansion would be extremely rapid. In lieu of other energy sources the light curve would fade out in a matter of hours. There are two possible ways around this problem: first, late time energy input from radioactive decays; and second, the progenitor could be extended rather than compact (i.e. initial radius $\gtrsim 10^{13}$ cm). Lasher (1975, 1980) has shown the viability of the latter possibility, but in the last five years great success has accrued to models invoking the radioactive decay of ^{56}Ni and its daughter ^{56}Co.

The cause of the exponential tail was not addressed in Lasher's extended models, but the tail is a natural consequence of the scenario of ^{56}Ni and ^{56}Co decay. The observed $\sim$ 55 day half-life of the tail initially misled researchers into looking for a decay scheme with such

a half-life, but recent calculations (Arnett, 1979; Axelrod, 1980; Colgate, Petschek and Kreise, 1980; Weaver, Axelrod and Woosley, 1980; Chevalier, 1981) show that the 78.8 day half-life of ^{56}Co is modulated to the observed $\sim$ 55 days by the increasing transparency of the nebula to gamma-rays.

Using the radioactive decay models one may attempt to determine the amount of ^{56}Ni required to power the hump (or the tail) of the observed light curves. However, there are three compounding sources of error in such an estimate. First, the measured apparent (monochromatic) magnitude of the supernova must be converted to an absolute magnitude using the Hubble law, but the Hubble constant is uncertain by at least 50%. Second, the bolometric magnitude is found by integrating the spectral profile. This also introduces error since the spectrum is not truly blackbody. Third, the efficiency of the conversion of the radioactive decay energy into thermal energy is uncertain; some fraction will escape the nebula as gamma-rays. As a result figures ranging from 0.2 $M_\odot$ to 1.4 $M_\odot$ (or more) of ^{56}Ni have been deemed acceptable for powering the light curve. For example Chevalier (1981) finds that 1.3 $(H/50)^{-2}$ $M_\odot$ of ^{56}Ni fits the peak of the light curve, but he assumed the spectrum to be blackbody. For a spectrum deficient in the ultraviolet this estimate could be significantly reduced (perhaps by as much as a factor of two or more).

As detailed in Chapter III the incineration of matter into nuclear statistical equilibrium inevitably produces ^{56}Ni. The real question is just how much of the critical core (up to 1.4 $M_\odot$) is so affected. Unfortunately the observations do not set stringent limits. Nevertheless,

two factors suggest that the actual ^{56}Ni production is probably less than 1 $M_\odot$ per event. The first is the estimate of the Galactic iron abundance, which implies a ^{56}Ni production of $\sim$ 0.3 $M_\odot$ per event (albeit with large error). The second follows from Chevalier's estimate (and similar ones); most astronomers believe $H \geq 50$ km-s^{-1}-Mpc^{-1}, so 1.3 $M_\odot$ becomes an upper bound. This value is reduced further by the truncated spectrum effect mentioned above. Thus, models which completely process their 1.4 $M_\odot$ cores to ^{56}Ni tend to be too bright. Furthermore they do not contain the intermediate mass elements (Si,S,Ca, etc.) identified in the SN I spectrum and they also show unacceptably high ejecta velocities (Wheeler, 1982).

Incineration Mechanisms

In all recent theoretical models of SN I the explosions are triggered by one of three processes: carbon detonation, carbon deflagration, or helium detonation. These processes all take place under the conditions of degeneracy and high density typical of critical cores.

The rate of nuclear burning (i.e. fusion) for carbon (or helium) increases with both temperature and density. There is a boundary (for each element) called the ignition line in the (ρ,T) plane, on which the energy generation rate equals the rate of energy loss by the various cooling mechanisms. When some region in the critical core crosses this line then the local temperature quickly rises. This then throws the energy production and cooling rates further out of balance, so a positive feedback is set up which drives up the temperature. If the matter was non-

degenerate then the pressure would rise with the temperature, causing the hot region to expand into its surroundings and cool, interrupting the feedback. This regulatory mechanism is absent if the matter is degenerate since then the pressure is (to first order) independent of temperature. Thus in degenerate matter a runaway ensues which continues until the degeneracy is lifted or the fuel is expended. In either case a great deal of thermal energy ($\sim 10^{18}$ ergs-g^{-1}) is deposited in the hot spot which creates some overpressure which propagates as a shock wave. As this shock wave travels through the unburned material it compresses and heats the matter, causing it to burn faster. If the newly shocked matter burns fast enough (burning time is less than the dynamical timescale) then the burning front is effectively coincident with the shock front and the process is called a detonation. The detonation will process all the available fuel into nuclear statistical equilibrium (NSE) before the core is disrupted. If on the other hand the shock is relatively weak then it will not drive the unburned matter into NSE, but eventually convective energy transport from the original hot spot may further heat the unburned material until it too is incinerated. This process is called a deflagration and is characterized by a subsonic burning front.

The case of detonation is relatively simple to calculate as the shock velocity (and hence the burning front velocity) is known, and the burning takes place before the core has expanded. Deflagration calculations are more uncertain; the velocity of the burning front (the deflagration velocity) must be specified in some manner (various prescriptions are given in Sutherland and Wheeler, 1984; Jeffery and Sutherland, 1985; and Nomoto, 1984). This is crucial because the burning front is

in competition with the expansion of the core which reduces the nuclear burning rate.

If the runaway is initiated at the base of the helium layer (as in the models of Nomoto, 1982a) then the detonation wave will propagate out through the rest of the helium. Depending on conditions a second detonation wave may propagate inward through the carbon-oxygen. Although such models produce reasonable light curves (Nomoto, 1982b) they are open to the objection that no intermediate mass elements (Si,S,Ca, etc.) are present as are identified in the spectra.

Alternatively the runaway may start in the carbon at the stellar centre. The early calculations on this problem (Arnett, 1969; Bruenn, 1972) assumed that such ignition would lead to a detonation. However, later calculations (Nomoto, 1984; Nomoto, Sugimoto and Neo, 1976; Ergma and Tutukov, 1976) show that the overpressure (and hence shock strength) from central carbon ignition is relatively weak and is not sufficient to create a detonation. Thus the current consensus is that central carbon ignition leads to carbon deflagration. (Note that the composition is assumed to be a mix of carbon and oxygen. As carbon has the smaller Coulomb barrier it ignites first, so the carbon ignition line is the crucial one. Once a carbon runaway occurs then the oxygen ignition line will also be crossed so both elements become incinerated.)

Whether it is the carbon or the helium which first reaches its ignition line may depend on the previous history of the critical core. For accreting white dwarf models the accretion rate is a crucial parameter in this regard. Fugimoto and Sugimoto (1982) and Fugimoto and

Taam (1982) have calculated the dependence of ignition type on the accretion rate. But it is not clear that both types of ignition actually occur in SN I, which show remarkable homogeneity as a class. As pointed out in the next section helium detonation models violate certain observational constraints and so may be much rarer than indicated by the above authors.

Progress of Theory

In this section the recent theoretical work on SN I is reviewed. The papers are discussed in roughly chronological order. At the end is a summary of pertinent results which provides the motivation for the models examined later in this work.

Arnett (1969) considered the evolution of stars in the range from 4 to 9 $M_\odot$, with critical carbon-oxygen cores. Central carbon ignition occurs which raises the temperature greatly but results in an overpressure of less than 3% (due to the degeneracy). It is demonstrated that if detonation is initiated then it will self-propagate resulting in complete core incineration to ^{56}Ni. The light curves were not explicitly calculated.

Colgate and McKee (1969) calculated the light curves resulting from ^{56}Ni decay in detail. They considered models of 2 $M_\odot$ and 10 $M_\odot$ respectively and used detailed opacity functions. (For reasons detailed in the next chapter the opacity is usually parametrized, as there are too many uncertainties to determine it exactly.) Colgate and McKee were the first to demonstrate numerically the viability of ^{56}Ni and ^{56}Co decay in explaining the late time light curve.

The essence of the radioactive decay model is that there is a delay in the release of some of the nuclear energy. Despite the prodigious amount of energy released at ignition ($\geq 10^{51}$ ergs), the star is very efficiently cooled by adiabatic expansion. The radioactive decay energy is released continually throughout the expansion and serves to reheat the matter. Typically about 10^{50} ergs are stored in ^{56}Ni nuclei for later release, a small amount compared to the explosion energy but large compared to visible light output ($\sim 10^{49}$ ergs). Some of the decay energy escapes the system but a fraction is trapped (deposited) and thermalized, and subsequently emitted as thermal radiation.

Whelan and Iben (1973) proposed the accreting white dwarf model to explain the existence of SN I in elliptical galaxies which no longer exhibit star formation. The model considers a carbon-oxygen white dwarf in a close binary system with a main sequence star. Such a system remains quiescent for a long time period until the main sequence star evolves to the giant phase whereupon it overfills its Roche lobe and transfers matter onto the white dwarf. The accreted matter is (or burns to) helium and eventually pushes the white dwarf up to a critical mass with a resultant supernova. This scenario is at present the most popular method of generating Type I supernovae.

Lasher (1975,1980) demonstrated the feasibility of extended progenitors for SN I. He made no attempt to utilise realistic stellar models and did not consider late-time heating by radioactive decay. His models had three adjustable parameters which were fitted to the hump of the SN I light curve. The best fitting model had $M = 2\ M_{\odot}$, $\rho = 10^{-8}$ g-cm^{-3}, and $E = 10^{51}$ ergs, and gave $M_B = -18.5$ at maximum, and v_{surf} =

1.0×10^{9} cm-s^{-1}. The mass of the progenitor and the energy released are plausible but the initial radius exceeded 3×10^{13} cm, which is exceptionally large for a star. It is quite possible, however, that the hump of the light curve is due to a combination of both radioactive decay and the effect of an extended progenitor.

Nomoto, Sugimoto and Neo (1976) argued that the assumption that carbon will detonate is incorrect. Their calculations show that the shock resulting from central carbon ignition is too weak to cause incineration, so burning must proceed by the slower process of deflagration. The deflagration velocity was quite uncertain so it was simply parametrized as a fraction of the sound speed (the fractions 1/5 and 1/100 being used explicitly in their calculations).

Weaver, Axelrod and Woosley (1980), and also Woosley, Weaver and Taam (1980) performed numerical calculations on accreting white dwarf models of various compositions. Two of their models had extended helium shells of radius $\sim 10^{11}$ cm surrounding the white dwarf, the remaining models were compact. The supernovae were triggered by (double) helium detonation which incinerated the cores entirely. The late-time light curve was powered by ^{56}Ni and ^{56}Co decay with the gamma-ray opacity taken to be 0.06 cm^{2}-g^{-1}. Overall the compact models give good fits to the light curve, the extended ones somewhat less so (the humps are not pronounced enough). The velocity profile of their Model A is too high, indicating excessive initial energy release. Even more serious difficulties are the creation of high-velocity nickel and the dearth of intermediate mass elements. The spectral fit of Model A is in rough agreement with

observations as both spectra are dominated by iron lines, but Model A's spectrum lacks certain notable features such as the calcium lines. In summary the models argue for the production of significant amounts of ^{56}Ni in SN I, but argue against complete core incineration.

Chevalier (1981) also calculated light curves for accreting white dwarf models with ^{56}Ni decay. He found (as above) that carbon detonation produced far too little of the intermediate mass elements, and what there was moved too fast ($\sim$ 30000 km-s^{-1}). The carbon deflagration model burnt 1.0 $M_\odot$ of the 1.4 $M_\odot$ core to ^{56}Ni, which was assumed to be mixed throughout the remnant. The opacity was taken to be 0.1 cm^2-g^{-1}. The models were compact. The density profile was taken to be constant in the interior and proportional to r^{-7} in the outer regions. Chevalier found that the peak of the light curve could be powered by 1.3 $(50/H)^2$ $M_\odot$ of ^{56}Ni. As noted earlier, this may be an overestimate since the spectrum is not blackbody.

Arnett (1982) used analytic models of SN I to study the hump of the light curve. Certain simplifying assumptions had to be made to reduce the problem to analytic form but nevertheless some interesting results were obtained. One is that the shape of the light curve depends on the value of his (opacity dependent) parameter 'y'. For a given progenitor mass and explosion energy it is possible to choose the opacity so that the peak of the light curve is correctly timed and the hump has the proper width. Another point is that (other things being equal) the initial progenitor radius only affects the light curve for the first twenty-five days or so. This means that the width of the hump is not

strongly dependent on the extent of the progenitor (but it does depend on the mass of the progenitor).

Schurmann (1983) calculated light curves for both compact and extended progenitors. No dynamics were included; the calculations start with an assumed density distribution (like Chevalier's) in a state of homologous expansion. The velocity at the core boundary was variously taken to be 9000 km-s^{-1} or 10000 km-s^{-1}, the (optical) opacity was taken to be 0.05 cm^2-g^{-1} or else 0.045 cm^2-g^{-1} (also some simple time-dependent opacities were used in certain models). The gamma-ray deposition was approximated by an analytic function. The convention of truncating the spectrum shortwards of 4000 Å was used to account for the observed paucity of ultraviolet flux. This has the effect of enhancing the hump of the light curve as seen in blue light. The observed light curves of SN 1972e and 1981b are well reproduced by these models but this is a result of a judicious choice of parameters. Both the compact and the extended models fit the observations.

Sutherland and Wheeler (1984) numerically followed the evolution of exploding carbon-oxygen-helium white dwarfs. The convention of truncating the spectrum at 4000 Å was adopted. The optical opacity was assumed constant at 0.1 cm^2-g^{-1} although their Model C investigated the effect of a spacially dependent opacity. The gamma-ray deposition was calculated numerically to take account of the non-uniform mass distribution. The gamma-ray opacity was taken to be 0.03 cm^2-g^{-1}. The models were all initially compact. As found in some of the earlier work the completely incinerated model (Model A) was too fast and too bright and failed

to contain the intermediate mass elements. The most promising models in terms of satisfying the observational constraints were B and C, in which 1.0 $M_\odot$ of the 1.4 $M_\odot$ star is burned to ^{56}Ni, similar to Chevalier's carbon deflagration model.

Nomoto (1984) performed numerical calculations on accreting white dwarfs up to the stage of carbon deflagration. He points out that even relatively cool white dwarfs will undergo pycnonuclear carbon ignition when the density reaches 3×10^9 g-cm^{-3}, a significantly smaller density than previously reported. This means that neutronization via electron capture is not likely to be very pronounced in SN I, as the density will never become large enough. The models still use a parametrized deflagration velocity. A detailed nuclear reaction network keeps track of the composition as burning proceeds. Typically 0.4-0.7 $M_\odot$ of ^{56}Ni is produced per event, along with a comparable amount of other iron-group and intermediate mass elements produced by partial burning as the deflagration wave dies out. This result is interesting because previously it was assumed that all incinerated matter burned to ^{56}Ni, so the kinetic energy released in the explosion was directly related to the late-time energy release. Also, this model satisfies many of the properties observed in SN I; at early times high velocity ($\gtrsim$ 10000 km-s^{-1}) calcium and silicon (for example) lines will be seen in the spectrum, while at later times slower moving iron and cobalt will be seen.

In summary the evidence favours carbon deflagration as the means of producing a Type I supernova. The observation of early time photospheric velocities near 12000 km-s^{-1} suggest that roughly 70% of the matter is

incinerated (as in Chevalier's deflagration model and in Sutherland and Wheeler's models B and C). On the other hand the nature of the progenitor is still uncertain. The calculations show that for the compact models (i.e. white dwarfs) radioactive decay can power both the hump and the tail of the light curve. Less work has been done on extended progenitors. The success of the radioactive decay models suggests that even for extended progenitors the bulk of hump's energy comes from radioactivity, but some fraction may nevertheless result from the initial mass distribution. The aim of this thesis is to examine the feasibility of extended SN I progenitors by performing detailed hydrodynamic calculations to determine their characteristics. Attention is given primarily to the light curves (both bolometric and blue) and the photospheric radius, velocity, and temperature (which determines the colour index).

CHAPTER III

THE CALCULATIONAL METHOD

The Hydrodynamical Equations

A star is best described in terms of macroscopic properties such as pressure, temperature, density, and entropy. These quantities are well defined in stars since they vary negligibly on the scale of the mean particle separation. After supernova ignition the particle interactions are insignificant and the material behaves as a fluid (at least until the temperature falls below a few thousand degrees when recombination and grain condensation may occur). The assumption of local thermodynamic equilibrium (LTE) allows the application of standard thermodynamic relations. The supernova thus becomes a problem in fluid dynamics.

For complete generality four independent coordinates are needed, three space coordinates and time. The assumption of spherical symmetry eliminates two coordinates, greatly simplifying the computations. Despite the apparent sphericity of the nearest star (the sun), in stellar modelling certain spherically asymmetric effects may be important: notably rotation, magnetic fields, and turbulence. Aspherical supernova calculations have only recently been attempted (Muller and Arnett, 1982; 1984) and require powerful computing capabilities. In the present work spherical symmetry is always assumed.

The remaining spatial coordinate may be chosen to be any monotonic function of the radius. The two common alternatives are the Eulerian sys-

tem (coordinates fixed in space) and the Lagrangian system (coordinates comoving with the matter). The Lagrangian system is the more convenient for this particular problem since the outer boundary (surface) of the supernova then remains fixed. Thus Lagrangian coordinates are used forthwith.

The independent spacial coordinate is 'm', defined by

$$m(r) = \int_0^r 4\pi(r')^2\rho(r')dr' \quad . \tag{3.1}$$

Thus the mass function 'm' at a point 'r' is just the amount of mass interior to 'r'. In keeping with the choice of m as the independent variable this equation may be re-expressed in the form

$$V \equiv \rho^{-1} = 4\pi r^2 \frac{\partial r}{\partial m} \quad , \tag{3.2}$$

which is the first of the hydrodynamic equations (the Continuity equation). 'V' is referred to as the proper volume.

The remaining equations are discussed in turn (for further detail see for example Falk and Arnett, 1977).

Velocity equation:

$$v = \frac{\partial r}{\partial t} \quad . \tag{3.3}$$

Momentum conservation:

$$\frac{\partial v}{\partial t} = -4\pi r^2 \frac{\partial P}{\partial m} - \frac{Gm}{r^2} \quad . \tag{3.4}$$

The only forces of note are the fluid pressure gradient and gravity.

. Energy conservation:

$$\frac{\partial E}{\partial t} + P \frac{\partial V}{\partial t} + \frac{\partial L}{\partial m} = \Sigma \quad . \tag{3.5}$$

Both the energy 'E' and the net energy sources 'Σ' are intensive variables, being measured per unit mass. The luminosity 'L' is an extensive variable (it is the total thermal radiation through a sphere of constant 'm'). The energy 'E' consists of the internal energy of the particle fluid and the thermal radiation field. Energy gained or lost locally through radioactivity, gamma-ray production or deposition, or neutrino production appears in the term 'Σ'.

Radiative diffusion

$$L' = -(4\pi r^2)^2 \frac{ac}{3\kappa} \frac{\partial T^4}{\partial m} \quad . \tag{3.6}$$

Radiative diffusion is a valid approximation if the photon mean free path is much less than the temperature scale height. Defining a dimensionless parameter 'x' by

$$x = \frac{4\pi r^2}{3\kappa T^4} \left| \frac{\partial T^4}{\partial m} \right| \quad . \tag{3.7}$$

then equation (3.6) is valid for $x << 1$. Since this condition is not always fulfilled in supernovae the luminosity is modified by the use of a flux limiter (Alme and Wilson, 1974):

$$L = L'[1+x+3x \cdot \exp(-3x/2)]^{-1} \quad . \tag{3.8}$$

By using this flux limiter it is possible to extend the use of the radiative diffusion equation (3.6) into optically thin environments.

Also needed is the equation of state specifying the pressure $P = P(\rho,T,\mu_e,\mu_i)$, the specific energy $E = E(\rho,T,\mu_e,\mu_i)$, and entropy $S = S(\rho,T,\mu_e,\mu_i)$. To complete the picture it is necessary to specify the opacity 'κ', the energy sources 'Σ', and the boundary conditions.

The essence of the problem is to solve equations (3.4) and (3.5) which are two coupled second order partial differential equations. (The other equations may be regarded as definitions.) This is done by approximating the hydrodynamic equations by finite difference equations.

The Finite Difference Equations

Finite difference equations have been in common use since the advent of computers (see e.g. Richtmeyer and Morton 1967; hereafter RM). The method entails evaluating the dependent variables only at certain discrete values (known as mesh points) of the independent variables. Derivatives are then approximated by secants taken between adjacent mesh points. Clearly, a denser mesh gives better estimates of the derivatives, but the price is an increase in computing cost. These two factors must be considered in determining the optimum mesh density.

It is not necessary for the mesh points to be evenly spaced in either variable (m or t). Nevertheless, for notational purposes the mesh points are always referred to by ordinal numbers. Subscripts refer to mass zone numbers whereas superscripts refer to time step numbers.

Defining the mass and time increments

$$\Delta t^{n+\frac{1}{2}} \equiv t^{n+1} - t^{n} \quad , \tag{3.9}$$

$$\Delta t^{n} \equiv \frac{1}{2}\left(\Delta t^{n+\frac{1}{2}} + \Delta t^{n-\frac{1}{2}}\right) \quad , \tag{3.10}$$

$$\Delta m_{k+\frac{1}{2}} \equiv m_{k+1} - m_{k} \quad , \tag{3.11}$$

$$\Delta m_{k} \equiv \frac{1}{2}\left(\Delta m_{k+\frac{1}{2}} + \Delta m_{k-\frac{1}{2}}\right) \quad , \tag{3.12}$$

then equations (3.2) to (3.8) may be differenced as

$$V^{n}_{k+\frac{1}{2}} = \frac{4\pi}{3}\,\frac{(r^{n}_{k+1})^{3} - (r^{n}_{k})^{3}}{\Delta m_{k+\frac{1}{2}}} \quad , \tag{3.13}$$

$$v^{n+\frac{1}{2}}_{k} = \frac{r^{n+1}_{k} - r^{n}_{k}}{\Delta t^{n+\frac{1}{2}}} \quad , \tag{3.14}$$

$$\frac{v^{n+\frac{1}{2}}_{k} - v^{n-\frac{1}{2}}_{k}}{\Delta t^{n}} = -4\pi (r^{n+\lambda}_{k})^{2}\,\frac{(P^{n+\lambda}_{k+\frac{1}{2}} - P^{n+\lambda}_{k-\frac{1}{2}})}{\Delta m_{k}} - \frac{G m_{k}}{(r^{n+\lambda}_{k})^{2}} \quad , \tag{3.15}$$

$$\frac{E^{n+1}_{k+\frac{1}{2}} - E^{n}_{k+\frac{1}{2}}}{\Delta t^{n+\frac{1}{2}}} + P^{n+\frac{1}{2}}_{k+\frac{1}{2}}\,\frac{V^{n+1}_{k+\frac{1}{2}} - V^{n}_{k+\frac{1}{2}}}{\Delta t^{n+\frac{1}{2}}} + \frac{L^{n+\frac{1}{2}}_{k+1} - L^{n+\frac{1}{2}}_{k}}{\Delta m_{k+\frac{1}{2}}} = \Sigma^{n+\frac{1}{2}}_{k+\frac{1}{2}} \quad , \tag{3.16}$$

$$L'^{n}_{k} = -\left[4\pi (r^{n}_{k})^{2}\right]^{2}\,\frac{ac}{3\kappa^{n}_{k}}\,\frac{(T^{n}_{k+\frac{1}{2}})^{4} - (T^{n}_{k-\frac{1}{2}})^{4}}{\Delta m_{k}} \quad , \tag{3.17}$$

$$x^{n}_{k} = \left|L'^{n}_{k}\right| \{2\pi (r^{n}_{k})^{2} ac (T^{n\,4}_{k-\frac{1}{2}} + T^{n\,4}_{k+\frac{1}{2}})\}^{-1} \quad , \tag{3.18}$$

$$L^{n}_{k} = L'^{n}_{k}\{1 + x^{n}_{k} + 3x^{n}_{k}\cdot\exp(-3x^{n}_{k}/2)\}^{-1} \quad . \tag{3.19}$$

Note that in equation (3.13) the exact expression for the specific volume is used since it is available.

Certain variables in the finite difference equations appear with half-integral subscripts or superscripts. This follows from the presence of derivatives in the hydrodynamical equations; derivatives are evaluated midway between two mesh points. There also occurs in equation (3.15) the superscript $(n+\lambda)$. This represents the point midway in time between $t^{n-\frac{1}{2}}$ and $t^{n+\frac{1}{2}}$, thus

$$t^{n+\lambda} = t^n + (\Delta t^{n+\frac{1}{2}} - \Delta t^{n-\frac{1}{2}})/4 \ . \qquad (3.20)$$

This differs from t^n itself only when the time step size changes from one iteration to the next. In practice the following approximations are used:

$$r_k^{n+\lambda} = r_k^n + v_k^{n-\frac{1}{2}}(\Delta t^{n+\frac{1}{2}} - \Delta t^{n-\frac{1}{2}})/4 \ , \qquad (3.21)$$

$$\dot{p}_{k+\frac{1}{2}}^{n-\frac{1}{2}} = \frac{p_{k+\frac{1}{2}}^n - p_{k+\frac{1}{2}}^{n-1}}{\Delta t^{n-\frac{1}{2}}} \ , \qquad (3.22)$$

$$p_{k+\frac{1}{2}}^{n+\lambda} = p_{k+\frac{1}{2}}^n + \dot{p}_{k+\frac{1}{2}}^{n-\frac{1}{2}} (\Delta t^{n+\frac{1}{2}} - \Delta t^{n-\frac{1}{2}})/4 \ . \qquad (3.23)$$

Equation (3.16) calls for the pressure and luminosity evaluated at time $(n+\frac{1}{2})$, whereas the other equations define them at time n. This is remedied by defining

$$P_{k+\frac{1}{2}}^{n+\frac{1}{2}} = \frac{1}{2}\left(P_{k+\frac{1}{2}}^{n+1} + P_{k+\frac{1}{2}}^{n}\right) \quad , \tag{3.24}$$

$$L_k^{n+\frac{1}{2}} = \theta L_k^{n+1} + (1-\theta) L_k^n \quad . \tag{3.25}$$

The parameter θ allows one to choose between forward differenced ($\theta = 0$), backward differenced ($\theta = 1$), or time centered ($\theta = 1/2$) equations. For a discussion on the merits of various choices of θ see Appendix A. The value $\theta = \frac{1}{2}$ was chosen in all the calculations.

Taking equations (3.13) and (3.16) together, each variable is defined at either integral or half-integral mesh points, but never at both. Therefore all half-integers can be rounded up to the next integer without causing confusion (i.e. the variable name itself suffices to distinguish between integral and half-integral subscripts). This allows the variables to be simply stored as arrays.

A few more ingredients are needed before the equations can be solved. These are: (i) an equation of state to determine the pressure and energy, (ii) the energy sources, represented by 'Σ', (iii) the opacity 'κ', (iv) the effect of shock waves, and (v) the boundary conditions. Points (i) through (iv) are discussed in subsequent sections of this chapter.

In a standard forty zone model the zones are numbered from 2 to 41 respectively. An artificial zone (#1) is created with the same pressure; temperature and density as zone 2, and with outer radius $r = 0$. This zone ensures that the gradients of P, T and ρ vanish at the origin. Another artificial zone (#42) is created on the outside with zero temperature and

pressure and serves to carry away the luminosity of the star. It remains to specify the initial condition i.e. the state of the star at $t = 0$. The various initial models are discussed in Chapter IV. The white dwarf core typically consists of forty zones, with a further twenty zones or so for the extended envelope. The initial models are in hydrostatic equilibrium prior to nuclear runaway.

The calculations are initiated by explicitly switching the desired number of zones into nuclear statistical equilibrium. Since the progress of the burning front is not calculated, the total amount of incinerated matter becomes a free parameter. Deflagration calculations (Nomoto, 1984; Jeffrey and Sutherland, 1985) show that typically 1 $M_\odot$ is incinerated; the remainder of the core being ejected in an unburned (or partially burned) state. The deflagration calculations themselves contain a free parameter and so do not give unambiguous results. Jeffrey and Sutherland (1985) show that the density and velocity profiles resulting from detailed deflagration calculations are fairly similar to those generated by instantaneous incineration.

The time step is initially set to one hundred microseconds and subsequently increases slowly, subject to the restriction that the radius, density and temperature of all zones must each change by less than one percent per time step. The time step is also limited by the Courant condition

$$\Delta t < 0.8\ \Delta R(PV)^{-\frac{1}{2}} \qquad (3.26)$$

where ΔR is the width of the zone in question. The Courant condition

requires that the time step size must be smaller than the sound crossing time for any given zone. The sound velocity is given by $v = (\gamma P V)^{\frac{1}{2}}$. The numerical factor of 0.8 includes a margin of safety. Another limit to the time step size is the diffusion time. This is the time necessary for photons to diffuse across a given zone, and is given by

$$t_d = \frac{\kappa\rho}{c} (\Delta R)^2 \qquad (3.27)$$

where κ is the opacity and c is the speed of light. Note that when the supernova is in a state of homologous expansion ΔR increases linearly with time. However, ρ decreases as the inverse third power of time so the diffusion time decreases with time. The diffusion time eventually becomes the limiting constraint on the time step, and it subsequently becomes necessary to relax the constraint somewhat to keep the computing costs within reason. Thus as a compromise the time step is only required to be less than some time-dependent multiple of the diffusion time. This multiple is initially set to unity and increases to roughly one thousand by the end of the run. In practice no numerical difficulties have resulted from permitting the time step to exceed the diffusion time in this manner.

The Equation of State

The equation of state expresses the pressure, the specific internal energy and the entropy of the system as functions of density, temperature and composition. The major constituents are the electrons, the photons (i.e. the radiation field), and the ions. The pressure is important dynamically only at early times, until the supernova reaches the stage of

homologous expansion. The specific energy (i.e. energy per unit mass) allows the energy in equations (3.5) and (3.16) to be expressed in terms of temperature; equation (3.16) is then solved iteratively to determine the new temperature. The entropy is not essential as it does not appear in the hydrodynamical equations, but it is nonetheless useful as a check when the system undergoes adiabatic expansion. Following the usual custom the entropy is expressed as a dimensionless entropy (S/k) per baryon.

The radiation field contributes a

pressure $$P_r = \frac{a}{3} T^4 \quad , \tag{3.28}$$

specific energy $$E_r = aT^4 V \quad , \tag{3.29}$$

and entropy $$\sigma_r = \frac{4aT^3 V}{3R} \quad . \tag{3.30}$$

(Here R is the universal gas constant). The radiation field is assumed isotropic for purposes of defining pressure, and the radiation temperature is always taken to be equal to the matter temperature. This assumption becomes dubious when the nebula becomes optically thin, around fifty days or so after ignition.

The ions are treated as a non-degenerate ideal gas with

pressure $$P_i = \frac{RT}{\mu_i V} \tag{3.31}$$

energy $$E_{oi} = \frac{3}{2} P_i V \tag{3.32}$$

and entropy $$\sigma_i = \mu_i^{-1}\{\ell n(VT^{3/2})-5.572\} + \sum_j \frac{x_j}{A_j}\ell n\left(\frac{A_j^{5/2}}{x_j}\right) . \qquad (3.33)$$

Here μ_i is the mean atomic mass of the ions (in atomic mass units):

$$\mu_i^{-1} = \sum_j \frac{x_j}{A_j} , \qquad (3.34)$$

and x_j is the fraction by mass of nuclear species j, and A_j is the corresponding atomic weight. The entropy equation (3.33) is a form of the Sackur-Tetrode equation (with V and T expressed in CGS units). These expressions for the ions are inappropriate prior to the explosion when the ions form a lattice, but this is inconsequential as the extremely degenerate electrons then dominate the equation of state.

The equation of state for the electrons is relatively complicated: The number density of electrons is known from the matter density, apart from any electrons formed by electron-positron pair production. Expressions appropriate for a non-interacting Fermi gas have been developed. Corrections due to interactions are then added, as summarized by Salpeter (1961). These results are presented in Appendix B. These formulae are applied to the known electron density. The number of electron-positron pairs (if any) in existence is then calculated (see Appendix C), providing knowledge of the true electron and positron number densities. If necessary, the pressure and energy are re-evaluated using these corrected densities.

The total pressure and energy are then

$$P = P_r + P_i + P_e \qquad (3.35)$$

$$E = E_r + E_i + E_e \qquad (3.36)$$

Derivatives such as $\frac{\partial P}{\partial V}$ and $\frac{\partial P}{\partial T}$ are evaluated numerically. These equations are summarized in SUBROUTINE PRES which evaluates the pressure and energy to an accuracy of about one part in ten thousand.

Nuclear Statistical Equilibrium

As mentioned in Chapter II, carbon ignition in a critical core can lead to thermonuclear runaway due to the electron degeneracy. The ensuing reactions form an extensive burning network which includes dozens of nuclear species. For a discussion of such detailed burning networks see Clayton (1968).

The detailed calculations show that most of the reactions are near equilibrium so that the composition changes relatively slowly with time. In nuclear statistical equilibrium (NSE) all the permitted reactions are assumed to be at equilibrium and hence the distribution of nuclear species is determined by statistics alone (the Saha equation) rather than by reaction rates. The composition is then a function only of the density and the temperature and not on the history of the matter.

The NSE network has been restricted to the 'alpha-particle nuclei', i.e. to those nuclei with an equal even number of both protons and neutrons. The reasons for this are as follows: first, the fuel nuclei are carbon, oxygen, and possibly helium, all of which are alpha-particle nuclei, and so will be their fusion products; second, the primary mode of decay of the heavier nuclei is photodisintegration which usually knocks an alpha particle out of the nucleus. If these processes operated alone then the

restriction to alpha-particle nuclei would be strictly valid. However, Clayton (1968) has shown that under certain conditions the principal mode of photodisintegration of ^{56}Ni is $(\gamma,p),(\gamma,p)$ leading to ^{54}Fe. There are some similar reactions which produce other nonradioactive elements such as ^{58}Ni, ^{55}Co, ^{57}Ni, and ^{52}Fe (see Nomoto, 1984). Nevertheless, the NSE network has been restricted to alpha-particle nuclei for simplicity.

The details of the NSE equations are in Appendix D. The heaviest nucleus included is ^{72}Kr. Under all conditions investigated the most abundant nucleus is either ^{4}He or ^{56}Ni. As the temperature drops the fraction of ^{56}Ni increases as it is the most tightly bound nucleus in the network. Eventually all the matter in NSE becomes ^{56}Ni unless it is assumed that the material 'freezes out' before this happens, i.e. the reaction rates become longer than the dynamical timescale. A fairly large amount of ^{56}Ni is desirable both for powering the supernova light curve and for explaining the large cosmic ^{56}Fe abundance.

Recent calculations by Nomoto (1984) show that in carbon deflagration supernovae the nuclear burning proceeds to NSE only in the inner 50% or so of the critical core. Outside this region partial burning occurs, producing a wide range of intermediate mass elements. This partial burning releases most of the available nuclear binding energy but produces relatively little ^{56}Ni and hence little late-time luminosity. In Nomoto's calculations typically 60% to 70% of the incinerated matter becomes ^{56}Ni. This has the effect of reducing the maximum luminosity of the light curve somewhat. For comparison both this possibility and the complete incineration to ^{56}Ni are considered in certain models. The recent identification of intermediate mass elements in the SN I spectrum

indicates that Nomoto's partial burning results are at least qualitatively correct.

Radioactive Decay and Gamma-Ray Deposition

The nucleus ^{56}Ni is radioactive with a half-life of 6.1 days and decays by electron capture to ^{56}Co, emitting a neutrino and gamma-rays. The loss of the electron will slightly raise μ_e (i.e. lower the electron pressure) but this is not dynamically significant. The neutrino on average carries off 0.4144 Mev per decay which is lost to the star. The gamma-rays carry 1.7202 Mev per decay on average, some of which gets deposited elsewhere in the star, where it appears in the energy source term 'Σ'. The numerical data here (and for the following paragraph) are from the Table of Isotopes (Lederer and Shirley, 1978).

The resultant ^{56}Co nucleus is also radioactive with a half-life of 78.8 days. There are two modes of decay, the branching ratio is 80.8% electron capture and 19.2% positron emission. Axelrod (1980) has calculated the average kinetic energy per positron as 660 kev. Thus the decay energy is divided as follows: gamma-rays 3.306 Mev, neutrinos 1.1415 Mev, and positrons 0.120 Mev. The positron energy represents kinetic energy only (which is assumed to be deposited locally). Twice the positron rest mass energy has been added to the gamma-ray energy to account for positron annihilation.

The rate of gamma-ray deposition has been calculated following the method of Sutherland and Wheeler (1984), using an effective gamma-ray opacity of 0.03 cm^2-g^{-1}. The deposition function is the ratio between the

rate of local energy deposition and the rate of energy production via radioactive decay of initially pure ^{56}Ni. It is found numerically that up to $\sim 5\times10^5$ seconds after the explosion the deposition is close to unity in the radioactive region and near zero elsewhere. This is due to the short mean free path of the gamma-rays at early times. At later times deposition occurs fairly uniformly throughout the star and a significant fraction of the gamma-rays leak out of the system and hence never deposit their energy.

Opacity

The opacity constitutes a major source of error in determining theoretical supernova light curves. The difficulties in its calculation are outlined below. In this work the opacity is treated as a free parameter with a value of the order of 0.1 cm^2-g^{-1}. Qualitatively, a reduction in the opacity reduces the rise time to maximum light and gives the light curve a sharper peak.

The opacity determines the rate of radiative diffusion. This process is important from roughly one to fifty days after supernova ignition, affecting both the location of the photosphere and the energy flux through it. After this time the ejecta becomes optically thin and the radiative diffusion approximation breaks down.

The diffusion phase is characterized by densities from 10^{-10} to 10^{-15} g-cm^{-3} and temperatures from 3000 K to 50000 K. At the upper end of this temperature range the dominant source of opacity is electron scattering (see for example Clayton, 1968; and Huebner et al, 1977). The opacity then has a particularly simple form

$$\kappa = 0.40\ \mu_e^{-1}\ f\ cm^2\text{-}g^{-1} \qquad (3.37)$$

where f is the fractional ionization.

The situation is more complicated at lower temperatures, with bound-bound and bound-free transitions becoming important. These latter sources of opacity are strongly dependent on temperature, density and composition, which renders their calculation very difficult. Furthermore, the bound-bound opacity is subject to an effect called 'Doppler enhancement'. This effect occurs in the presence of a velocity gradient and is due to the Doppler shifting of the bound-bound absorption peaks relative to the photons. The calculations of Karp et al (1977) show that this effect typically increases the opacity by as much as a factor of two or so, but under certain conditions by as much as a factor of ten.

Opacity curves for certain elements (without Doppler enhancement) are presented in Colgate and McKee (1969). Iron has an opacity of 0.03 $cm^2\text{-}g^{-1}$ or larger under the conditions of interest; this is a plausible lower bound for the opacity. Several factors other than Doppler enhancement cause uncertainty in the opacity: one is the composition and another is the ambient photon distribution (if not blackbody). The former is a problem because the abundances of intermediate mass elements are quite uncertain, but their effect on the opacity may be pronounced (as for instance in the solar spectrum). The latter effect matters if the opacity is non-grey (frequency dependent), as in the case for bound-bound and bound-free opacity (but not for the electron scattering opacity). Below about 5000 K the opacity of certain elements is expected to drop sharply due to recombination, but it is not clear if this actually takes place. The observed colour temperature of SN I (as measured by the colour index) drops to 4500 K at the hump-tail transition and then rises again. However, it

is not clear how closely the ionization temperature agrees with the colour temperature, as the matter and the radiation may decouple to some extent. In fact, the results (see Chapter V) do not suggest a significant drop in the opacity near 5000 K.

In consideration of the above uncertainties, a benchmark value of 0.1 cm^2-g^{-1} is used for the opacity in most of the present calculations. This value is probably accurate to within a factor of two or three. As will be seen in Chapter V, this value is tenable only for the bare white dwarf models; more massive stars (those with envelopes) require concominant reduction in the opacity to keep their light curves in agreement with observations. In certain models a crude temperature dependence has been built into the opacity to show its qualitative effect. The specific prescriptions used in this regard are detailed in Chapter IV.

Shock Waves

A shock front is a surface of sharp, discontinuous change in pressure, temperature, density, entropy, and velocity. In reality the variables are not truly discontinuous; they change smoothly over a region of characteristic width δ which depends on the viscosity of the medium. In the problem at hand δ is much smaller than the width of a zone, hence the shock is effectively discontinuous. Such a shock front is incompatible with finite difference calculations which presuppose that the system changes smoothly from one mesh point to the next. Over the years many schemes have been developed to handle shocks (several methods are discussed in Richtmeyer and Morton 1967; hereafter RM) , but the most common is to introduce a 'pseudoviscous' pressure, represented by the symbol Q. Following Falk and Arnett (1977) the choice adopted for this term is

$$Q^{n-\frac{1}{2}}_{k+\frac{1}{2}} = \frac{4(v^{n-\frac{1}{2}}_{k+1} - v^{n-\frac{1}{2}}_{k})^2}{V^{n}_{k+\frac{1}{2}} - V^{n-1}_{k+\frac{1}{2}}} \quad , \quad \text{if} \begin{cases} V^{n}_{k+\frac{1}{2}} < V^{n-1}_{k+\frac{1}{2}} \\ v^{n-\frac{1}{2}}_{k+1} < v^{n-\frac{1}{2}}_{k} \end{cases} \tag{3.38}$$

$$= 0 \quad , \quad \text{otherwise.}$$

This term is directly added to the pressure in equations (3.15) and (3.16):

$$\frac{v^{n+\frac{1}{2}}_{k} - v^{n-\frac{1}{2}}_{k}}{\Delta t^{n}} = 4\pi (r^{n+\lambda}_{k})^2 \frac{P^{n+\lambda}_{k+\frac{1}{2}} + Q^{n-\frac{1}{2}}_{k+\frac{1}{2}} - P^{n+\lambda}_{k-\frac{1}{2}} - Q^{n-\frac{1}{2}}_{k-\frac{1}{2}}}{\Delta m_k} - \frac{GM_k}{(r^{n+\lambda}_{k})^2} \quad , \tag{3.39}$$

$$\frac{E^{n+1}_{k+\frac{1}{2}} - E^{n}_{k+\frac{1}{2}}}{\Delta t^{n+\frac{1}{2}}} + (P^{n+\frac{1}{2}}_{k+\frac{1}{2}} + Q^{n-\frac{1}{2}}_{k+\frac{1}{2}}) \frac{(V^{n+1}_{k+\frac{1}{2}} - V^{n}_{k+\frac{1}{2}})}{\Delta t^{n+\frac{1}{2}}} + \frac{L^{n+\frac{1}{2}}_{k+1} - L^{n+\frac{1}{2}}_{k}}{\Delta m_{k+\frac{1}{2}}} = \Sigma^{n+\frac{1}{2}}_{k+\frac{1}{2}} \tag{3.40}$$

Note that the Q terms are not time-centered. This allows equations (3.39) and (3.40) to be evaluated explicitly.

The pseudoviscosity stiffens the equation of state when sudden compression (i.e. a shock) occurs, which has the effect of spreading the shock out spacially. The pseudoviscosity contains an arbitrary numerical coefficient which determines the extent of the spreading: the coefficient chosen in equation (3.38) spreads the shock over three or four zones. The overall shock strength is not affected by the introduction of pseudoviscosity. This is demonstrated in various tests of the pseudoviscosity method, discussed in RM.

Despite its success and extensive use in astrophysics, the pseudoviscosity method has a drawback. The shock waves in the problem at hand are exceedingly strong, with the temperature jumping by several orders of magnitude at the shock front. As discussed earlier, for numerical accuracy

only a one percent fractional change in temperature is permitted at each iteration. Clearly then a large number of iterations are needed to raise the temperature of the zone being shocked by the required amount. This difficulty may be mitigated by relaxing the one percent criterion to, say, a four or five percent change per iteration, but this significantly increases the error inherent in the finite difference equations.

For such a strong shock a method which explicitly recognizes the discontinuous nature of a shock would be more efficient. Given the conditions in the unshocked material and the shock strength (as represented by the velocity discontinuity 'Δ'), then from the Hugoniot relations all the post-shock conditions can be found. The relevant equations are derived and discussed in Appendix E. Such a method of shock fitting actually predates the pseudoviscosity method and is briefly described in Sections 12.8 and 12.9 of RM.

This analytical method of shock treatment has the two salient advantages of speed and correct shock profile over the pseudoviscosity method, but of course there are drawbacks. With the analytical method it is useful to distinguish pre-shock and post-shock material by placing a zone boundary (or two) at the shock front. In practice the shock front is represented by a zone of negligible mass whose boundaries reflect the pre-shock and post-shock conditions. These two zone boundaries shift position at each time step thus negating (locally) the advantage of having fixed (in Lagrangian terms) mesh points.

Prior to being shocked the envelope is in hydrostatic equilibrium and is neither zoned nor evolved hydrodynamically. The shock from the exploding star moves out through the envelope, sweeping up (per iteration) an amount of matter determined by the shock velocity and the size of the

time step. This newly swept-up matter is formed into a new mini-zone (which is far smaller than the other established zones). On the subsequent time step this mini-zone is merged with the zone interior to it and a new mini-zone is created by the shock. The accreting zone eventually becomes significantly larger than the rest, whereupon it is split into two smaller zones. When the shock has passed through the entire envelope typically about twenty new zones will have been created in this way.

As mentioned above the Hugoniot equations do not completely specify the post-shock conditions. To them must be added one more condition which determines how the shock strength varies with time. Various prescriptions for this condition were tried out in test calculations, with the following proving sufficient:

$$\frac{dv_{shock}}{dt} = \frac{\partial v}{\partial t} = -4\pi r^2 \frac{\partial P}{\partial m} \qquad (3.41)$$

where $\frac{\partial P}{\partial m}$ is the pressure gradient evaluated immediately behind the shock. This expression is further refined by making perturbational corrections to the zone velocities after each iteration which ensure that $\frac{\partial v}{\partial m}$ is constant over the outer two zones. This is done to ensure energy conservation when the two outer zones are merged into a single one.

To test this system of handling shock waves some trials were run to simulate a point explosion in a uniform density cold gas, a problem for which the analytic solution is known (commonly called the Sedov solution). The analytic solutions are given in Landau and Lifshitz (1959) (but note their equation (99.10) should read $\nu_5 = \frac{2}{\gamma-2}$). Two models were run, both starting with just two zones. As the same program was used for these models

as for the supernova calculations themselves, the pressure was supplied by both photon and particle gases. In order to compare the results to Sedov theory the adiabatic index must remain constant throughout the calculations, hence the initial conditions were chosen so that the first model was radiation dominated ($\gamma = 4/3$), while the second model was matter dominated ($\gamma = 5/3$). Both models were evolved until the radius had increased by a factor of several hundred.

For both models the velocity, pressure and density behind the shock front are shown as functions of the Eulerian and Lagrangian coordinates, all values being normalized to the values at the shock front. As the theoretical solutions are self-similar, the curves presented in this manner are independent of time. The results are shown in Figures 3-1 through 3-4. Both models show excellent agreement with the theory; the only noticeable deviations being in the velocity of the inner few zones, which oscillate about their mean theoretical values. These oscillations result from small disturbances being magnified as they propagate inward down the density gradient.

The shock algorithm was also tested on sample supernovae models, whereupon another point came to light. When the exploded critical core rams the envelope a second shock (called the reverse shock) forms which propagates inwards in Lagrangian coordinates (although outwards in Eulerian coordinates). This reverse shock reheats the adiabatically cooled core. In certain models this reverse shock is relatively weak and hence can be handled by the pseudoviscosity method reasonably efficiently. However, in other models the reverse shock is quite strong in which case it is necessary to use the above shock fitting procedure on both shocks to gain

efficiency. The reverse shock is handled analogously to the outward shock although separate subroutines are used to account for the different boundary conditions. In all models the reverse shock slowly weakens and in some cases disappears entirely a few days after supernova ignition.

It should be noted that in general pseudoviscosity is used concurrently with the above analytic treatment to handle the various other minor shock-like disturbances which may arise during the calculations.

For the bare white dwarf models for SN I the analytic treatment of shocks is superfluous. Conversely, in extended progenitor models the passage of the shock through the envelope takes perhaps five times as many iterations with the pseudoviscosity method as compared to the analytic method. This ratio may be reduced by relaxing the time step criterion to (say) a three or four percent change in each variable per iteration, which speeds up the pseudoviscosity calculation, but this compromise sacrifices accuracy and is still slower than the analytic method.

Figure 3-1

Results for a point explosion in a uniform density, zero temperature atmosphere (Sedov solution). The explosion is radiation dominated and hence has adiabatic index $\gamma = 4/3$. The numerical results are calculated using the program BOMB. Plotted are velocity (+++), pressure (◇◇◇), and density (***) versus radius, all normalized to the values at the shock front. The absolute errors in the normalization factors are about 0.1%. The solid curves represent the corresponding analytical solutions.

FIGURE 3-1

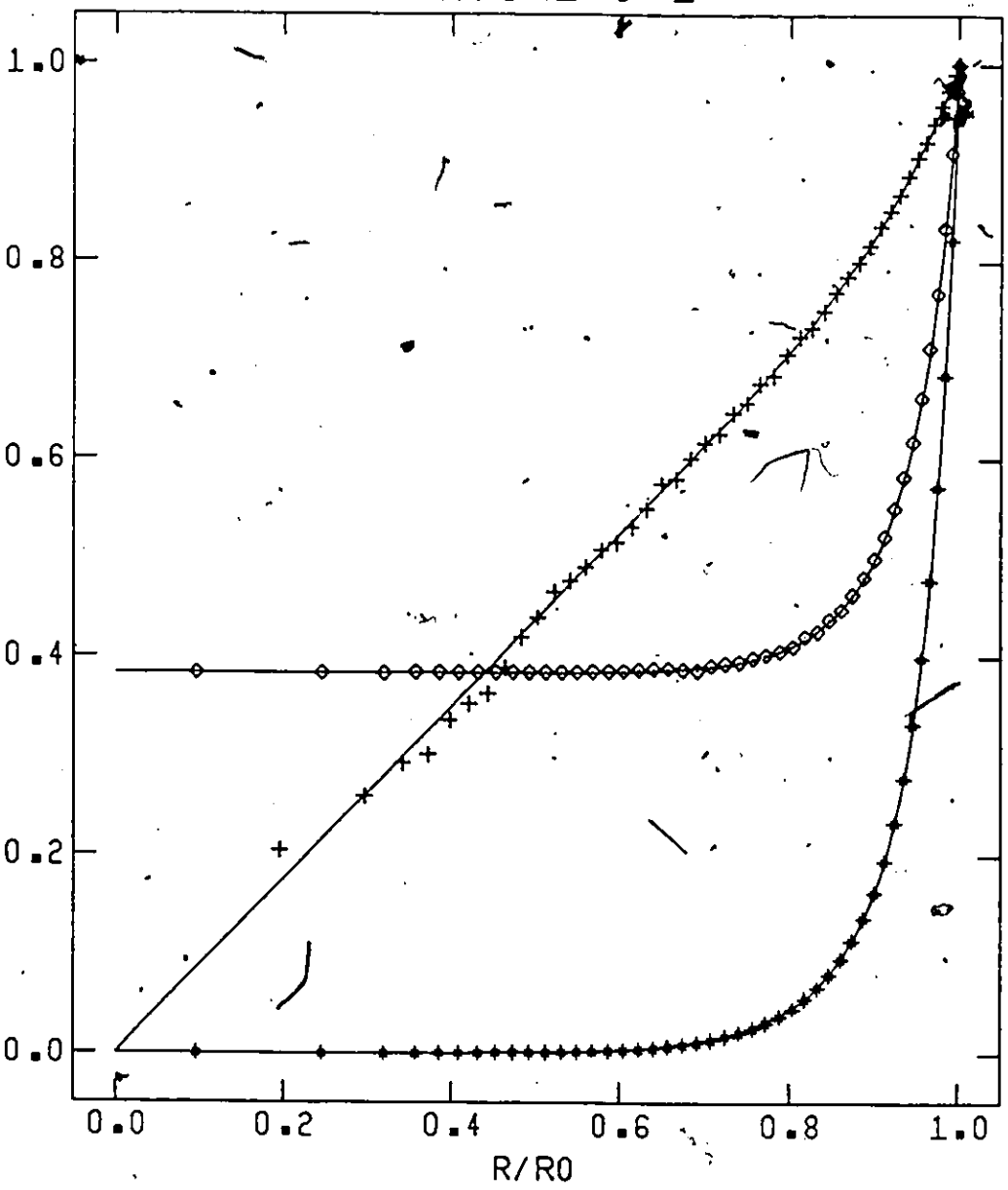

Figure 3-2

Numerical Sedov solution with $\gamma = 4/3$ plotted against mass function. Plotted are velocity (***), pressure (◇◇◇), and density (+++) normalized to the shock front. The solid curves are the corresponding analytical solutions.

FIGURE 3-2

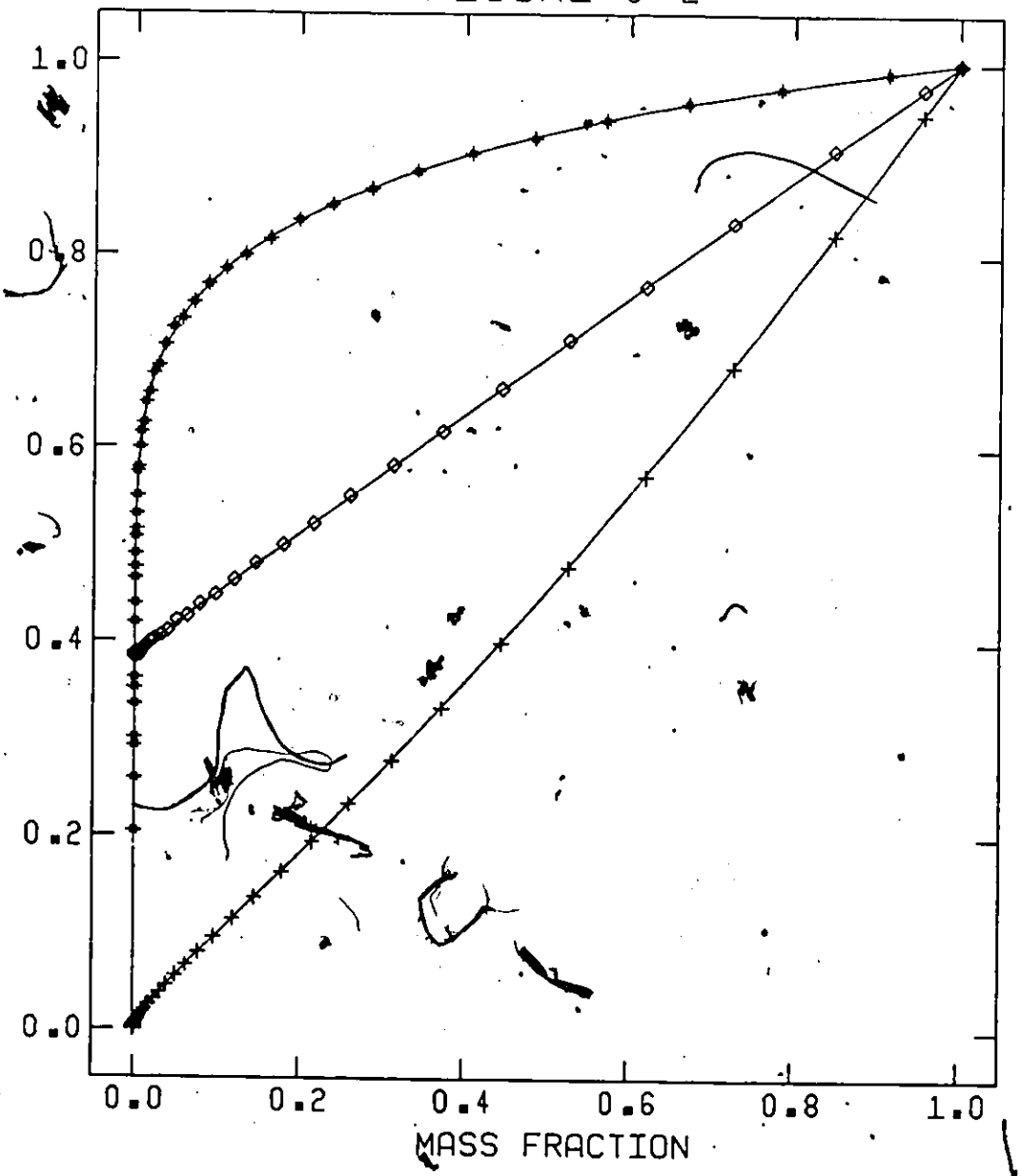

Figure 3-3

Numerical Sedov solution for a monatomic particle gas ($\gamma = 5/3$) plotted against radius. Plotted are velocity (***), pressure (◇◇◇), and density (+++), normalized to their values at the shock front. The solid curves are the corresponding analytical solutions.

FIGURE 3-3

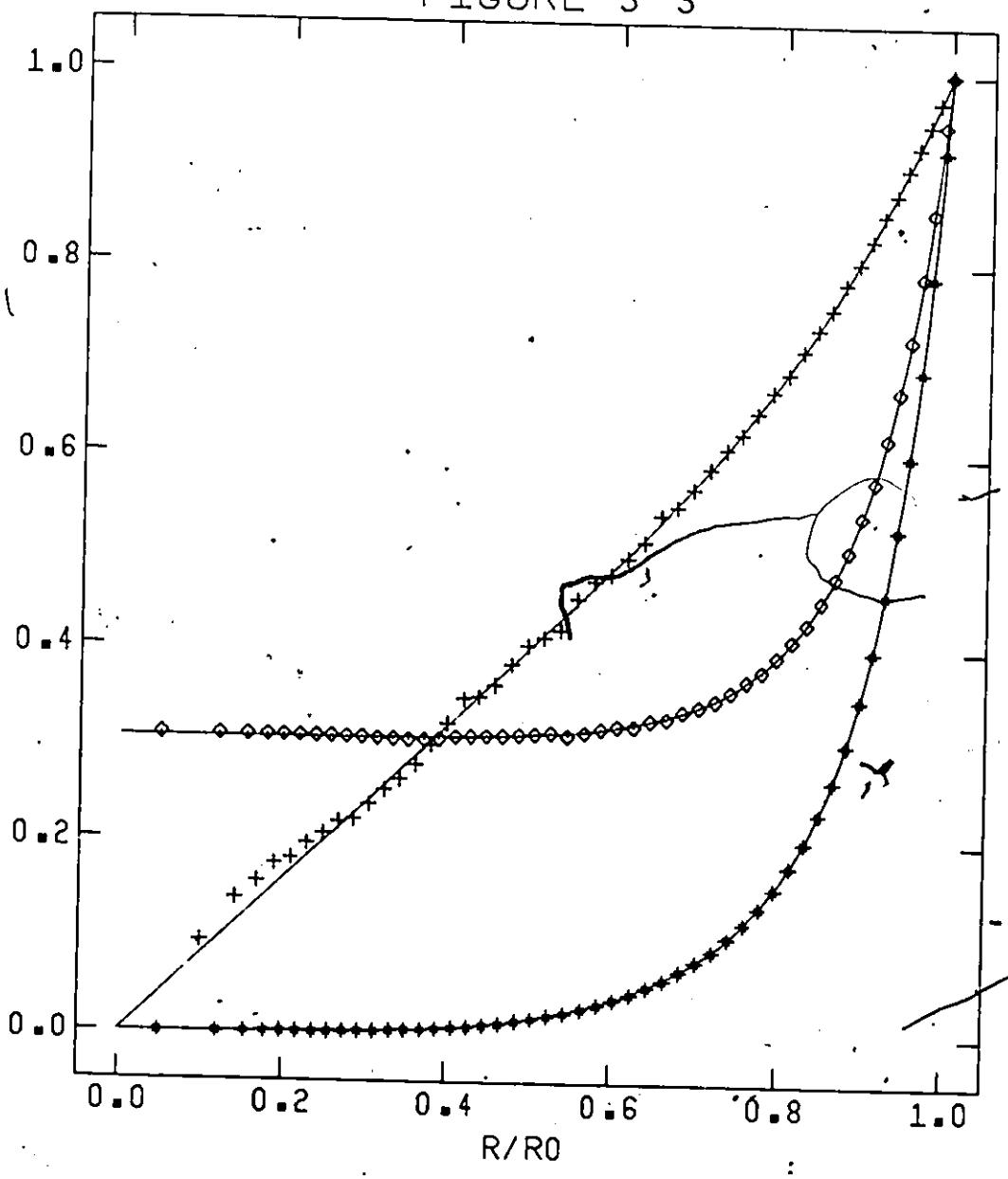

Figure 3-4

Numerical Sedov solution with $\gamma = 5/3$ plotted against mass fraction. Plotted are velocity (****), pressure (◇◇◇) and density (+++), normalized to the shock front. The solid curves are the corresponding analytical solutions.

FIGURE 3-4

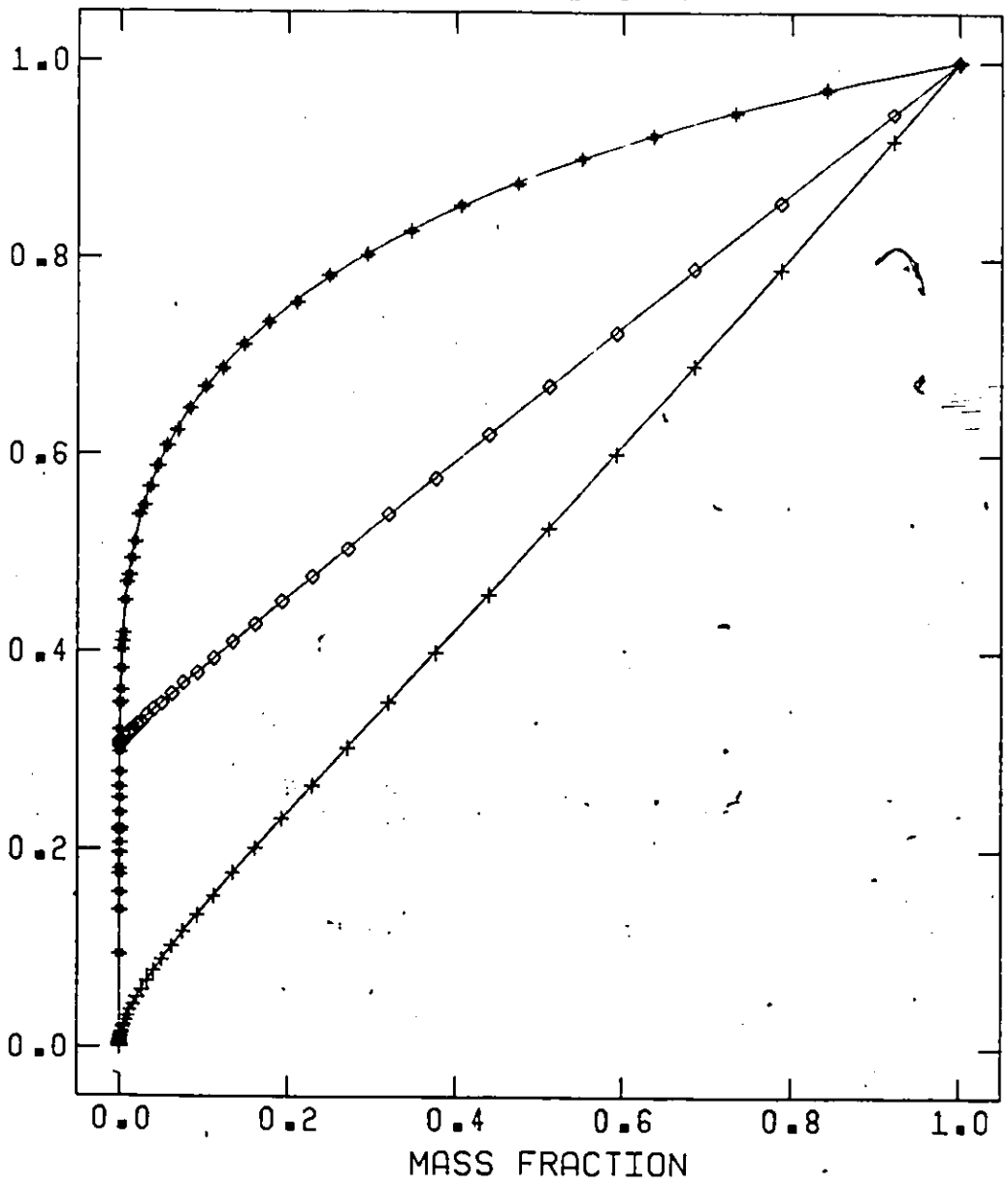

CHAPTER IV

INITIAL CONDITIONS

A total of seventeen models were hydrodynamically evolved using the methods described in the previous chapter. For each model the central density, the initial temperature (assumed isothermal) and the composition were specified, which, assuming hydrostatic equilibrium, uniquely determine the structure of the core. The cores were generated and zoned by the program WHITE. Envelopes were then added as detailed in the next section. To the progenitors so generated three more parameters must be added: the amount of mass to incinerate, the amount of ^{56}Ni produced, and the opacity function. Mathematically, these parameters and the progenitors themselves serve as initial conditions for the differential equations of the previous chapter. The hydrodynamic calculations were carried out by the program BOMB. The results of these calculations are presented in Chapter V.

Envelope Parametrization

The 'envelope' refers to the extended, low density, non-degenerate matter surrounding the degenerate core. The star may be conceptually divided into core and envelope without difficulty as there is a nearly discontinuous drop in density at the core-envelope interface. The envelopes constructed for the models in this work are uniquely determined by a set of five parameters. One of these parameters is the total envelope mass M_{env}. The other four are radii, labelled r_1 through r_4. The envelope

extends from r_1 to r_4 and has the following density profile:

$$\rho(r) = c_1 \quad , \quad r_1 < r < r_2$$
$$\rho(r) = c_1 r_2^2 r^{-2} \quad , \quad r_2 < r < r_3$$
$$\rho(r) = c_1 r_2^2 r_3^2 r^{-4} \quad , \quad r_3 < r < r_4 \; . \qquad (4.1)$$

The density is continuous throughout the envelope. The constant c_1 follows from the envelope mass. The composition of the envelope is always taken to be 90% helium and 10% carbon. The temperature profile of the envelope is determined by the condition of hydrostatic equilibrium.

The three density gradients were chosen for straightforward reasons. Constant density profiles have often been used in the past (e.g. Lasher 1975). The inverse square profile has the desirable property that $\frac{\partial m}{\partial r}$ is constant. The inverse fourth power profile was chosen as it is a good fit to the outer structure of R Cor Bor stars (Saio 1983).

Tables of Initial Conditions

Tables 4.1 through 4.3 list the progenitor characteristics for each of the seventeen models examined, which are divided into four groups labelled A through D. The models within each group have similar core characteristics. An explanation of the parameters listed in the tables follows.

M_{tot} is the total mass of the progenitor (core plus envelope) in units of the solar masses (i.e. 1.99×10^{33} grams).

M_{core} is the mass of the critical core in solar masses. All seventeen models have M_{core} close to the Chandrasekhar mass.

M_{env} is the mass (in solar masses) of the envelope.

Table 4.1

PARAMETERS FOR GROUP A AND B MODELS

	A1	A2	B1	B2	B3	B4
M_{tot}	1.387	1.387	1.806	1.806	1.806	1.806
M_{core}	1.387	1.387	1.406	1.406	1.406	1.406
M_{env}	-	-	0.400	0.400	0.400	0.400
M_{co}	0.983	0.983	1.264	1.264	1.264	1.264
M_{incin}	0.983	0.983	1.098	1.098	1.098	1.098
M_{rad}	0.983	0.584	1.098	1.098	1.098	1.098
ρ_c	3.0×10^9	3.0×10^9	1.07×10^{10}	1.07×10^{10}	1.07×10^{10}	1.07×10^{10}
T_o	5.7×10^7	5.0×10^7	1.58×10^7	1.58×10^7	1.58×10^7	1.58×10^7
R_{core}	1.61×10^8	1.61×10^8	1.11×10^8	1.11×10^8	1.11×10^8	1.11×10^8
κ	0.10	0.10	0.10	0.10	var.	var.
r_1	-	-	1.0×10^{10}	1.0×10^{11}	1.0×10^{11}	1.0×10^{11}
r_2	-	-	1.3×10^{11}	1.3×10^{12}	1.3×10^{12}	1.3×10^{12}
r_3	-	-	1.3×10^{11}	1.3×10^{12}	1.3×10^{12}	1.3×10^{12}
r_4	-	-	8.33×10^{12}	8.33×10^{13}	8.33×10^{13}	8.33×10^{13}
$\rho(r_1)$	-	-	2.18×10^{-2}	2.18×10^{-5}	2.18×10^{-5}	2.18×10^{-5}
$\rho(r_4)$	-	-	1.30×10^{-9}	1.3×10^{-12}	1.3×10^{-12}	1.3×10^{-12}
$\langle r_{env} \rangle$	-	-	4.35×10^{11}	4.35×10^{12}	4.35×10^{12}	4.35×10^{12}
N_{tot}	40	40	60	60	60	60
E_{net}	1.24×10^{51}	1.15×10^{51}	1.39×10^{51}	1.39×10^{51}	1.39×10^{51}	1.39×10^{51}
$\bar{v}$	9.48×10^8	9.13×10^8	8.79×10^8	8.79×10^8	8.79×10^8	8.79×10^8

Table 4.2

PARAMETERS FOR GROUP C MODELS

	C1	C2	C3	C4	C5	C6
M_{tot}	2.000	2.000	2.000	2.000	2.000	2.000
M_{core}	1.385	1.385	1.385	1.385	1.385	1.385
M_{env}	0.615	0.615	0.615	0.616	0.616	0.615
M_{co}	1.385	1.385	1.385	1.385	1.385	1.385
M_{incin}	1.196	1.196	1.196	1.196	1.196	1.196
M_{rad}	1.196	1.196	1.196	1.196	0.703	0.0
ρ_c	3.0×10^{9}	3.0×10^{9}	3.0×10^{9}	3.0×10^{9}	3.0×10^{9}	3.0×10^{9}
T_o	1.0×10^{8}	1.0×10^{8}	1.0×10^{8}	1.0×10^{8}	1.0×10^{8}	1.0×10^{8}
R_{core}	1.6×10^{8}	1.6×10^{8}	1.6×10^{8}	1.6×10^{8}	1.6×10^{8}	1.6×10^{8}
κ	0.10	0.10	0.10	0.10	0.10	0.10
r_1	1.0×10^{11}	1.0×10^{11}	5.0×10^{10}	8.45×10^{9}	8.45×10^{9}	5.0×10^{10}
r_2	5.0×10^{13}	1.0×10^{11}	5.0×10^{11}	8.45×10^{10}	8.45×10^{10}	5.0×10^{13}
r_3	5.0×10^{13}	5.0×10^{13}	5.0×10^{12}	8.45×10^{11}	8.45×10^{11}	5.0×10^{13}
r_4	5.0×10^{13}	5.0×10^{13}	5.0×10^{13}	8.45×10^{12}	8.45×10^{12}	5.0×10^{13}
$\rho(r_1)$	2.34×10^{-9}	1.95×10^{-4}	4.26×10^{-5}	8.83×10^{-3}	8.83×10^{-3}	2.34×10^{-9}
$\rho(r_4)$	2.34×10^{-9}	7.8×10^{-10}	4.3×10^{-11}	8.83×10^{-9}	8.83×10^{-9}	2.34×10^{-9}
$\langle r_{env} \rangle$	3.75×10^{13}	2.50×10^{13}	7.65×10^{12}	1.29×10^{12}	1.29×10^{12}	3.75×10^{13}
N_{tot}	71	71	71	71	71	71
E_{net}	1.62×10^{51}	1.62×10^{51}	1.62×10^{51}	1.62×10^{51}	1.51×10^{51}	1.35×10^{51}
$\bar{v}$	9.02×10^{8}	9.02×10^{8}	9.02×10^{8}	9.02×10^{8}	8.71×10^{8}	8.23×10^{8}

Table 4.3

PARAMETERS FOR GROUP D MODELS

	D1	D2	D3	D4	D5
M_{tot}	1.692	1.692	1.692	1.692	1.692
M_{core}	1.385	1.385	1.385	1.385	1.385
M_{env}	0.308	0.308	0.308	0.308	0.308
M_{co}	1.385	1.385	1.385	1.385	1.385
M_{incin}	1.103	1.103	1.103	1.103	1.103
M_{rad}	1.103	0.625	0.625	1.103	0.625
ρ_c	3.0×10^{9}	3.0×10^{9}	3.0×10^{9}	3.0×10^{9}	3.0×10^{9}
T_o	1.0×10^{8}	1.0×10^{8}	1.0×10^{8}	1.0×10^{8}	1.0×10^{8}
R_{core}	1.6×10^{8}	1.6×10^{8}	1.6×10^{8}	1.6×10^{8}	1.6×10^{8}
κ	0.10	0.10	var.	0.10	0.10
r_1	5.0×10^{10}	5.0×10^{10}	5.0×10^{10}	8.45×10^{9}	8.45×10^{9}
r_2	5.0×10^{11}	5.0×10^{11}	5.0×10^{11}	8.45×10^{10}	8.45×10^{10}
r_3	5.0×10^{12}	5.0×10^{12}	5.0×10^{12}	8.45×10^{11}	8.45×10^{11}
r_4	5.0×10^{13}	5.0×10^{13}	5.0×10^{13}	8.45×10^{12}	8.45×10^{12}
$\rho(r_1)$	2.13×10^{-5}	2.13×10^{-5}	2.13×10^{-5}	4.42×10^{-3}	4.42×10^{-3}
$\rho(r_4)$	2.13×10^{-11}	2.13×10^{-11}	2.13×10^{-11}	4.42×10^{-9}	4.42×10^{-9}
$\langle r_{env} \rangle$	7.65×10^{12}	7.65×10^{12}	7.65×10^{12}	1.29×10^{12}	1.29×10^{12}
N_{tot}	55	55	55	55	55
E_{net}	1.45×10^{51}	1.34×10^{51}	1.34×10^{51}	1.45×10^{51}	1.34×10^{51}
$\bar{v}$	9.28×10^{8}	8.92×10^{8}	8.92×10^{8}	9.28×10^{8}	8.92×10^{8}

M_{co} is the mass (in solar masses) of that part of the core composed of 50% carbon and 50% oxygen by mass, a mixture designated hereafter by the label C/O. If M_{co} is less than M_{core}, then the remainder of the core is composed of helium. The core helium layer is always external to the C/O layer.

M_{incin} is the mass (in solar masses) incinerated by the supernova. In these models this is always the innermost part of the star (no off-centre ignition models are considered). M_{incin} determines how much nuclear binding energy is released in the explosion and hence the kinetic energy of the ejecta.

M_{rad} is the mass (in solar masses) of radioactive ^{56}Ni formed in the supernova. Usually this is assumed equal to M_{incin}. In accordance with the assertion of Nomoto (1984), in some models M_{rad} is set to $\sim$ 60% of M_{incin}, with the remaining incinerated matter forming non-radioactive products. For calculating the binding energy released in the explosion it is assumed that these non-radioactive nuclei have on average the same binding energy per nucleon as ^{56}Ni. When M_{rad} is not equal to M_{incin}, then it is the innermost material which is radioactive.

ρ_c is the central density of the progenitor in units of $g\text{-}cm^{-3}$. For these models this density is in the range $(3\text{-}11)\times10^9$ $g\text{-}cm^{-3}$ which is appropriate for pycnonuclear carbon burning.

T_o is the initial temperature of the core in degrees Kelvin. The cores are assumed to be initially isothermal for simplicity.

R_{core} is the radius of the core in centimetres.

κ is the opacity of the ejecta to (thermal) photons in units of $cm^2\text{-}g^{-1}$. This is distinct from the gamma-ray opacity which is set to $0.03\ cm^2\text{-}g^{-1}$ in all models. In most models κ is set to $0.10\ cm^2\text{-}g^{-1}$ in lieu of better knowledge of the true opacity function. In three models special temperature-dependent opacity functions are used, primarily to judge their qualitative effect. These functions are described in detail in a following section.

r_1 is the inner radius of the envelope. Ideally this should coincide with the surface of the core but in practice this is not necessary, as r_1 is small enough so that the region inside would contain a negligible fraction of the envelope. Choosing $r_1 >> R_{core}$ allows the exploded core to settle into homologous expansion prior to encountering the envelope.

Between r_1 and r_2 the envelope density profile is constant (prior to being shocked, of course). The density profile is continuous at r_2 but the slope changes (to $\rho \propto r^{-2}$). At r_3 the slope changes again (to $\rho \propto r^{-4}$), and continues out to r_4, the surface of the star. All radii (r_1 through r_4) are measured in centimetres.

$\rho(r_1)$ is the density at the inner boundary of the envelope (in $g\text{-}cm^{-3}$). It may be calculated from the five basic envelope parameters as follows

$$\rho(r_1) = \frac{M_{env}}{4\pi} \{2r_2^2 r_3 - \frac{1}{3}(r_1^3 + 2r_2^3 + 3r_2^2 r_3^2 r_4^{-1})\}^{-1} \quad . \qquad (4.2)$$

$\rho(r_4)$ is the density at the outer boundary of the envelope in $g\text{-}cm^{-3}$). It is given by

$$\rho(r_4) = \rho(r_1) r_2^2 r_3^2 r_4^{-4} \quad . \qquad (4.3)$$

$\langle r_{env} \rangle$ is the mass-weighted mean envelope radius (in centimetres). This quantity indicates where the bulk of the envelope mass is located. An envelope with a large $\langle r_{env} \rangle$ has more effect on the light curve than one with a small $\langle r_{env} \rangle$. The mean envelope radius may be calculated from the other parameters by

$$\langle r_{env} \rangle = \frac{4\pi\rho(r_1)}{M_{env}} \{r_2^2 r_3^2 \left(\frac{1}{2} + \ln\left(\frac{r_4}{r_3}\right)\right) - \frac{1}{4}\left(r_1^4 + r_2^4\right)\} . \qquad (4.4)$$

N_{tot} is the total number of zones the star is divided into.

E_{net} is a measure of the energy of the explosion. It is the sum of the internal energy, the kinetic energy, the gravitational potential energy, the radiated energy, and the radioactive energy yet to be released (via Ni-Co-Fe decay), summed over the entire star. E_{net} is expressed in units of ergs. E_{net} should remain constant throughout the explosion, and in fact is used as a check on the accuracy of the calculations. E_{net} must be positive if the supernova is to leave no central remnant (i.e. completely disrupt the star).

$\bar{v}$ is defined as $(2E_{net}/M_{tot})^{\frac{1}{2}}$. It has the dimensions of velocity, and since at late times E_{net} is almost entirely in the form of kinetic energy of expansion, $\bar{v}$ is termed the characteristic expansion velocity. Note that for the case of a uniform density, homologously expanding sphere the characteristic velocity is $\bar{v} = (3/5)^{\frac{1}{2}} v_s = 0.775\ v_s$, where v_s is the velocity at the surface of the sphere.

The core of each model is broken up into forty zones. The zones in the interior are larger (in mass) than the zones near the surface as the temperature and density gradients tend to be smaller in the interior. The innermost zone is typically about three times as massive as the outermost

core zone. The envelope is broken into zones after being shocked, each zone being about 0.020 $M_\odot$, comparable to the mass of the outermost core zone.

It is necessary to have a criterion to indicate whether or not the zoning is sufficiently fine to maintain numerical accuracy. To this end the parameter E_{net} is used. Ideally E_{net} should remain constant over the entire run but in practice it varies slightly, typically by about one part in a million per iteration, and by about one part in 300 over an entire run. This variation arises from using finite (rather than infinitesimal) zones, finite time steps (iterations), and from accumulated roundoff error in the computations. Considering the uncertainties in some of the input parameters (M_{incin} for example), there seems to be little to be gained by increasing the number of zones in order to obtain greater accuracy.

Opacity Functions

As noted in the tables three models (B3, B4 and D3) do not make use of the standard assumption of a constant opacity. Two different prescriptions are tested: a frequency dependent opacity which is larger in the ultraviolet than at visible wavelengths, and a temperature dependent opacity which is reduced below 6000 K to reflect the effects of recombination.

The frequency dependent opacity is motivated by the observed ultraviolet flux deficiency. It is parametrized as follows. The scattering opacity $\kappa_{\nu s}$ is set constant at a value κ_s (typically 0.1 cm^2-g^{-1}). The absorption opacity $\kappa_{\nu a}$ is represented as a step function; it is set to a constant κ_a at wavelengths below 4000 A, and to zero at longer wavelengths. The assumption of local thermodynamic equilibrium is then invoked to permit calculation of the Rosseland mean opacity, transforming the

frequency dependence into a temperature dependence. Specifically

$$\kappa^{-1} = \kappa_s^{-1} I \int_0^{x_0} e^x (e^x-1)^{-2} x^4 dx + I \int_{x_0}^{\infty} \frac{e^x (e^x-1)^2 x^4 dx}{\kappa_a (1-e^{-x}) + \kappa_s} , \qquad (4.5)$$

where

$$x_0 = \frac{35{,}969.66\ K}{T}$$

and

$$I^{-1} = \int_0^{\infty} e^x (e^x-1)^{-2} x^4 dx = \frac{4\pi^4}{15} .$$

For the specific values $\kappa_s = 0.1\ cm^2\text{-}g^{-1}$ and $\kappa_a = 1.0\ cm^2\text{-}g^{-1}$ (as used in Model B3) this results in $\kappa \cong 1.04\ cm^2\text{-}g^{-1}$ for $T >> 10^5$ K and $\kappa \cong 0.1\ cm^2\text{-}g^{-1}$ for $T << 10^4$ K. A similar prescription is used for Model B4 except that both κ_s and κ_a (and hence κ) are reduced by a factor of four ($\kappa_s = 0.025\ cm^2\text{-}g^{-1}$, $\kappa_a = 0.25\ cm^2\text{-}g^{-1}$).

Model D3 makes use of an explicitly temperature dependent opacity. The prescription is

$$\kappa = 0.10\ cm^2\text{-}g^{-1} \quad , \quad \text{for } T > 6000\ K ;$$

$$\kappa = 0.10 \left(\frac{T}{6000\ K}\right)^{5.67887} cm^2\text{-}g^{-1} \quad , \quad \text{for } 4000\ K < T < 6000\ K;$$

$$\kappa = 0.01\ cm^2\text{-}g^{-1} \quad , \quad \text{for } T < 4000\ K . \qquad (4.6)$$

The motivation behind this choice is that significant electron recombination may occur near 5000 K. A reduction of the opacity in this temperature range may have the desirable effect of causing the photosphere to recede when such temperatures are encountered, about twenty to thirty days after

maximum light.

This prescription, like the frequency dependent one, is at best qualitative. Extensive recombination leads to domination by the bound-bound transitions (line absorption), which is certainly frequency dependent and subject to the effect of Doppler enhancement.

Group A Models

This group comprises two models (A1 and A2) which are initially compact, i.e. bare white dwarf stars. These models serve as standards for comparison with the various extended models. Model A1 starts with $\sim 1.0\ M_\odot$ of C/O surrounded by $0.4\ M_\odot$ of helium. The central density is 3.0×10^9 g-cm^{-3} and the star is isothermal at 5×10^7 K. The supernova is initiated by incinerating the C/O. This model is similar to the best-fitting models of both Chevalier (1981) and Sutherland and Wheeler (1984). The distinction between models A1 and A2 lies in the amount of radioactive ^{56}Ni created. In model A1 all the incinerated matter becomes ^{56}Ni, as was assumed in both of the above papers. Model A2 follows the results of Nomoto (1984) in that only $\sim$ 60% of the incinerated matter becomes ^{56}Ni, the rest forming other (non-radioactive) iron-group nuclei. Otherwise models A1 and A2 are identical. The opacity in both models is 0.1 cm^2-g^{-1}.

Group B Models

There are four models in group B which all start with the same cores, composed of $1.264\ M_\odot$ of C/O surrounded by $0.152\ M_\odot$ of helium. The central density of the progenitors is 1.07×10^{10} g-cm^{-3} and they are isothermal at 1.58×10^8 K. These values closely approximate the conditions in Model F of Nomoto (1982a) at the onset of carbon ignition (although note that Nomoto

1984 reports a revised carbon ignition density of 3×10^9 g-cm^{-3}). In each group B model 1.1 $M_\odot$ is incinerated and it all becomes ^{56}Ni.

Model B1 starts with an envelope of 0.40 $M_\odot$, constant in density from a radius of 1.0×10^{10} cm out to 1.3015×10^{11} cm, beyond which the density varies as r^{-4} out to the surface at 8.33×10^{12} cm. This envelope was chosen to reproduce the surface features of a member of the class of R Cor Bor stars, as described by Saio and Wheeler (1983). The surface temperature is 7000 K and the luminosity is $10^{4.5}$ $L_\odot$. The surface density and gradient are chosen to agree with the theoretical calculations of Saio (1983). It was first suggested by Wheeler (1978) that the class of R Cor Bor stars might be viable supernova progenitors.

As the envelope radius of model B1 is relatively small compared to the models of Lasher (1975), the hump of the light curve for model B1 is primarily due to radioactive decay, with the envelope of secondary importance. Model B2 examines the effect of an envelope of larger initial size (but similar mass) to that of model B1. To this end the characteristic envelope radii of model B2 are ten times those of model B1, with everything else unchanged.

Model B3 is identical to model B2 except for the use of a frequency-dependent opacity, as described earlier in this chapter. At high temperatures ($T \gg 10^5$ K) the opacity is ~ 1.04 cm^2-g^{-1}. At low temperatures ($T \ll 10^4$ K) the opacity is ~ 0.10 cm^2-g^{-1}.

Model B4 is identical to model B3 except that the opacity is lower by a factor of four under all conditions.

Group C Models

The six group C models start with identical cores of 1.385 $M_\odot$ of C/O, with a central density of 3.0×10^9 g-cm^{-3} and isothermal at 1.0×10^8 K. This central density is the carbon ignition density reported by Nomoto (1984). The group C models each incinerate 1.20 $M_\odot$. Models C1 through C4 convert all incinerated matter to ^{56}Ni, whereas model C5 converts only 0.7 $M_\odot$ to ^{56}Ni. Radioactivity is absent in model C6, to show the effect of the envelope alone. The opacity for all group C models is 0.1 cm^2-g^{-1}.

Models C1 through C3 examine the effect of different envelope density profiles. All three envelopes have the same mass (0.615 $M_\odot$) and same radius (5.0×10^{13} cm). The envelope in model C1 is of constant density throughout. The density of the envelope of model C2 varies as r^{-2} throughout. Model C3 is a composite of all three density profiles: it is constant out to 5×10^{11} cm, varies as r^{-2} from there out to 5×10^{12} cm, and then varies as r^{-4} out to 5×10^{13} cm. It is not feasible to maintain the r^{-4} profile throughout the entire envelope; the density in the inner regions would be unreasonably large.

Model C4 has a density profile similar to that of model C3 but is more compact; the outer radius is only 8.45×10^{12} cm. This value was chosen (like model B1) as appropriate for an R Cor Bor star. Thus model C4 is a 'realistic' model, as it conforms to a known class of stars considered to be possible supernova progenitors.

Model C5 is identical to model C4 apart from the fact that only 0.70 $M_\odot$ of ^{56}Ni is created.

Model C6 is also similar to model C1 except that no ^{56}Ni is present at all (i.e. the radioactivity is turned off). As is seen in the next chapter the light curve for this model renders it unacceptable as a viable model.

Group D Models

The cores of the progenitors of the five group D models are identical to those of the group C models. The difference is that only 1.1 $M_\odot$ are incincerated as opposed to 1.2 $M_\odot$ as in the group C models. The envelopes are only half as massive as those in group C (i.e. 0.308 $M_\odot$). The envelope profiles are analogous to that of model C3.

Model D1 has an initial radius of 5.0×10^{13} cm and burns all 1.1 $M_\odot$ of incinerated matter to ^{56}Ni. The opacity is constant at 0.1 $cm^2\text{-}g^{-1}$.

Model D2 turns only 0.625 $M_\odot$ to ^{56}Ni, otherwise it is identical to model D1.

Model D3 is the same as model D2 except that a temperature dependent opacity function is used (discussed earlier in this chapter). The opacity is 0.1 $cm^2\text{-}g^{-1}$ above 6000 K and is reduced at lower temperatures.

Model D4 has an initial radius of 8.45×10^{12} cm, like model C4. Model D4 has an opacity of 0.1 $cm^2\text{-}g^{-1}$ and burns 1.1 $M_\odot$ to ^{56}Ni.

Model D5 only has 0.625 $M_\odot$ of ^{56}Ni but is otherwise identical to model D4.

Summary

The parameter space of possible models is much too large to explore with any degree of completeness. There is little point in merely searching for a fit between a given model and the observations; even in a relatively restricted three parameter space. Lasher (1975) was able to achieve such a fit, but this did not imply that the model was correct. The models examined in this work are of two types: models B1, C4, C5, D4, and D5 reproduce the observed properties of typical R Cor Bor stars, with various assumptions about their mass and structure and an assumed value for the opacity of 0.1 cm^2-g^{-1}. (As seen in the next chapter a smaller value for the opacity would produce better fits.) The remaining models are variations on these which are designed to explore the qualitative effects of changes in the various parameters. These models were given significantly larger envelope radii than the R Cor Bor models in part to exaggerate these differences.

The models were hydrodynamically evolved from ignition out to 5×10^6 seconds later by the program BOMB, which implements the methods outlined in Chapter III. The results of these calculations are the subject of the next chapter.

CHAPTER V

RESULTS

Each of the models described in the previous chapter was numerically evolved to about fifty days after ignition, when the SN I light curve undergoes the hump-tail transition. For each model characteristic density and velocity profiles are presented. Also recorded as functions of time were the photospheric radius, the velocity at the photosphere, and the luminosity. From these data certain other quantities were derived, notably the colour temperature, the luminosity in the blue band and the colour index.

Density Profiles

The density profiles for the various models are presented in Figures 5-1 to 5-10. The profiles of models A1 and A2 (Figure 5-2) show discontinuities at mass fraction 0.71, where the incineration stopped. Model A2 shows a second discontinuity at mass fraction 0.42, at the outer edge of the radioactive region. In the outer, non-incinerated regions both profiles drop steeply ($\rho \propto r^{-16}$). This is in sharp contrast to the density profiles assumed in most analytic models (where typically ($\rho \propto r^{-7}$).

The profiles of the envelope models are all qualitatively similar: a significant fraction of the mass is concentrated in a density peak just inside the original core/envelope boundary. Although they are not plotted here, the temperature and entropy profiles also show dis-

continuities at the core/envelope boundary, but in the opposite sense (greater in the envelope than in the core). Of the three, the entropy profile is the most fundamental. The entropy discontinuity exists even prior to ignition. After the primary shock passes through the envelope, the system undergoes adiabatic expansion. Radiative diffusion eventually smooths out the temperature discontinuity, but the entropy and density discontinuities remain. (Note that for a radiation dominated system the entropy is inversely proportional to the density.)

The density profile of model D5 as a function of time is shown in Figures 5-1 and 5-6. At 10^3 seconds after ignition the shock has not yet reached the stellar surface, but the characteristic shape of the profile is already established. Hardly any change in the profile occurs after 10^5 seconds, as the supernova settles into homologous expansion.

The linearity of the outmost parts of the profiles in Figures 5-7 to 5-10 indicate a power-law relationship between density and radius ($\rho \propto r^{-n}$). As noted above, the A group models show $n \sim 16$. Models C1 and C6 show $n \sim 10$; model C2 shows $n \sim 8$; and the remainder all show $n \sim 6$. In all the envelope models the profiles flatten out in the inner regions of the envelope. These values for n are correlated with the pre-shock density profiles. As the constant density envelope models (C1 and C6) are the most difficult to justify astrophysically, the remaining envelope models (n=6 to n=8) agree nicely with the standard value of n=7 used in analytic work. However, the bare white dwarf models do not agree in this regard. This may be due in part to the abrupt cessation of the deflagration wave in these models.

Velocity Profiles

The velocity profile for model D5 at various times is shown in Figure 5-11. At 10^3 seconds after ignition the primary shock is still below the stellar surface, at mass fraction 0.96. The reverse shock at mass fraction 0.50 is clearly visible. Between the reverse shock and the core/envelope boundary (mass fraction 0.82) the velocity profile is very flat; this corresponds to the matter compressed into the density peak. After 10^4 seconds the velocity profile shows no significant change, allowing the supernova to settle in to a homologous expansion.

The velocity profiles of models A1 and A2 do not show the flat plateaux near 8×10^8 cm-s^{-1} that mark the envelope models. As will be seen in Figures 5-19 to 5-21 these plateaux serve to 'hold up' the photospheric velocity at 8000 km-s^{-1} at least until the hump-tail transition.

Photospheric Radius

The photosphere is defined in these models to be at an optical depth of $\tau = 2/3$ below the surface (i.e. 2/3 of a photonic mean free path). This is the Eddington approximation; it assumes a grey atmosphere (frequency independent opacity) and locates the point where the local temperature is equal to the star's effective temperature (see e.g. Mihalas 1978).

The photosphere is located by numerical integration of the optical depth:

$$\frac{2}{3} = \tau(r_{ph}) = \int_{r_{ph}}^{r_s} \kappa(r)\rho(r)dr \qquad (5.1)$$

If the opacity is frequency-dependent then the Rosseland mean opacity is used. The photospheric radius for each model as a function of time is plotted in Figures 5-16 to 5-18. According to Branch et al (1983) the photospheric radius of SN 1981b reached a maximum around 4×10^6 seconds after ignition and decreased by approximately 20% by 5×10^6 seconds. The only model to show such a decrease is model B4, due to the use of a frequency-dependent opacity which decreased at late times. The opacity for model D3 dropped abruptly at 3.5×10^6 seconds (simulating electron recombination); however, the photospheric radius declined too abruptly and the nebula quickly became optically thin.

A comparison of models B3 and B4 shows the sensitivity of the photospheric radius to the opacity. A suitable reduction in the opacity could cause the other models to maximise their photospheric radii at 4×10^6 seconds, although this would have adverse effects on the velocity curves described below. In any case the observational data on photospheric radii are not extensive enough to provide sound constraints on the theoretical models.

Velocity at the Photosphere

For each model the velocity of the matter at the photosphere as a function of time is plotted in Figures 5-19 to 5-21. Branch (1981; 1982) has reported two values: $\sim 1.1\text{-}1.2 \times 10^9$ cm-s^{-1} at maximum light ($\sim 1.3 \times 10^6$ seconds), and $\sim 8 \times 10^8$ cm-s^{-1} some 45 days later ($\sim 5.5 \times 10^6$ seconds). The group A models fit well at maximum light, but drop off too quickly there-

after. To keep the velocity high out to 5.5×10^6 seconds would require an increase in the opacity - contrary to what is indicated by the photospheric radius curves. Models B1, B2 and B3 give acceptable velocities at both times, because the photosphere lingers in the density peak moving at 8000 km-s^{-1}; but this is not the case for model B4 which has a reduced opacity. While relatively small opacities are better for matching the photospheric radius, relatively large opacities are needed to match the observed velocities. (This dilemma could be resolved by increasing the amount of incinerated mass to enhance the velocity profiles.)

Models C1, C2 and C3 show the effect of various envelope density profiles. Models C1 and C2 have somewhat high velocities at maximum light and low velocities later on. To resolve this would require an opacity which increases as time goes on, contrary to what the radius curves and the light curves (discussed later) suggest. Model C3 is superior in this regard, fitting well at both times, as do the group D models (except D3). Thus the composite envelope density profile provides the most viable models.

Luminosity

The bolometric luminosity for the various models is plotted in Figures 5-22 to 5-24. No observational data on the bolometric luminosity are available, but the graphs provide some insight into the models. All the models (except C6) show peaks in the luminosity at $1\text{-}2 \times 10^6$ seconds due to radioactive heating of the nebula. The envelope models also show very bright precursor peaks formed at $\sim 10^5$ seconds by shock heating of

the envelope. Model C6 exhibits this effect in the absence of radioactive heating. The envelope is seen to have little effect on the luminosity past the time of maximum light ($\sim 1.3 \times 10^6$ seconds). The bright, narrow precursor peaks emit primarily X-rays, although as will be seen later there is also significant radiation in the blue band. Unfortunately, at present there is little chance of directly observing the presence (or absence) of this X-ray flash which is the most identifiable characteristic of the envelope models.

Colour Temperature

The effective temperature follows from the condition that blackbody photospheric emission provides the required luminosity. Hence

$$T_e = (L/4\pi R_{ph}^2 \sigma)^{\frac{1}{4}} \qquad (5.2)$$

By the Eddington approximation this should also be the local matter temperature at the photosphere; in practice the two differ by several percent. This is due in part to the coarse zoning. Also, at late times significant gamma-ray deposition occurs above the nominal photosphere, violating the Eddington approximation.

If the supernova spectrum were truly blackbody then the colour temperature would equal the effective temperature. In fact the spectrum is complex, but two simplified descriptions are used here to estimate the colour temperature. The first (method I) simply assumes a blackbody spectrum, giving a colour temperature T_I equal to T_e. These temperatures are plotted in Figures 5-25 to 5-27. The second description (method II)

has negligible flux below 4000 Å and a Planckian spectrum at longer wavelengths. As this method takes account of the observed ultraviolet deficiency, it should provide better results than does the more straightforward method I. Under method II the colour temperature (T_{II}) is

$$T_{II} = T_I \left(\frac{15}{\pi^4} \int_0^{X_o} \frac{x^3 dx}{e^x - 1} \right) \qquad (5.3)$$

where $X_o = 35{,}970\ K/T_I$. As this method implies a redistribution of flux from the ultraviolet into the visible, it results in higher colour temperatures than does method I. The method II temperatures are plotted in Figures 5-28 to 5-30.

The method I temperatures at maximum light are all too low compared to the estimate of 17,000 ± 3,000 for SN 1981b (Branch, 1982). At maximum light no model exceeds 11,000 K. The method II temperatures are more encouraging: models A1, B1, B2, B4, C1 to C4, D1, and D4 all have a temperature near 13,000 K at maximum light. (These models all have $M_{rad} = M_{incin} \gtrsim 1\ M_\odot$.) The models with $M_{rad} \simeq 0.60\ M_{incin}$ (models A2, C5, D2, D3, and D5) all have significantly lower temperatures at maximum light. The temperatures may be raised somewhat by a reduction in the opacity, but it seems that it requires $M_{rad} \gtrsim 1\ M_\odot$ to bring the temperature up to Branch's estimate. This amount of ^{56}Ni appears incompatible with the deflagration calculations of Nomoto (1984).

Bolometric Magnitude

The bolometric magnitude diagrams (Figures 5-31 to 5-33) plot the luminosity on the stellar magnitude scale, a negative logarithmic

scale retained by astronomers primarily for historic reasons. Using the definitions in Allen (1976) it follows:

$$M_{BOL} = -18.793 - 2.5 \log (L_{43}) \qquad (5.4)$$

where L_{43} is the luminosity in units of 10^{43} erg-s^{-1}. (All logarithms in this chapter are common or base ten logarithms.)

The bolometric magnitude curves naturally show similar features to the luminosity curves in Figures 5-22 to 5-24. The most prominent feature in the envelope models are the very bright precursor peaks which in some models reach magnitude -25. The rising side of the precursor peaks is nearly instantaneous and has been omitted from the figures for the sake of clarity. The decline in the bolometric magnitude after maximum light is much more gradual than the decline in blue light (see below), showing that the latter is governed largely by the change in the temperature and colour index.

Blue Magnitude

Supernova light curves are often measured in the standard blue waveband centered at 4400 Å. Following Allen (1976), the blue magnitude is given by

$$M_B = -2.5 \log(F_B) + 22.775 - 5 \log(R/R_\odot) \qquad (5.5)$$

where F_B is the monochromatic flux at 4400 Å. This expression may be reduced to

$$M_B = -21.402 + 2.5 \log(e^X - 1) - 5 \log(R_{15}) \qquad (5.6)$$

where $x = 32{,}699.7\ K/T$ and R_{15} is the photospheric radius in units of 10^{15} cm. Since the parameter 'x' is temperature dependent, two values for the blue magnitude may be derived, depending on whether method I or II is used to determine the temperature. The method I blue magnitudes are plotted in Figures 5-34 to 5-36 while the method II results are plotted in Figures 5-37 to 5-39. Also plotted in the figures are the observed blue magnitudes of SN 1981b taken from Buta and Turner (1983). It should be noted that there is considerable uncertainty in the distance modulus to the host galaxy (NGC 4536): a different distance modulus would shift the measurements en masse vertically. Buta and Turner themselves argue for a distance modulus of 30.0 magnitudes, corresponding (via equation 1.1) to a Hubble constant of 110 $km\text{-}s^{-1}\text{-}Mpc^{-1}$. This value is not consistent with deflagrating white dwarf supernova models. Sandage and Tamann (1985) and Branch (1985) argue for a Hubble constant near 50 $km\text{-}s^{-1}\text{-}Mpc^{-1}$. The chosen distance modulus of 31.5 magnitudes for SN 1981b corresponds to H=55 $km\text{-}s^{-1}\text{-}Mpc^{-1}$, half of the Buta and Turner value.

None of the method I light curves are bright enough at maximum light, and the curves do not decline fast enough thereafter. The method II results are better in both regards, consistent with the better spectral fit. The discussion below focusses on the method II results.

The light curve of model A1 comes closest to fitting the observations. This in itself is not surprising as it was chosen to match the best-fitting models of both Chevalier (1981) and Sutherland

and Wheeler (1984). The light curve of model A2 (0.6 $M_\odot$ of ^{56}Ni) is dimmer and runs parallel to that of model A1. Model A2 would fit the observations if the Hubble constant were 70 km-s^{-1}-Mpc^{-1}.

Using method II the envelope models as a class tend to fit well at maximum light but there are significant problems at other times. One problem is that the light curves do not decline steeply enough after maximum light. This effect is correlated with mass; the heavier the model, the flatter is the light curve. This is because the envelopes serve as insulating blankets which slow down the cooling of the system. This effect is also seen in the colour index curves (see below). A smaller opacity would mitigate this effect, but then maximum light would occur earlier and would be brighter (compare models B3 and B4, or see Arnett, 1982). A variable opacity which dropped after maximum light would be better, but at late times the luminosity is controlled by the deposition rate more so than by the opacity.

The second and more serious problem with the envelope models is the existence of the precursor peaks. The observations (Pskovskii 1977) show no precursor peak within four magnitudes of the main peak. There is good evidence that Type I supernovae produce a significant amount of ^{56}Ni, thus the main peak of the light curve is powered at least in part by radioactivity. For envelope models to be viable therefore, requires that the precursor peak either be very small, or else it must be superimposed on the radioactivity peak. The latter event would require a very large envelope mass and opacity, several times larger than in model

C6 which peaks much too early. As will be seen below the evidence of the colour index curves rules out such a model. Thus if an envelope exists it must be small ($R \leq 10^{12}$ cm) so that the precursor peak is sufficiently dim and short-lived to have eluded detection so far.

Colour Index

The colour index B-V is the difference in the light curves between the blue and the visible wavebands. Unlike the light curves, the colour index has the advantage of being independent of the Hubble constant. It is a function solely of the temperature and is given by

$$B\text{-}V = -0.562 + 2.5 \log \left(\frac{e^X - 1}{e^Y - 1} \right) \qquad (5.7)$$

where X = 32,699.7 K/T and Y = 26,159.8 K/T, corresponding to the wavelengths 4400 Å and 5500 Å, respectively. The colour index depends on the method used to determine the colour temperature. The method I colour index curves are plotted in Figures 5-40 to 5-42, while the method II curves are plotted in Figures 5-43 to 5-45.

The method I colour index curves are all too flat: they are too red at maximum light and become too blue thereafter. The method II curves are steeper: they fit well at maximum light although they also are generally too blue at later times. The slope of the curves depends on mass: the group A models (no envelope) are steepest and provide the best fit to the data, while groups B, D, and C are progressively both flatter and more massive. This is a consequence of the fact that the temperature

depends on the deposition rate, which in turn depends on the mass and the gamma-ray opacity. Since the gamma-ray opacity is fixed at 0.03 cm^2-g^{-1}, the lighter stars become optically thin to the gamma-rays before the heavier stars do, hence the deposition rate drops faster for the lighter stars.

The major uncertainties in the deflagrating white dwarf supernova models are the amount of ^{56}Ni produced and the thermal opacity. The slope of the colour index curves is insensitive to both of these parameters. As can be seen by comparing models A1 and A2, or models C4 and C5, or B4 and D5, a change in M_{rad} only shifts the colour index curves without changing the slope. Similarly, the curves for the models differing only in the opacity (B3 and B4) are shifted diagonally. The conclusion is that the colour index curves provide good evidence against the envelope models, as the bare white dwarf models of one Chandrasekhar mass provide the best fit.

Summary

The models simulating R Cor Bor stars (models B1, C4, C5, D4, and D5) are not viable as standard Type I supernovae as they show bright, early precursor peaks which would certainly be seen if they existed. Furthermore, if the gamma-ray opacity is correct then the colour index curves clearly indicate that little or no envelope can exist. If any envelope exists, it should be lighter than $\sim 0.3\ M_\odot$ (group D models) and have a radius of $\sim 10^{12}$ cm or less.

A comparison of the bare white dwarf models shows little to choose between them. Model A1 gives a light curve corresponding to a Hubble constant of H = 50 km-s^{-1}-Mpc^{-1}, whereas model A2 corresponds to H = 70 km-s^{-1}-Mpc^{-1}. The colour index curve favours model A1 at maximum light but favours A2 at later times. Branch's fit of 17,000±3000 K. to the temperature at maximum light clearly favours model A1. There are enough uncertainties in the calculations that both models (1.0 or 0.6 $M_\odot$ of ^{56}Ni) remain viable as Type I supernovae.

Figures 5-1 to 5-5

Density profiles plotted against mass fraction. The dependent variable is log (ρt^3), which remains invariant under homologous expansion. Figure 5-1 shows the time evolution of model Q5, with curves 3, 4, 5, 6 and 7 representing times of 10^3, 10^4, 10^5, 10^6, and $.5 \times 10^7$ seconds after ignition, respectively. The expansion is homologous from about 10^5 seconds onwards. Figures 5-2 to 5-5 show the late-time (homologous) profiles for all the models.

Figure 5-1

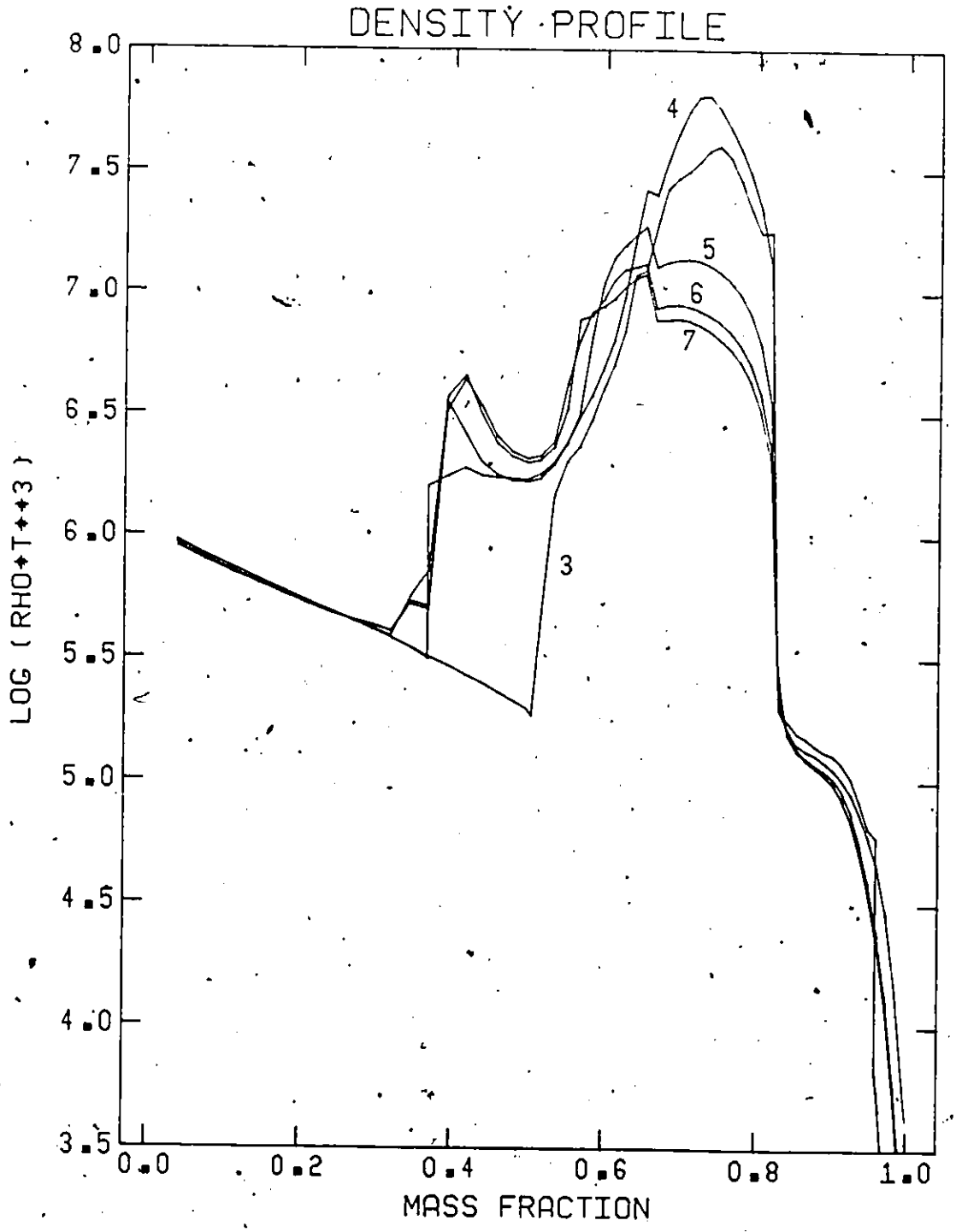
DENSITY PROFILE
LOG (RHO*T**3)
MASS FRACTION
8.0
7.5
7.0
6.5
6.0
5.5
5.0
4.5
4.0
3.5
0.0
0.2
0.4
0.6
0.8
1.0
3
4
5
6
7

Figure 5-2

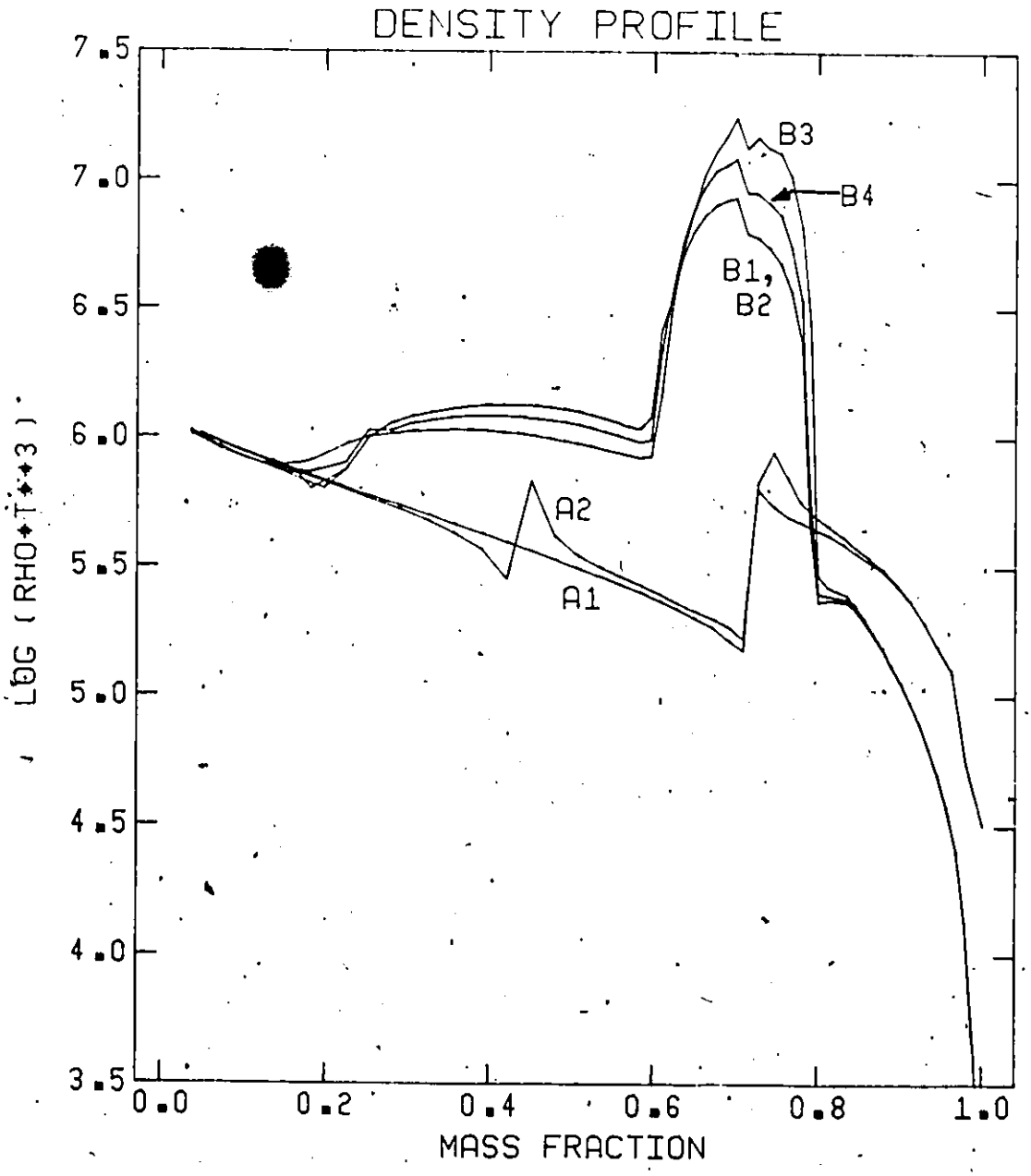
DENSITY PROFILE
7.5
7.0
6.5
6.0
5.5
5.0
4.5
4.0
3.5
LOG (RHO*T**3)
0.0
0.2
0.4
0.6
0.8
1.0
MASS FRACTION
B3
B4
B1,
B2
A2
A1

Figure 5-3

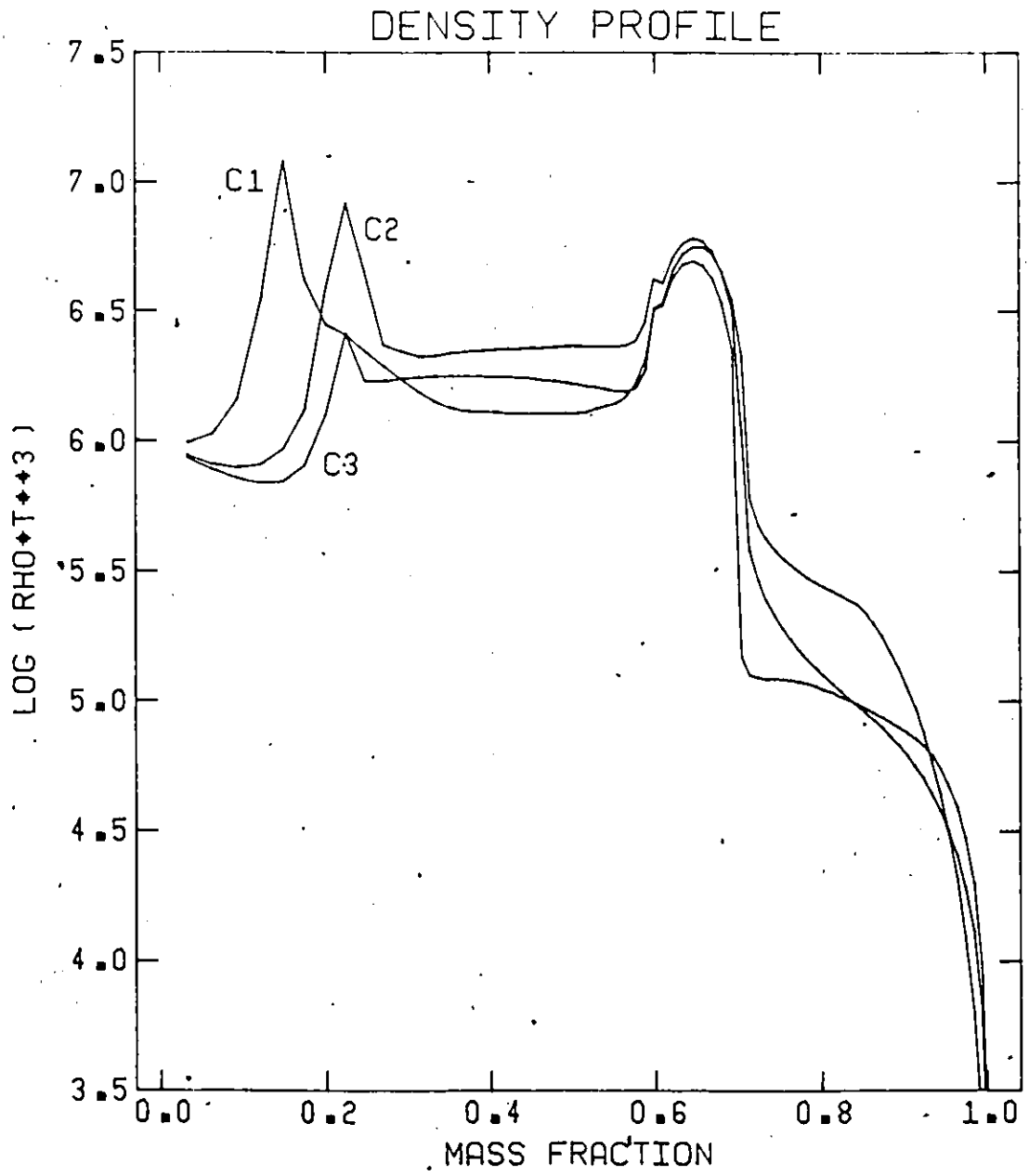
DENSITY PROFILE
C1
C2
C3
LOG (RHO◆T◆◆3)
7.5
7.0
6.5
6.0
5.5
5.0
4.5
4.0
3.5
0.0
0.2
0.4
0.6
0.8
1.0
MASS FRACTION

Figure 5-4

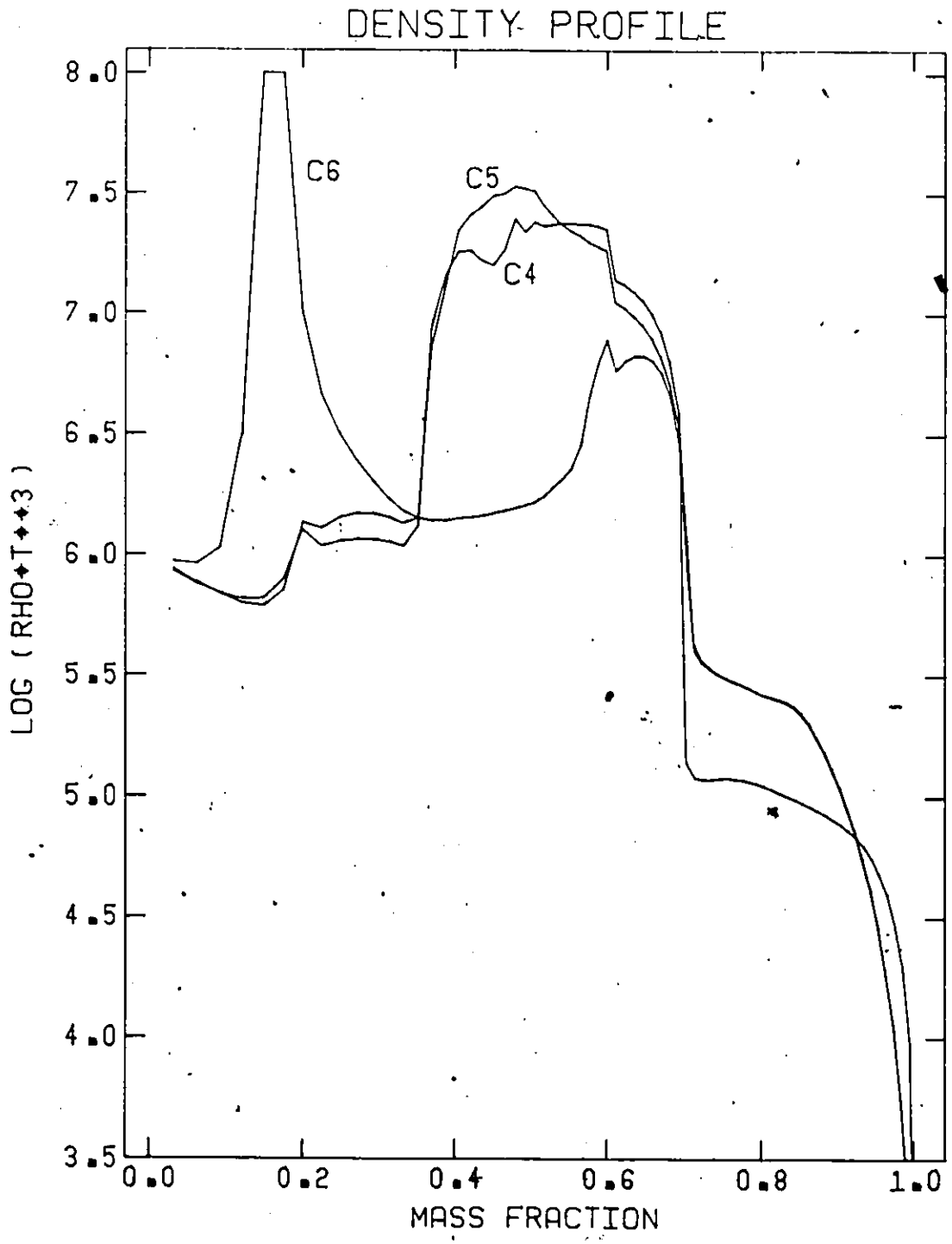
DENSITY PROFILE
C6
C5
C4
LOG (RHO*T**3)
8.0
7.5
7.0
6.5
6.0
5.5
5.0
4.5
4.0
3.5
0.0
0.2
0.4
0.6
0.8
1.0
MASS FRACTION

Figure 5-5

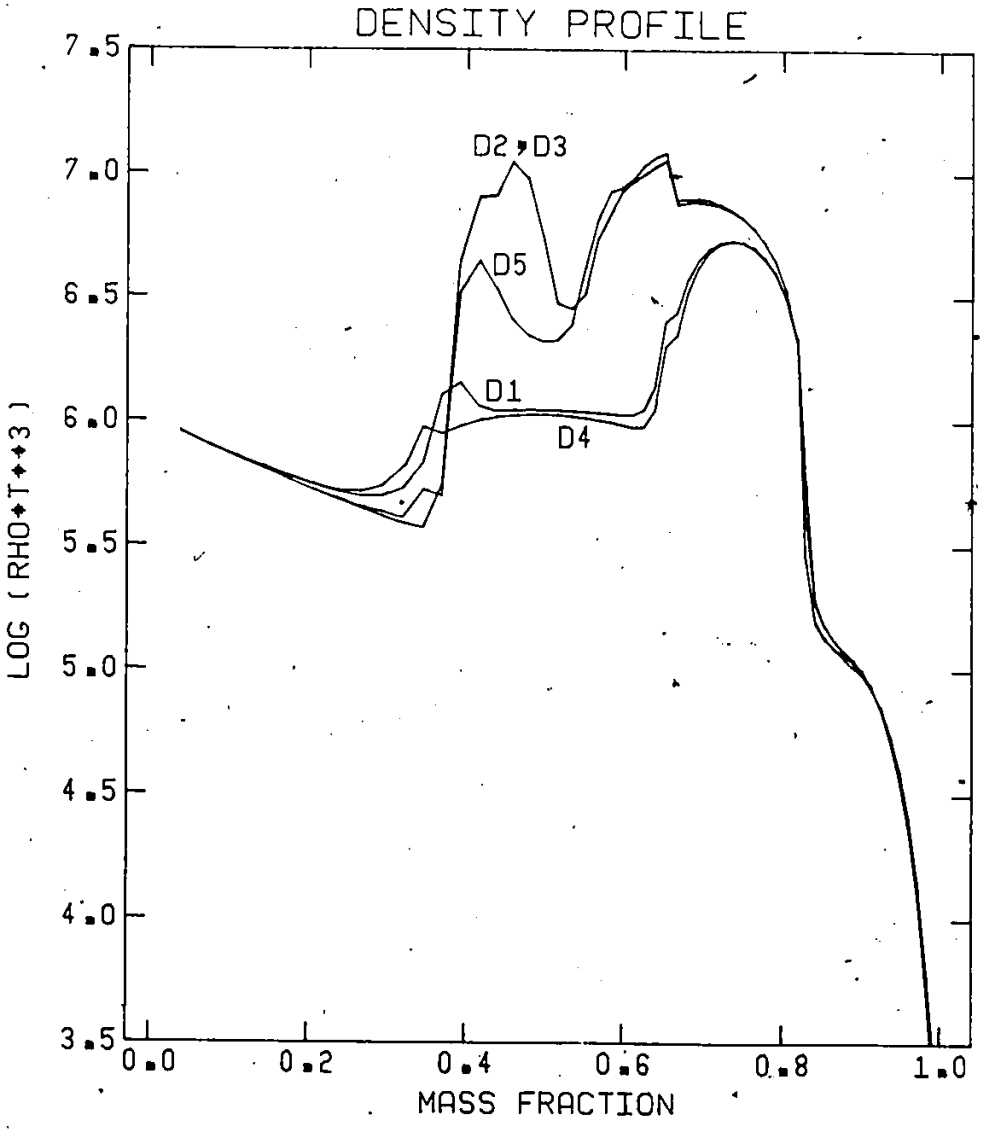
DENSITY PROFILE
7.5
7.0
6.5
6.0
5.5
5.0
4.5
4.0
3.5
LOG (RHO*T**3)
D2,D3
D5
D1
D4
0.0
0.2
0.4
0.6
0.8
1.0
MASS FRACTION

Figures 5-6 to 5-10

Density profiles plotted against log (r/t). For a homologously expanding system the independent variable reduces to log (v). Figure 5-1 shows the time evolution of model D5, with curves 3, 4, 5, 6 and 7 representing times of 10^3, 10^4, 10^5, 10^6, and $.5x10^7$ seconds after ignition, respectively. Figures 5-7 to 5-10 show the late-time (homologous) profiles for all the models.

Figure 5-6

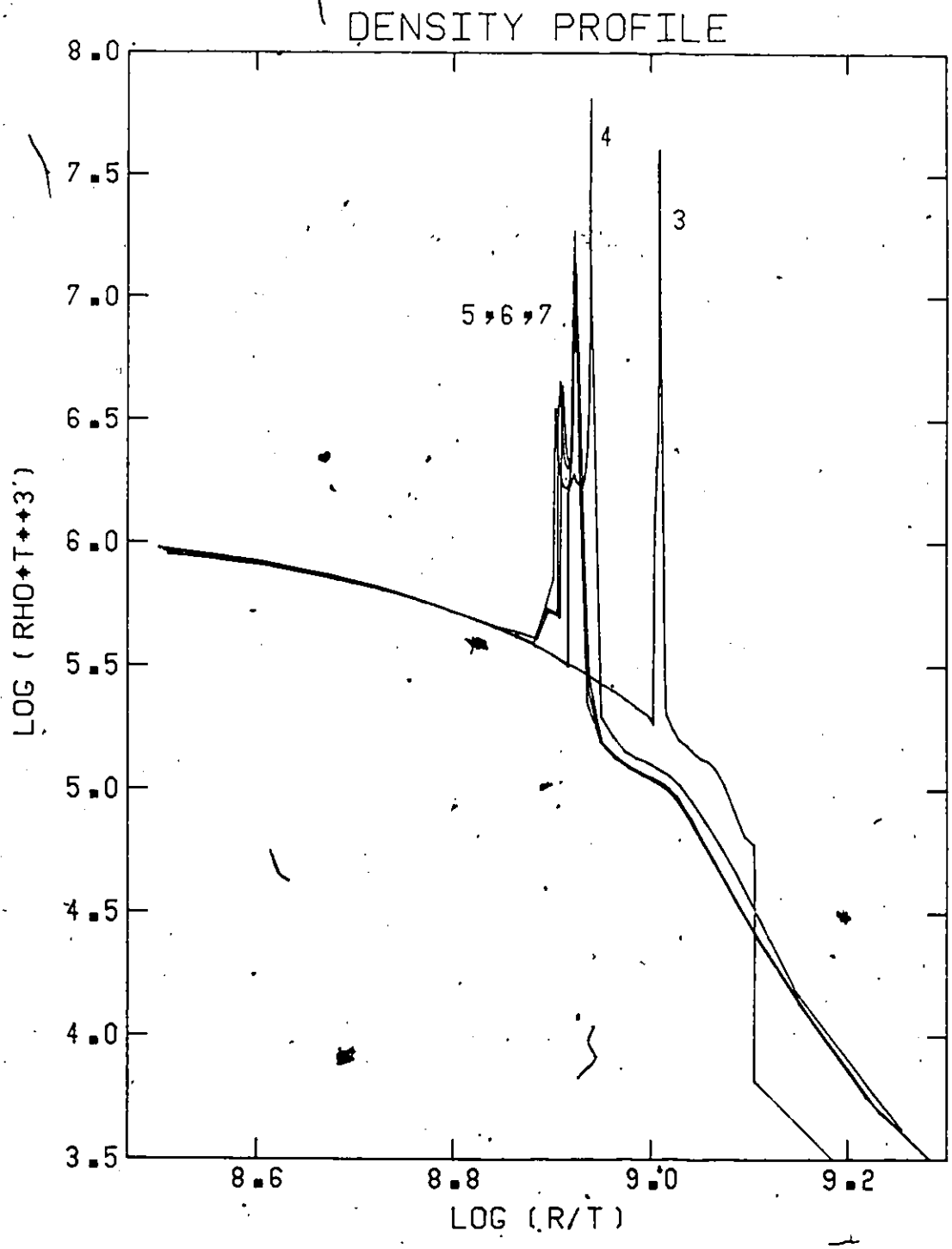
DENSITY PROFILE
8.0
7.5
7.0
6.5
6.0
5.5
5.0
4.5
4.0
3.5
LOG (RHO*T**3)
8.6
8.8
9.0
9.2
LOG (R/T)
4
3
5,6,7

Figure 5-7

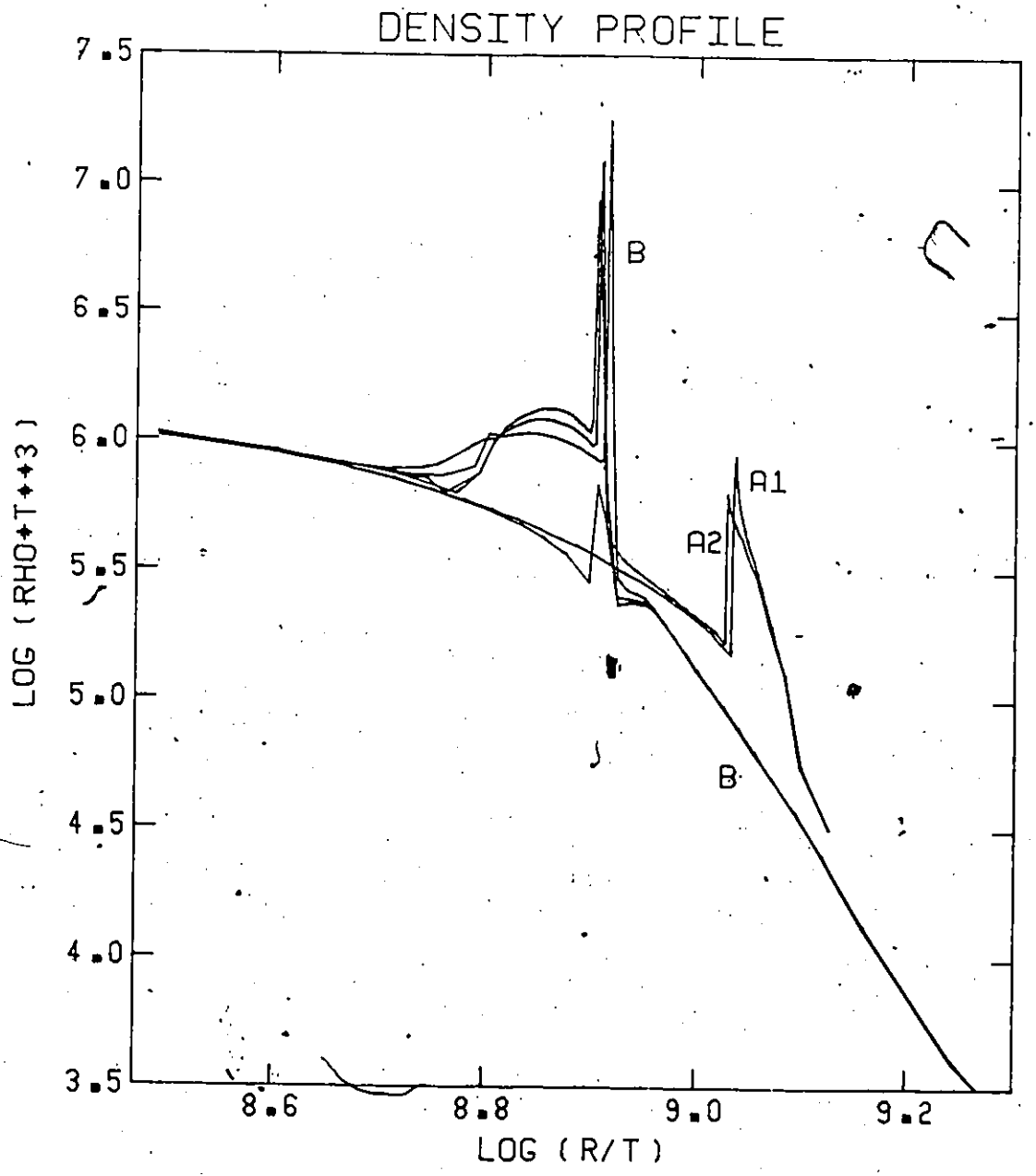
DENSITY PROFILE
7.5
7.0
6.5
6.0
5.5
5.0
4.5
4.0
3.5
LOG (RHO*T**3)
B
A1
A2
B
8.6
8.8
9.0
9.2
LOG (R/T)

Figure 5-8

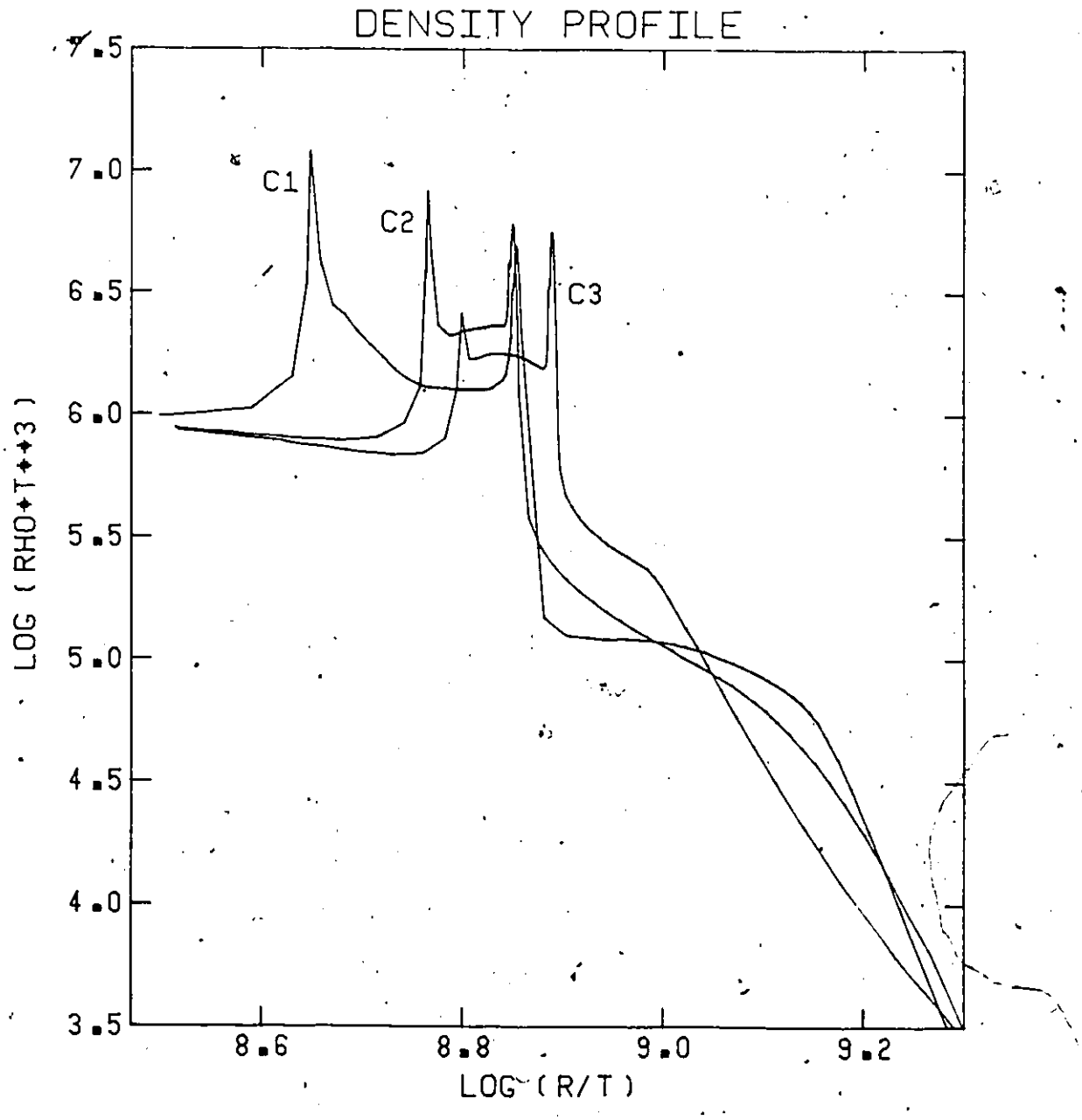
DENSITY PROFILE
C1
C2
C3
7.5
7.0
6.5
6.0
5.5
5.0
4.5
4.0
3.5
LOG (RHO*T**3)
8.6
8.8
9.0
9.2
LOG (R/T)

Figure 5-9

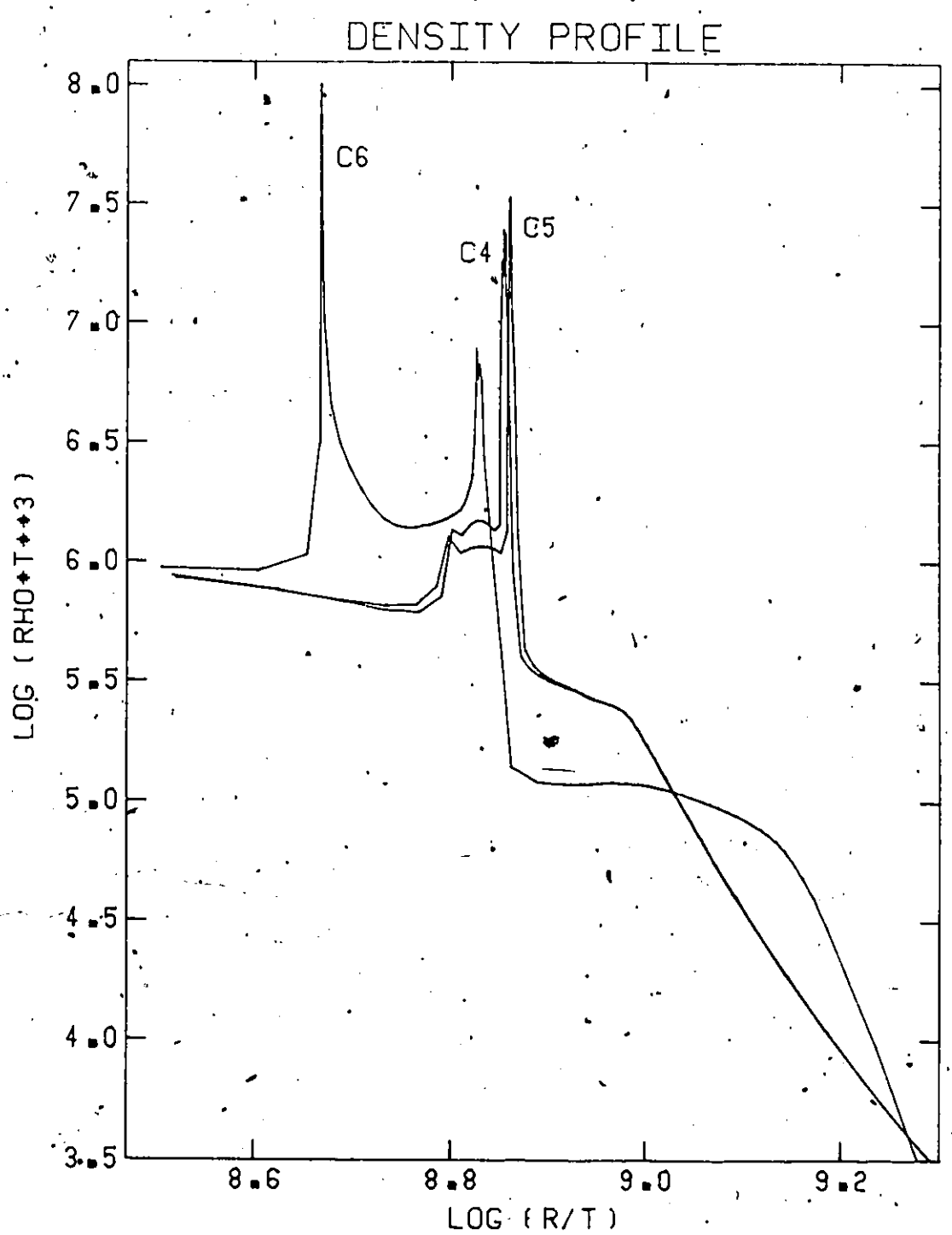
DENSITY PROFILE
C6
C5
C4
8.0
7.5
7.0
6.5
6.0
5.5
5.0
4.5
4.0
3.5
LOG (RHO*T**3)
8.6
8.8
9.0
9.2
LOG (R/T)

Figure 5-10

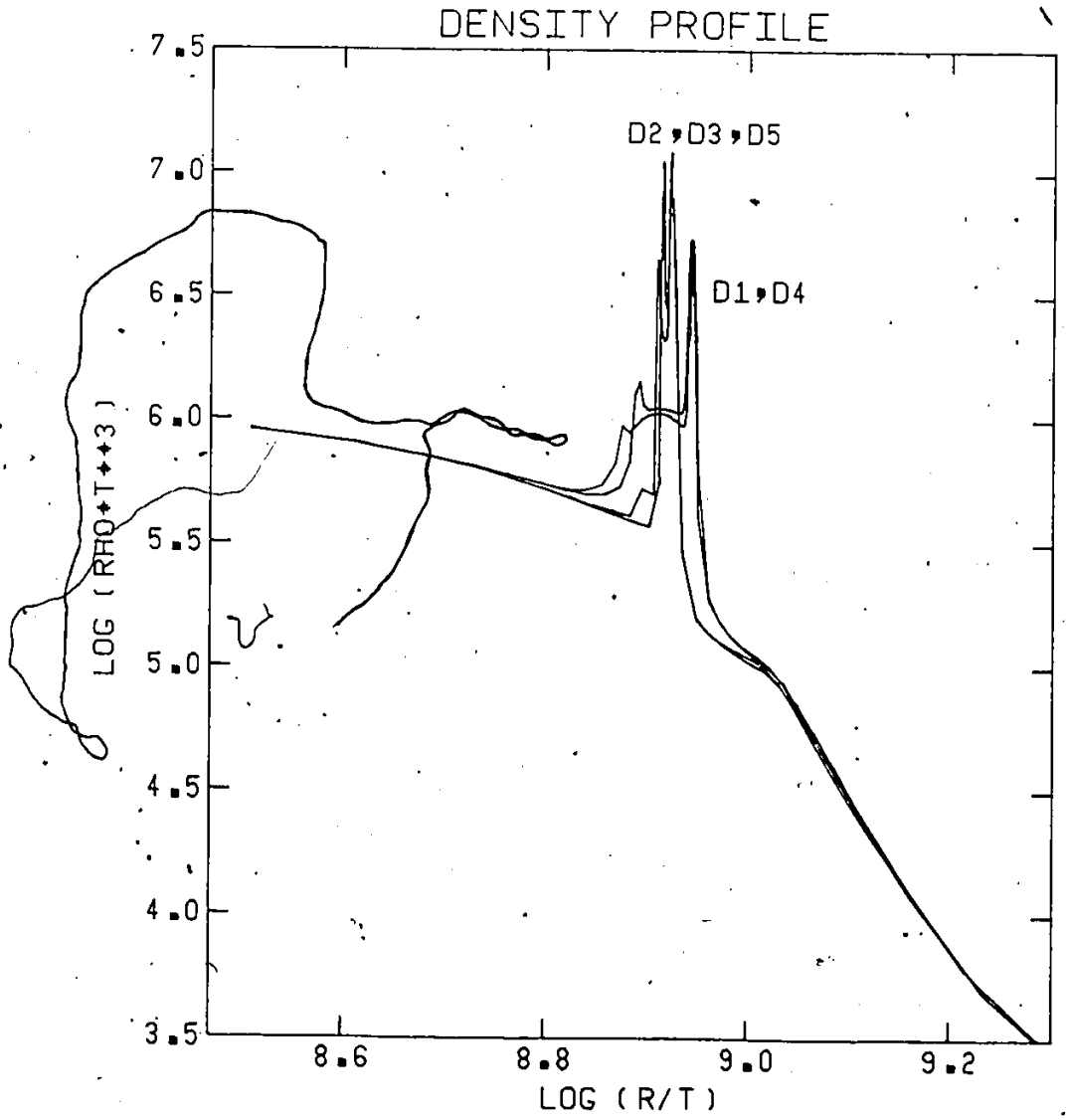
DENSITY PROFILE
D2,D3,D5
D1,D4
LOG (RHO*T**3)
LOG (R/T)
7.5
7.0
6.5
6.0
5.5
5.0
4.5
4.0
3.5
8.6
8.8
9.0
9.2

Figures 5-11 to 5-15

Velocity profiles plotted versus mass fraction. Figure 5-11 shows the time evolution of the velocity profile for model D5, with curves 3, 4, 5, 6 and 7 representing times of 10^3, 10^4, 10^5, 10^6, and $.5 \times 10^7$ seconds after ignition, respectively. The acceleration is negligible after 10^4 seconds. Figures 5-12 to 5-15 show the late-time velocity profiles for all the models.

Figure 5-11

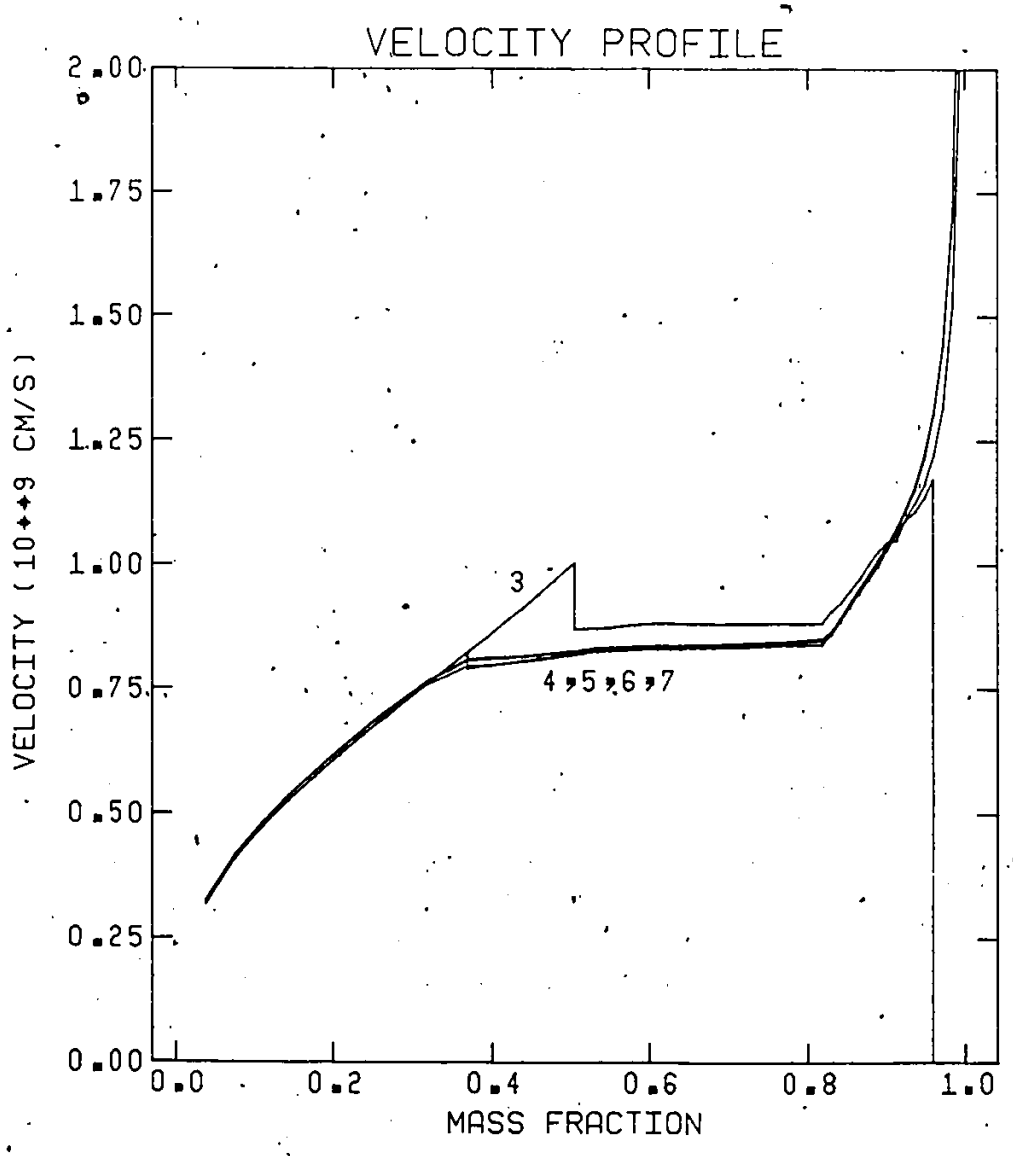
VELOCITY PROFILE
VELOCITY (10**9 CM/S)
2.00
1.75
1.50
1.25
1.00
0.75
0.50
0.25
0.00
0.0
0.2
0.4
0.6
0.8
1.0
MASS FRACTION
3
4,5,6,7

Figure 5-12

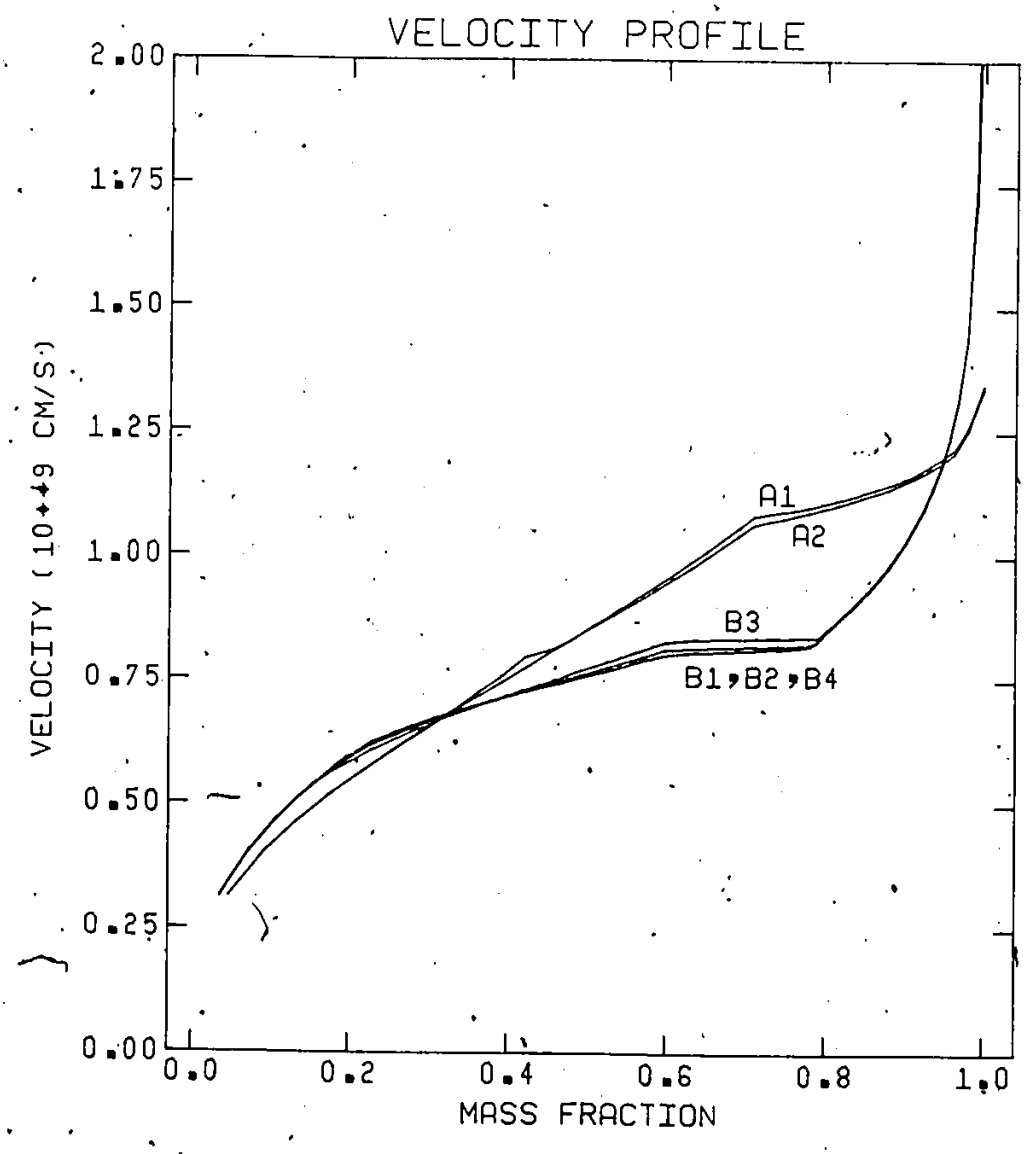
VELOCITY PROFILE
VELOCITY (10**9 CM/S)
2.00
1.75
1.50
1.25
1.00
0.75
0.50
0.25
0.00
0.0
0.2
0.4
0.6
0.8
1.0
MASS FRACTION
A1
A2
B3
B1,B2,B4

Figure 5-13

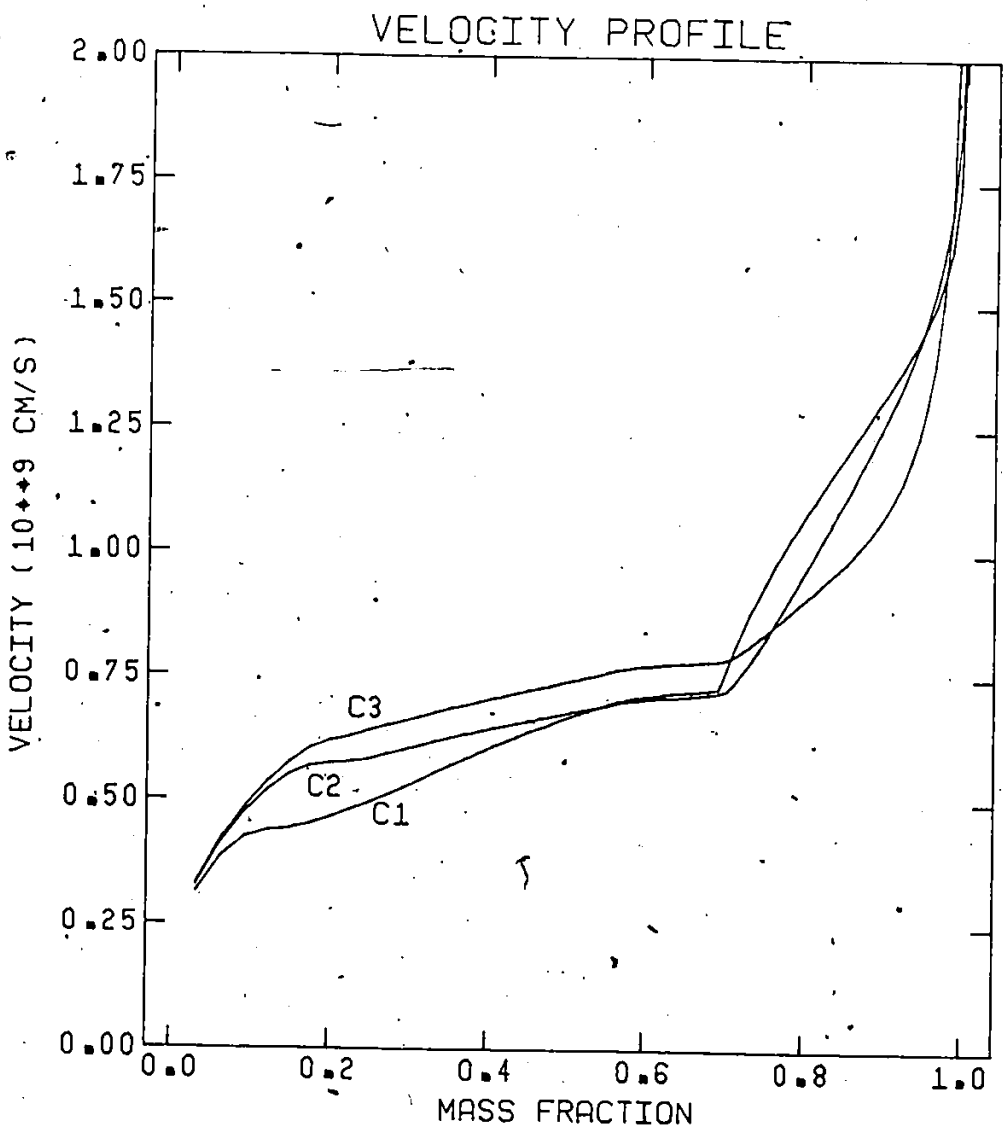
VELOCITY PROFILE
VELOCITY (10**9 CM/S)
2.00
1.75
1.50
1.25
1.00
0.75
0.50
0.25
0.00
0.0
0.2
0.4
0.6
0.8
1.0
MASS FRACTION
C3
C2
C1

Figure 5-14

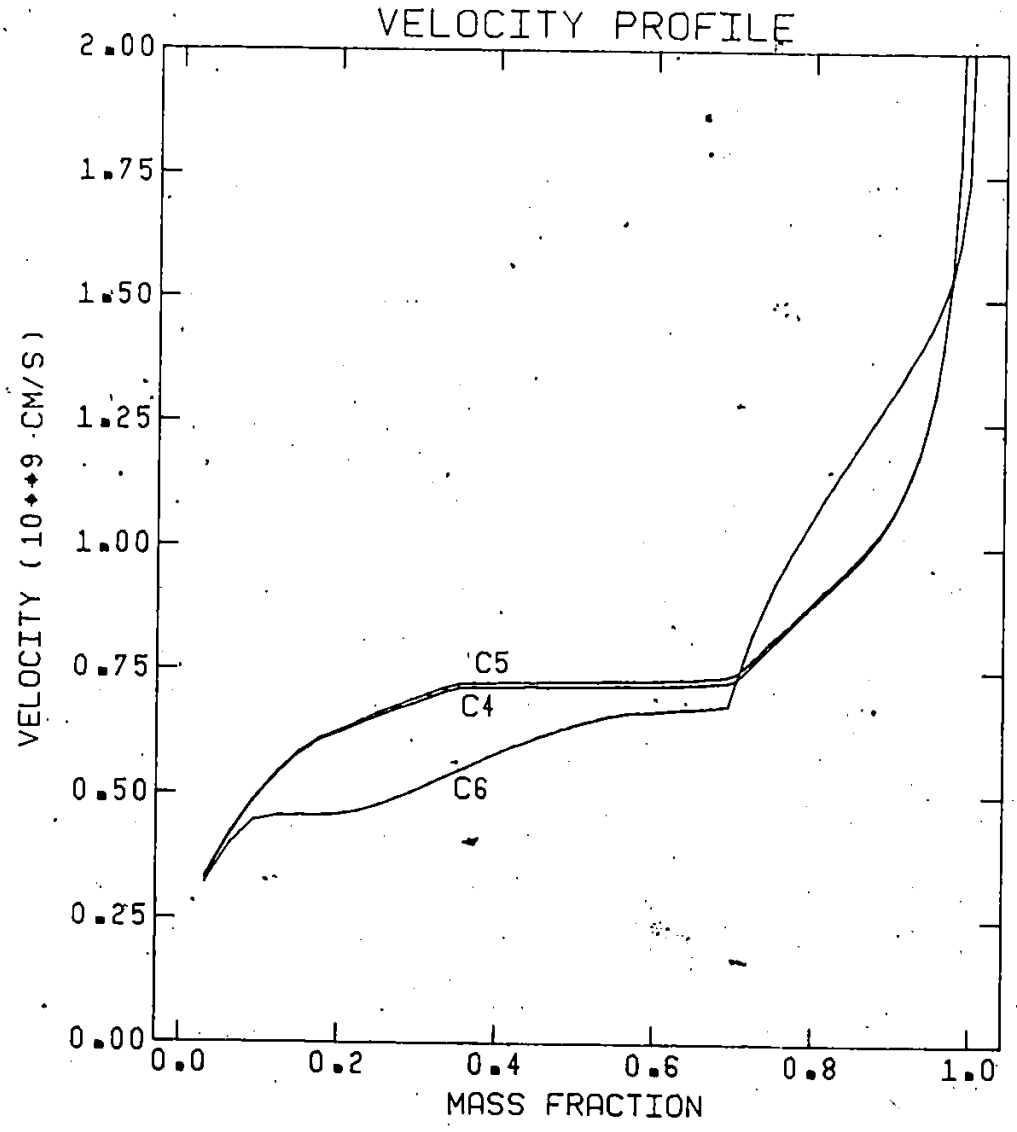
VELOCITY PROFILE
VELOCITY (10**9 CM/S)
2.00
1.75
1.50
1.25
1.00
0.75
0.50
0.25
0.00
0.0
0.2
0.4
0.6
0.8
1.0
MASS FRACTION
C5
C4
C6

Figure 5-15

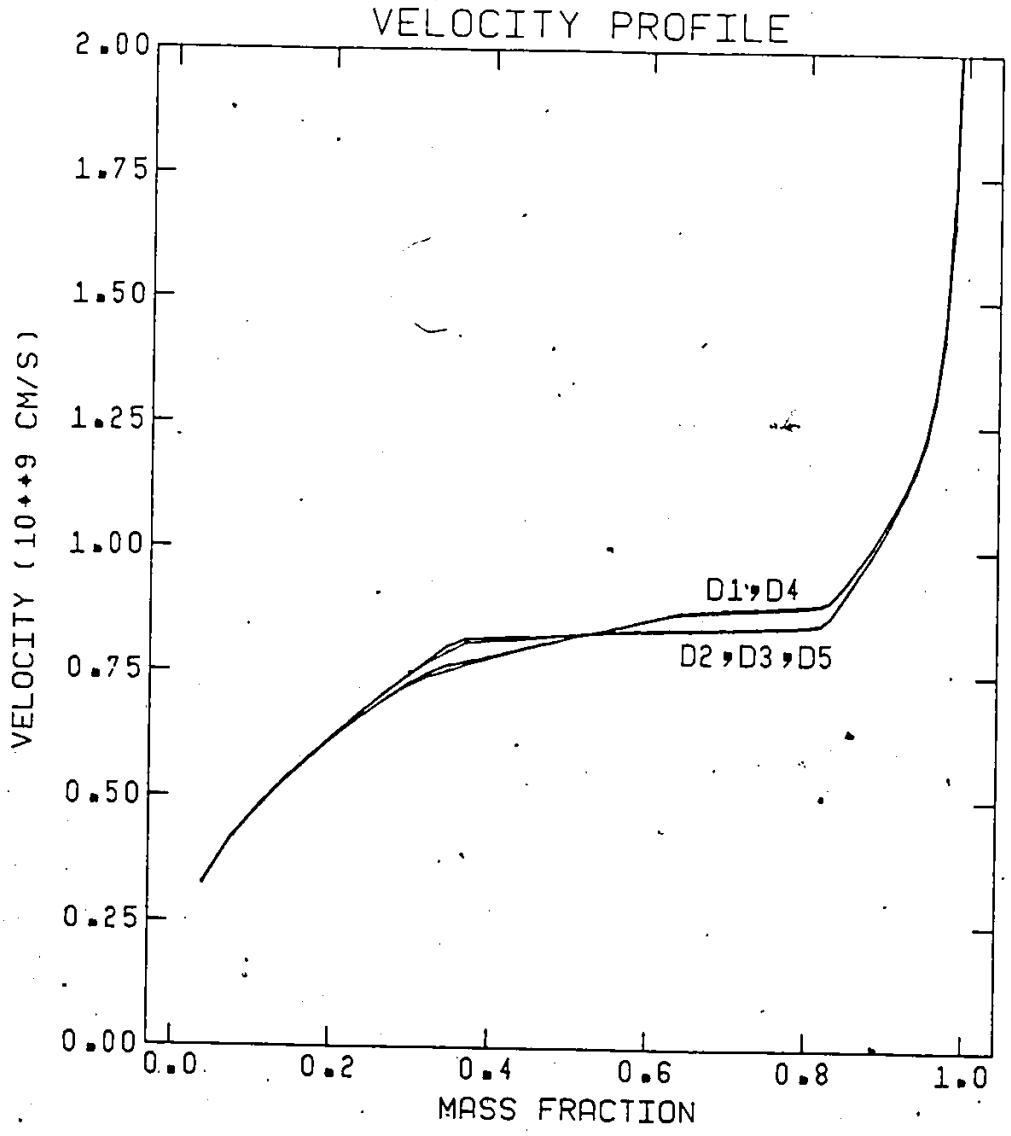
VELOCITY PROFILE
VELOCITY (10**9 CM/S)
2.00
1.75
1.50
1.25
1.00
0.75
0.50
0.25
0.00
0.0
0.2
0.4
0.6
0.8
1.0
MASS FRACTION
D1, D4
D2, D3, D5

Figure 5-16 to 5-18

Photospheric radius versus time, plotted for each model. The photospheric is defined to be located at optical depth $\tau = 2/3$. The radii are expressed in units of 10^{15} cm and the time in units of 10^{6} seconds.

Figure 5-16

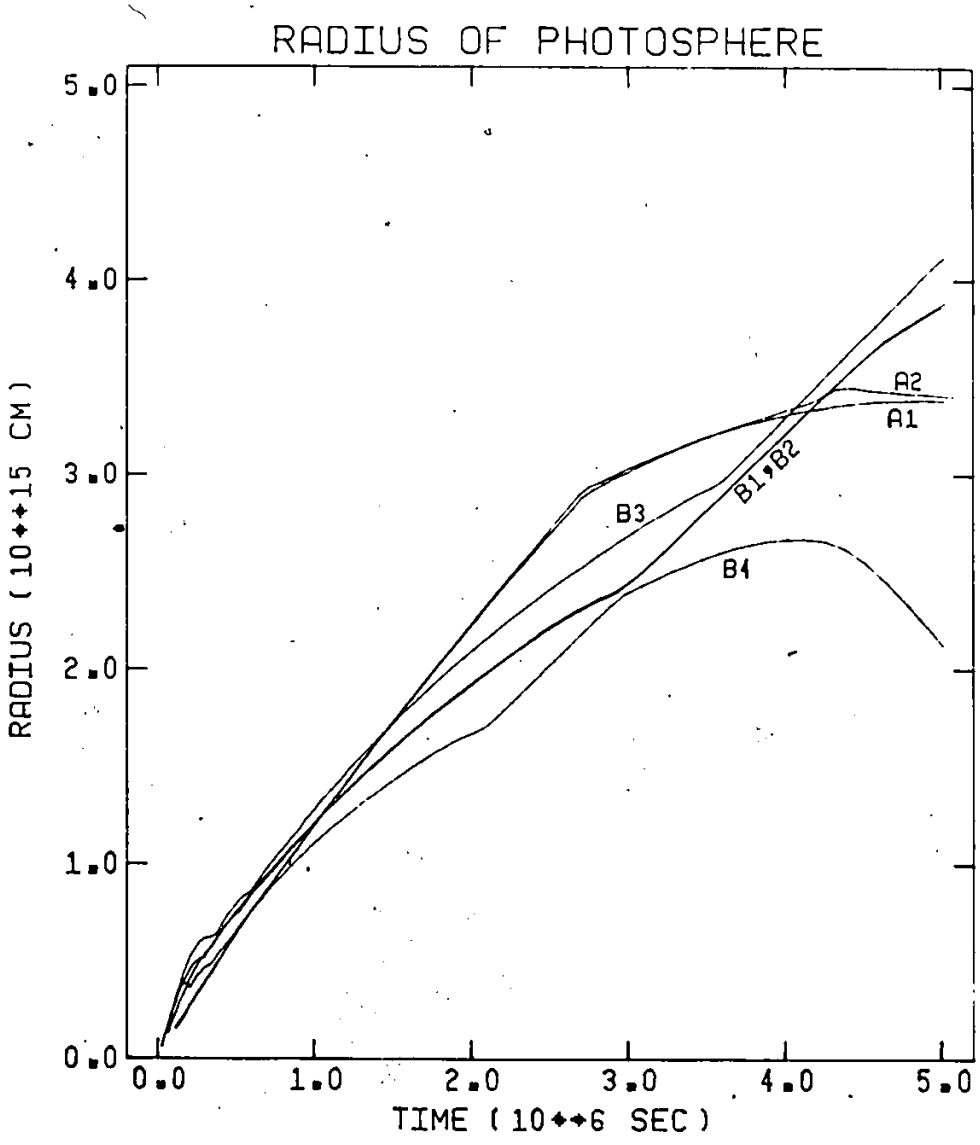
RADIUS OF PHOTOSPHERE
RADIUS (10**15 CM)
TIME (10**6 SEC)
5.0
4.0
3.0
2.0
1.0
0.0
0.0
1.0
2.0
3.0
4.0
5.0
A2
A1
B1,B2
B3
B4

Figure 5-17

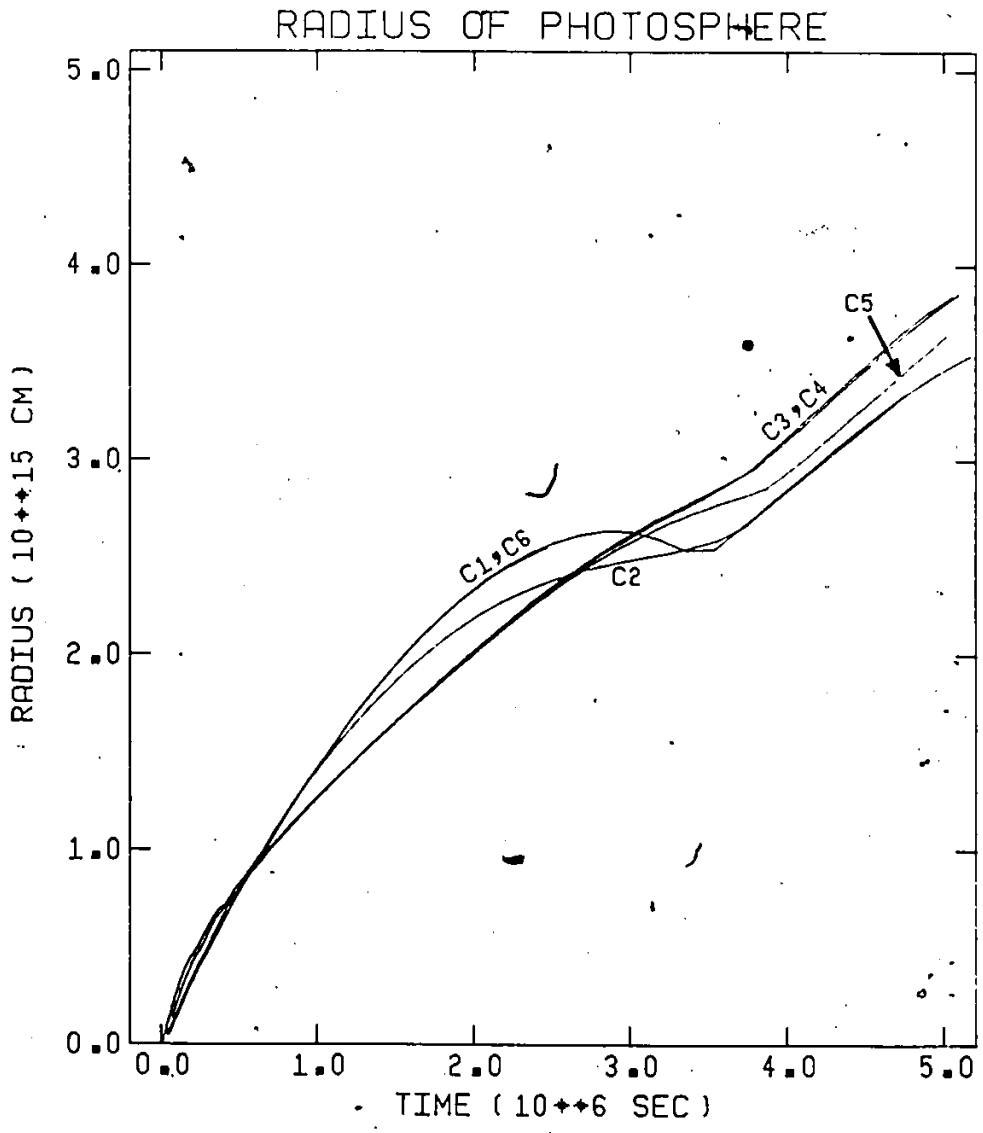
RADIUS OF PHOTOSPHERE
RADIUS (10**15 CM)
TIME (10**6 SEC)
0.0
1.0
2.0
3.0
4.0
5.0
C1,C6
C2
C3,C4
C5

Figure 5-18

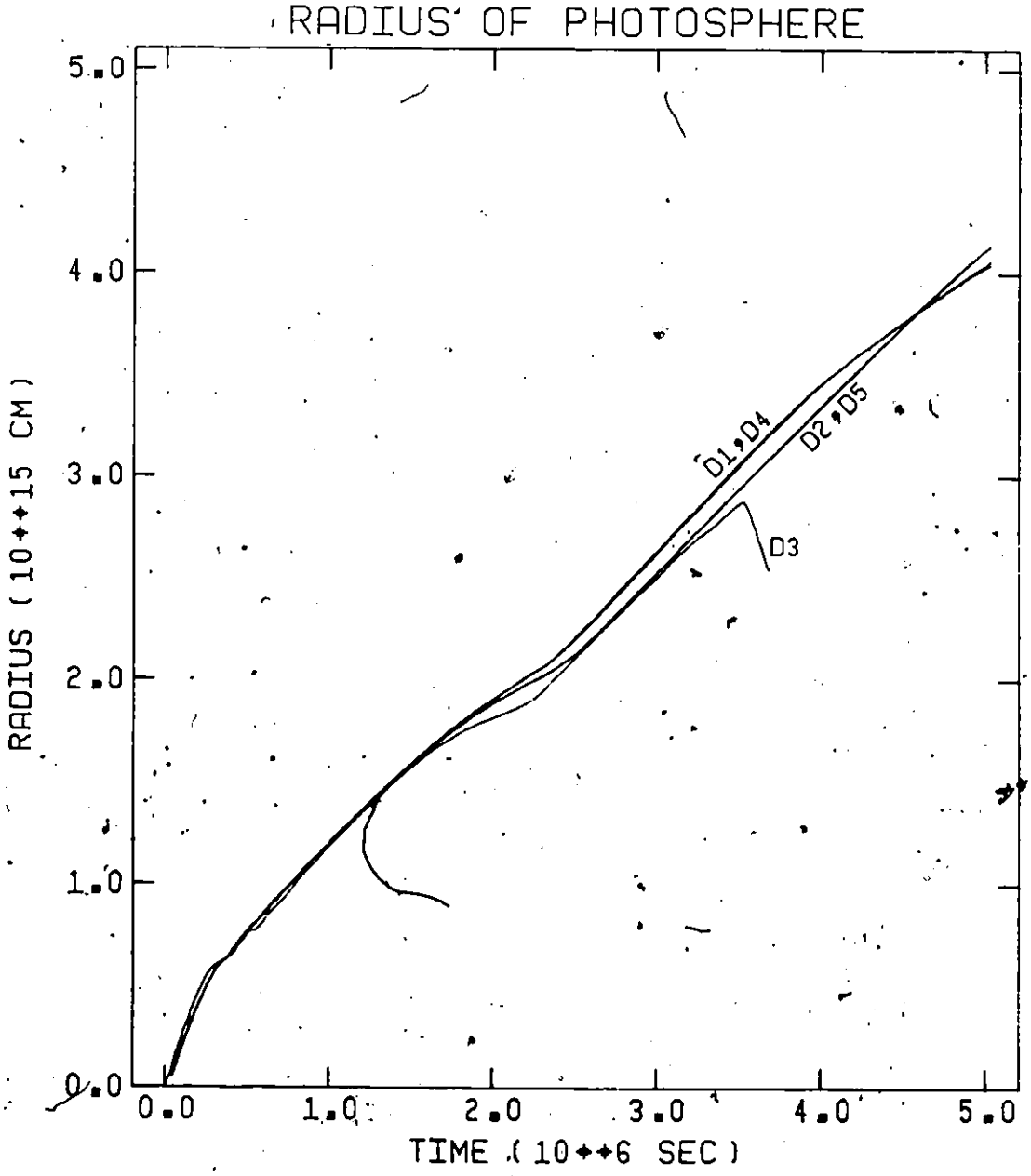
RADIUS OF PHOTOSPHERE
RADIUS (10**15 CM)
TIME (10**6 SEC)
5.0
4.0
3.0
2.0
1.0
0.0
0.0
1.0
2.0
3.0
4.0
5.0
D1,D4
D2,D5
D3

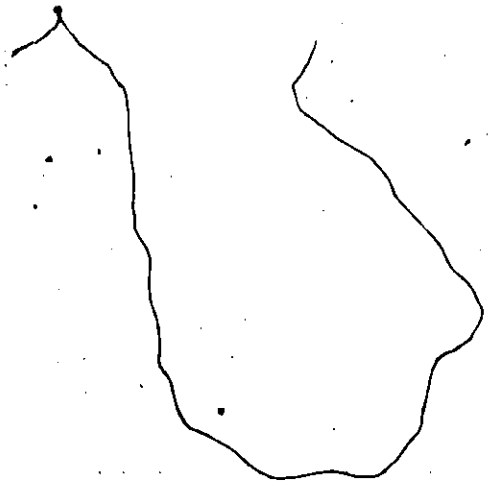

Figure 5-19 to 5-21

Velocity at the photosphere versus time, for each model. Note that this refers to the velocity of the matter at the location of the photosphere, rather than to the velocity of the photosphere itself. The two differ because the photosphere continually recedes in Lagrangian coordinates. The velocity is expressed in units of 10^9 cm-s^{-1}.

Figure 5-19

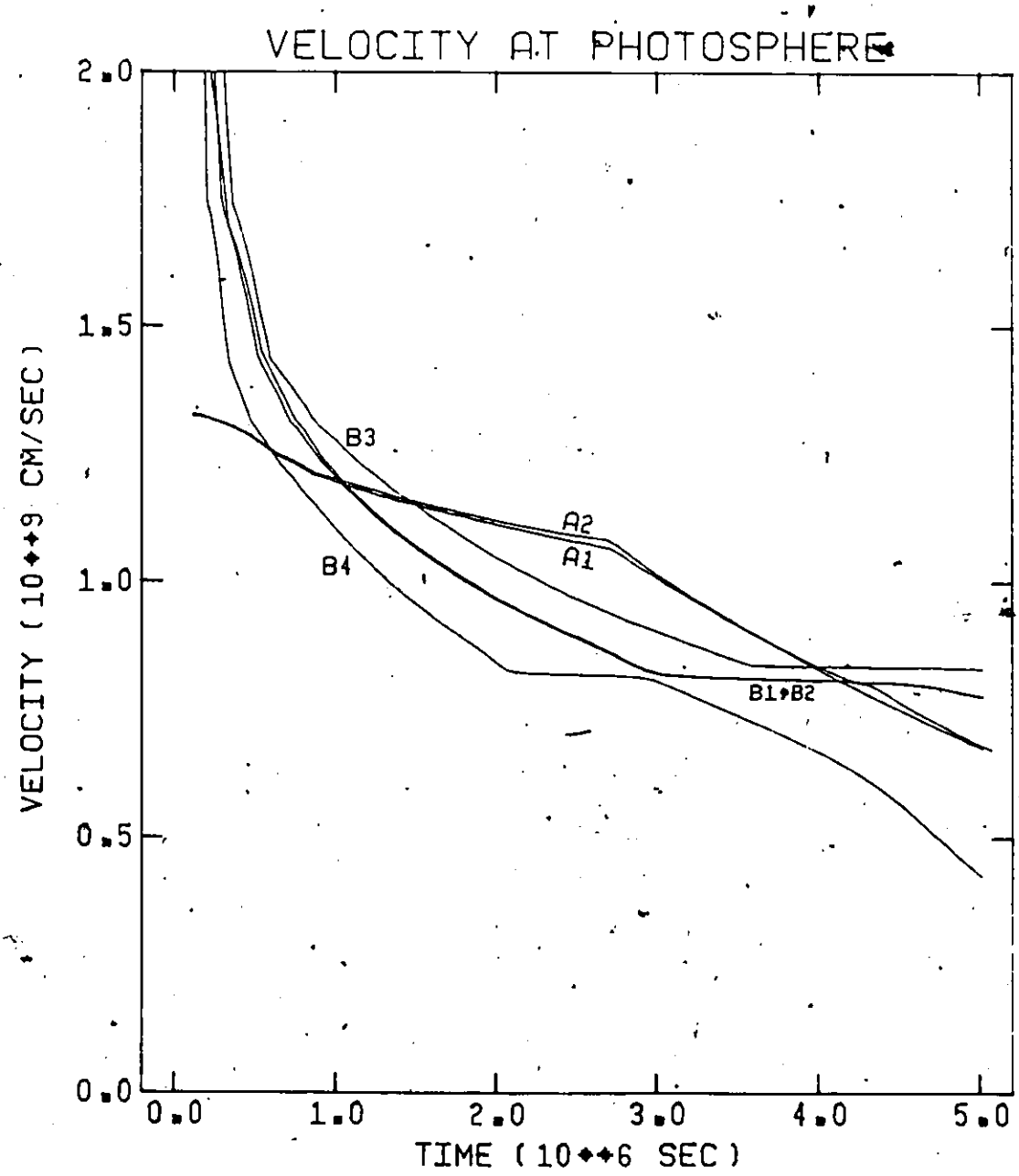
VELOCITY AT PHOTOSPHERE
VELOCITY (10**9 CM/SEC)
TIME (10**6 SEC)
2.0
1.5
1.0
0.5
0.0
0.0
1.0
2.0
3.0
4.0
5.0
B3
A2
A1
B4
B1+B2

Figure 5-20

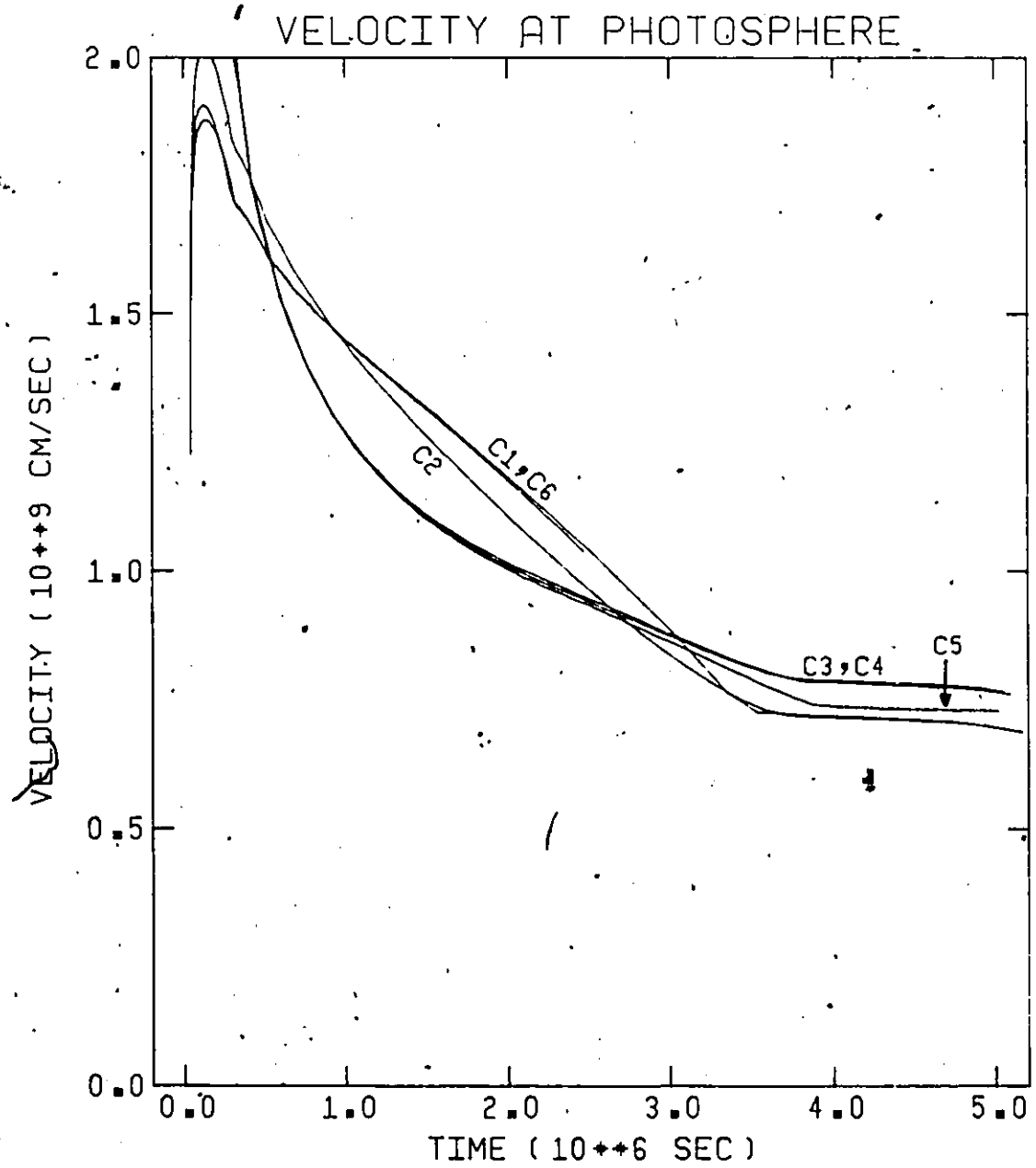
VELOCITY AT PHOTOSPHERE
2.0
1.5
1.0
0.5
0.0
VELOCITY (10**9 CM/SEC)
C1,C6
C2
C3,C4
C5
0.0
1.0
2.0
3.0
4.0
5.0
TIME (10**6 SEC)

Figure 5-21

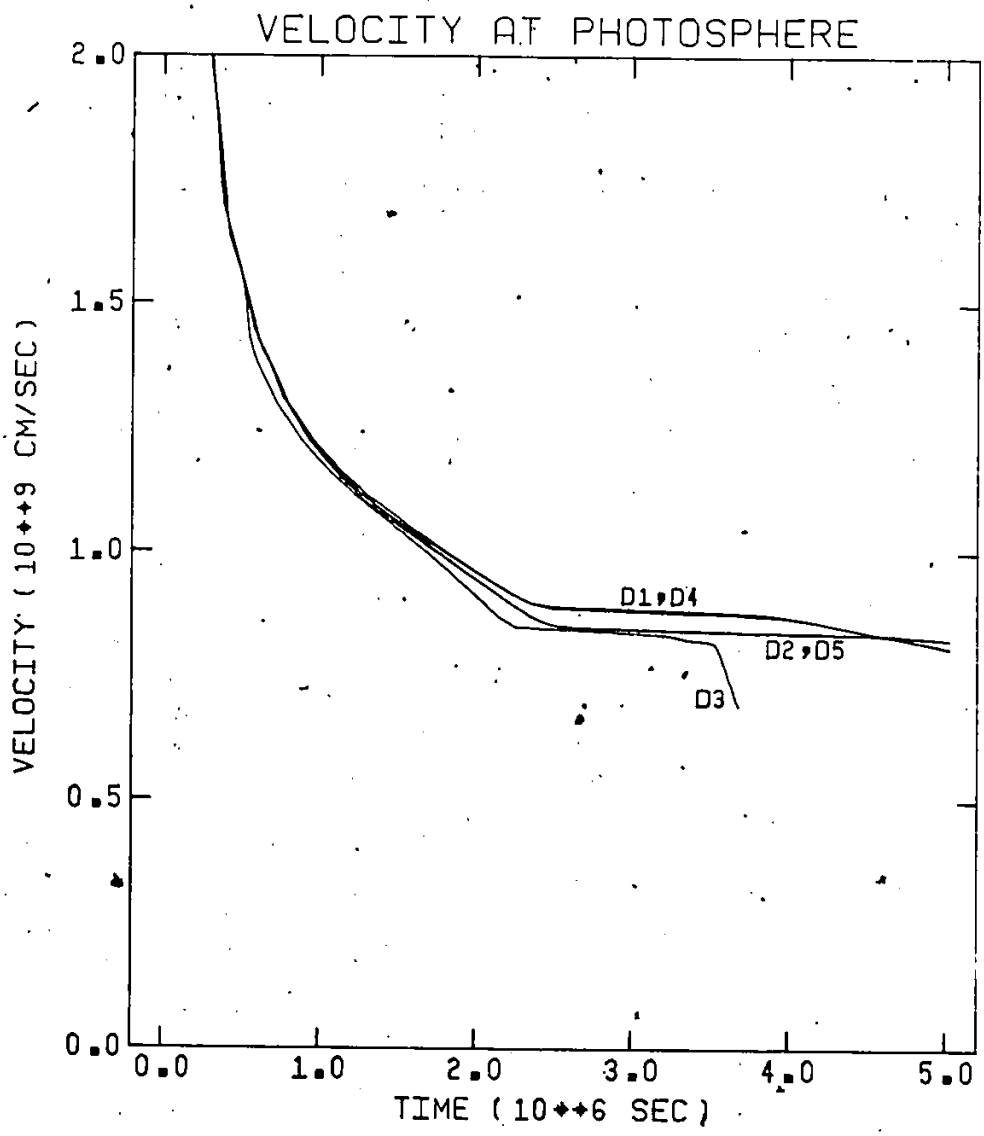
VELOCITY AT PHOTOSPHERE
VELOCITY (10**9 CM/SEC)
TIME (10**6 SEC)
2.0
1.5
1.0
0.5
0.0
0.0
1.0
2.0
3.0
4.0
5.0
D1,D4
D2,D5
D3

Figure 5-22 to 5-24

Luminosity versus time, for each model. The luminosity is the thermal photon flux out of the surface zone, i.e. gamma rays from radioactive processes are excluded. The luminosity curves for the bare white dwarf models (A1 and A2) differ qualitatively from the envelope models by the absence of the sharp, narrow precursor peak seen in the latter. The luminosities are measured in units of 10^{43} erg-s^{-1}.

Figure 5-22

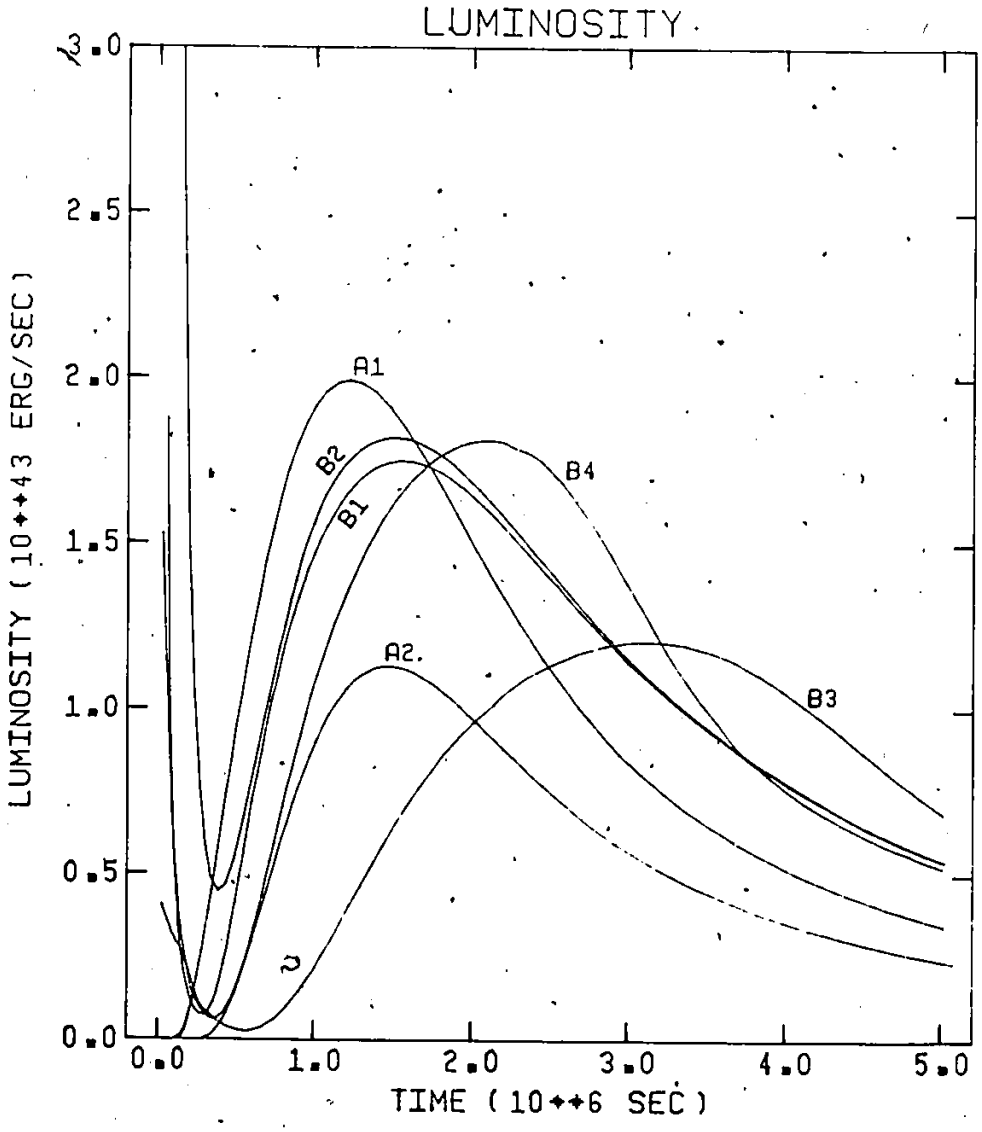
LUMINOSITY
LUMINOSITY (10**43 ERG/SEC)
TIME (10**6 SEC)
3.0
2.5
2.0
1.5
1.0
0.5
0.0
0.0
1.0
2.0
3.0
4.0
5.0
A1
B2
B1
B4
A2.
B3
U

Figure 5-23

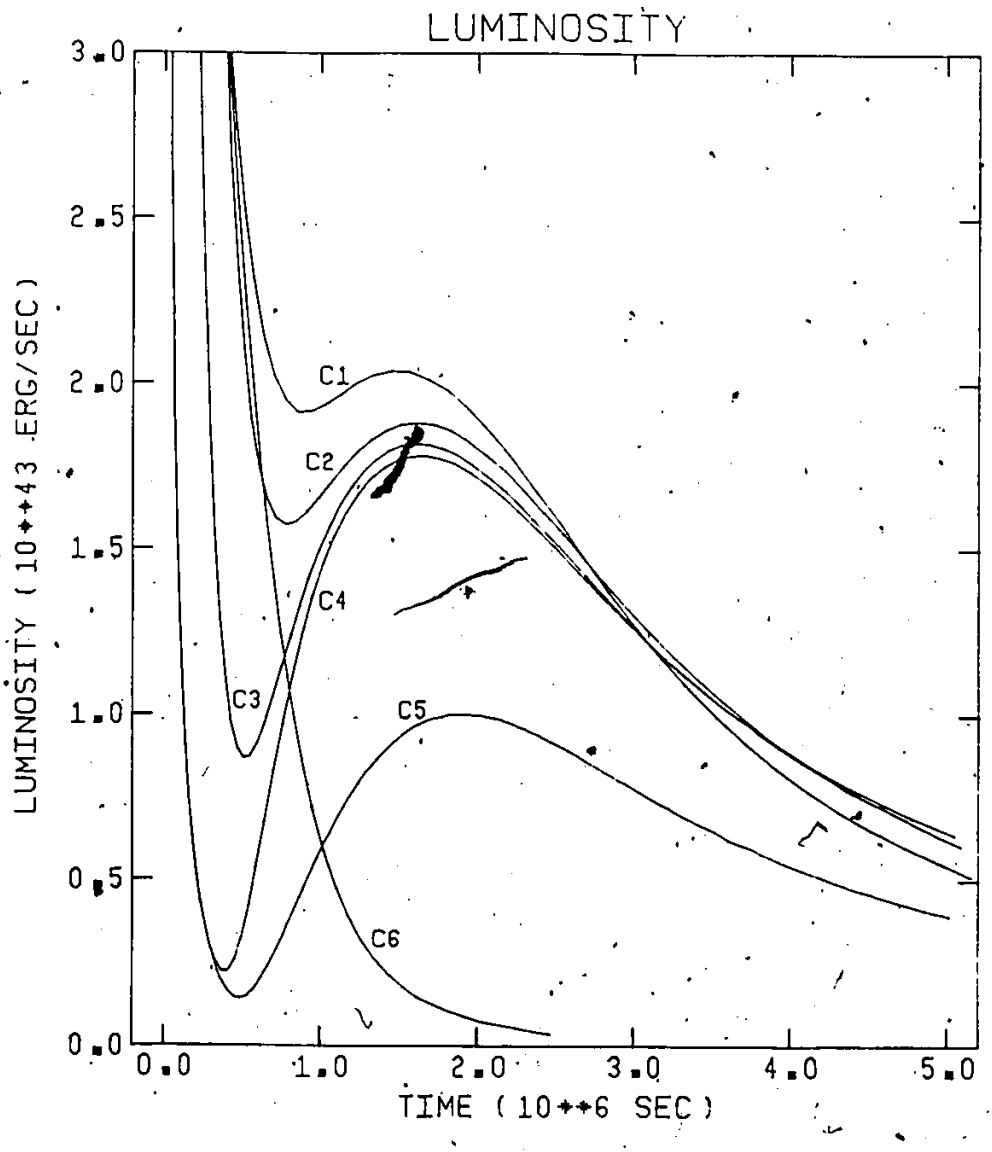
LUMINOSITY
LUMINOSITY (10**43 ERG/SEC)
TIME (10**6 SEC)
C1
C2
C3
C4
C5
C6
3.0
2.5
2.0
1.5
1.0
0.5
0.0
0.0
1.0
2.0
3.0
4.0
5.0

Figure 5-24

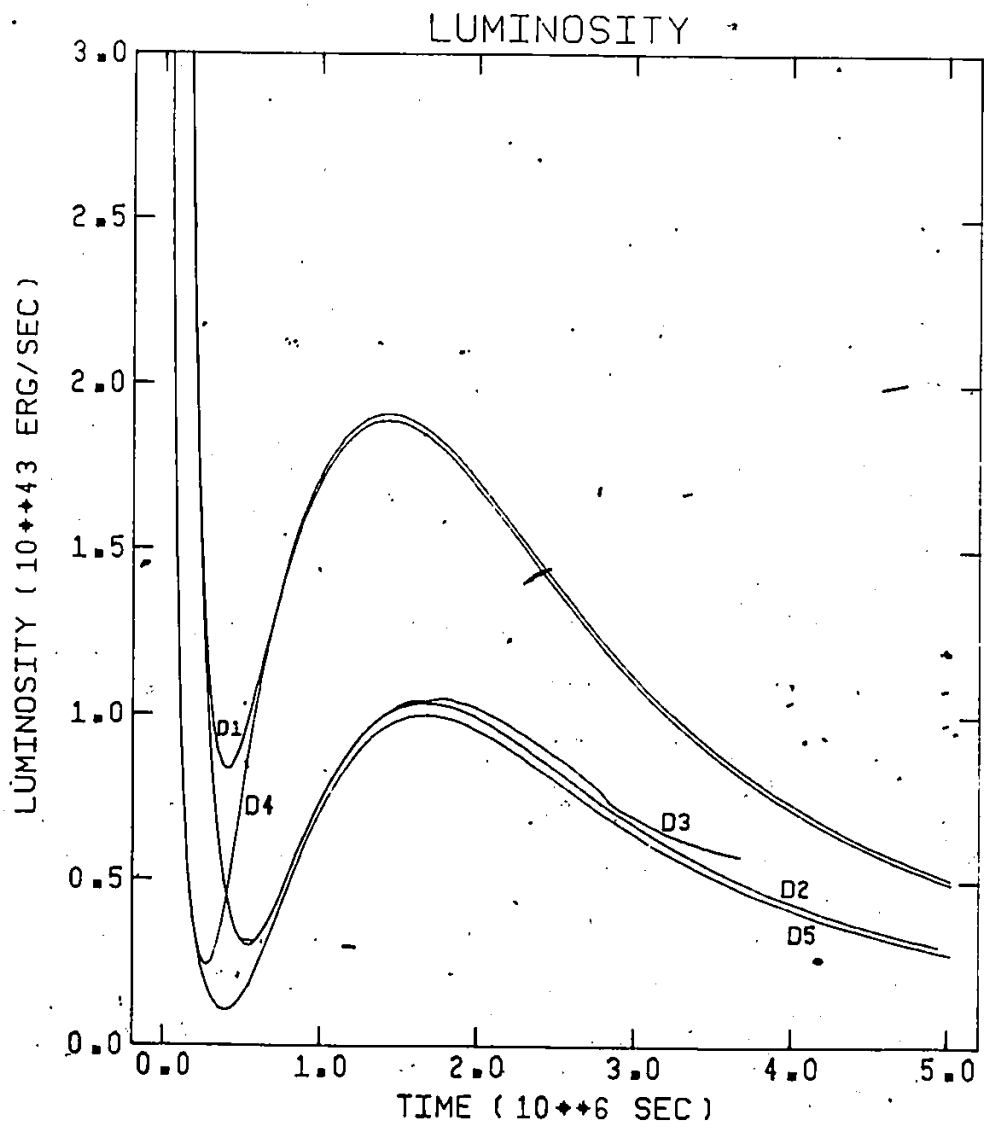
LUMINOSITY
LUMINOSITY (10**43 ERG/SEC)
TIME (10**6 SEC)
3.0
2.5
2.0
1.5
1.0
0.5
0.0
0.0
1.0
2.0
3.0
4.0
5.0
D1
D4
D3
D2
D5

Figure 5-25 to 5-30

Colour temperatures versus time, for each model. Two methods of determining the colour temperature are used. The first method (labelled I) assumes that the luminosity is distributed across a full blackbody spectrum. The colour temperatures determined by method I are plotted in Figures 5-25 to 5-27. The second method (labelled II) assumes that there is negligible flux shortwards of 4000 Å and blackbodyemission at longer wavelengths. The colour temperatures following from this 'truncated spectrum' are plotted in Figures 5-28 to 5-30. The temperatures are in units of 10^4 K.

Figure 5-25

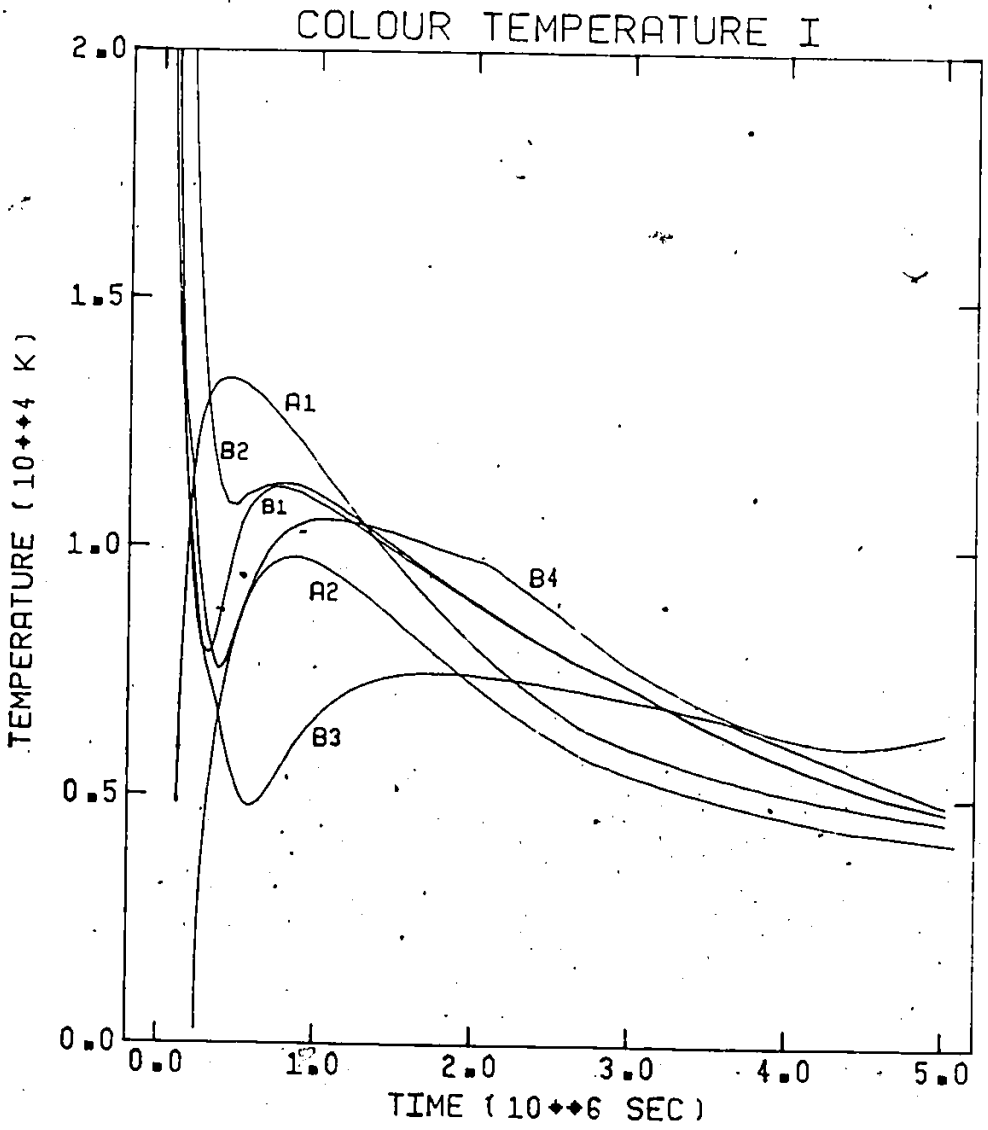
COLOUR TEMPERATURE I
TEMPERATURE (10**4 K)
TIME (10**6 SEC)
2.0
1.5
1.0
0.5
0.0
0.0
1.0
2.0
3.0
4.0
5.0
A1
B2
B1
A2
B4
B3

Figure 5-26

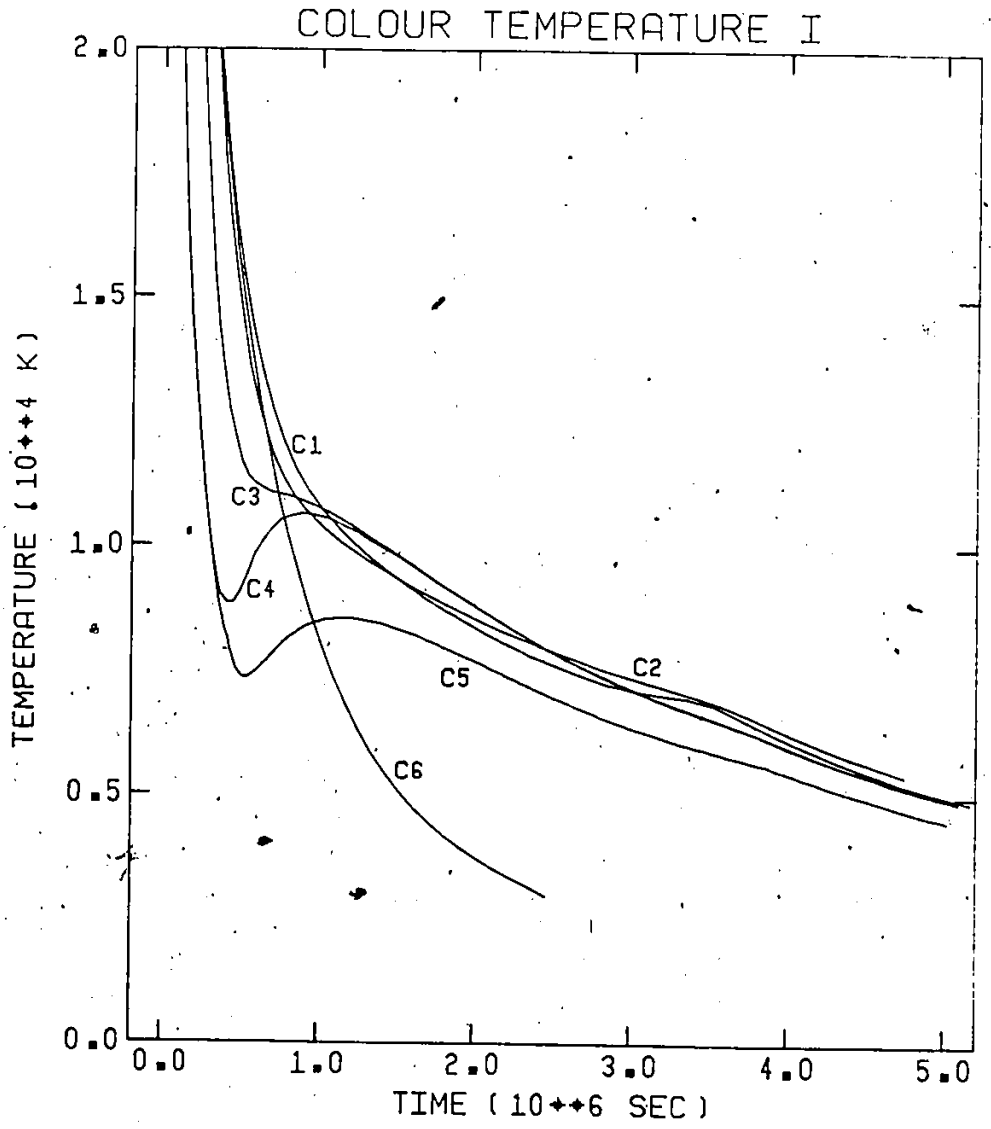
COLOUR TEMPERATURE I
TEMPERATURE (10**4 K)
TIME (10**6 SEC)
2.0
1.5
1.0
0.5
0.0
0.0
1.0
2.0
3.0
4.0
5.0
C1
C2
C3
C4
C5
C6

Figure 5-27

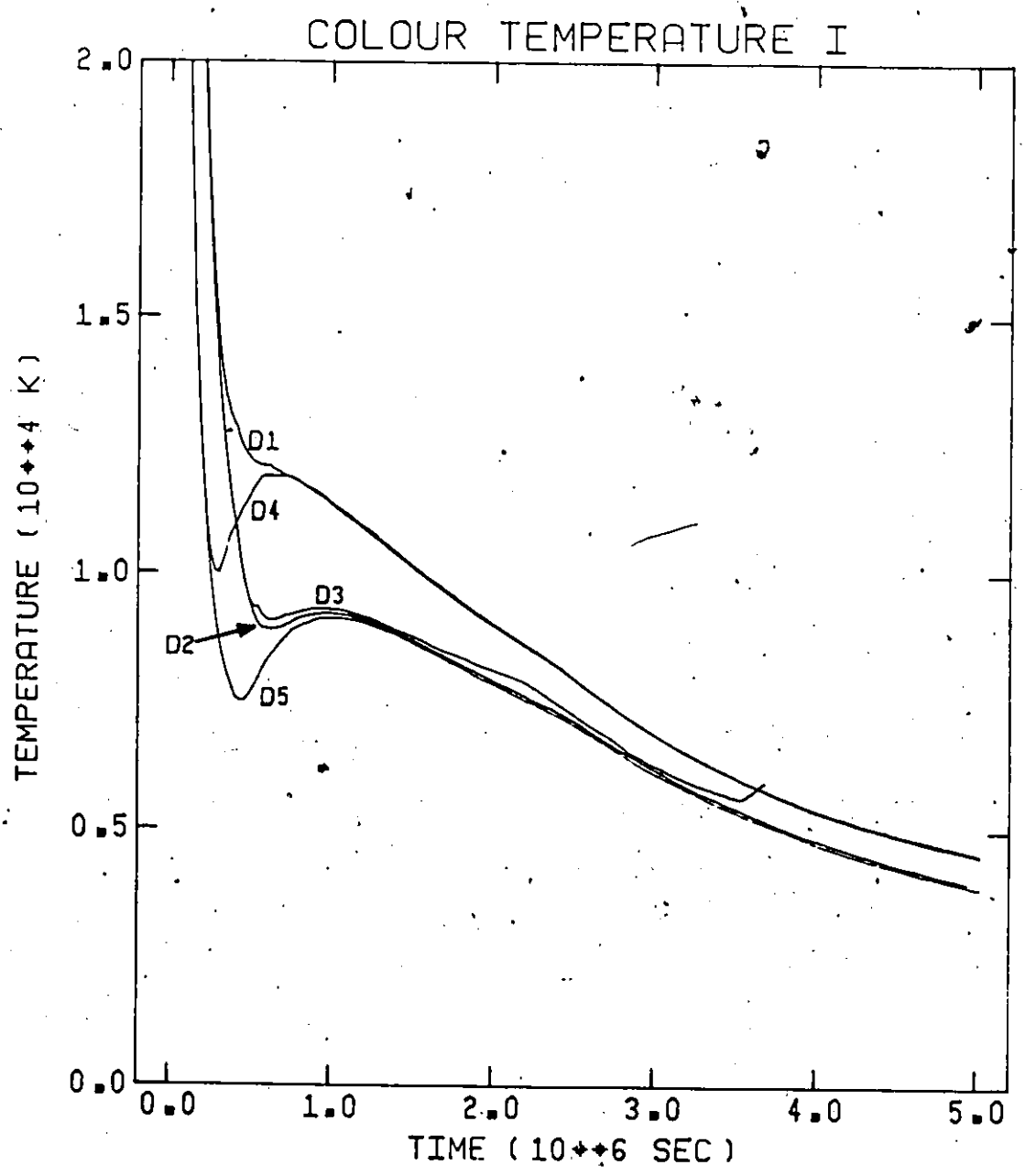
COLOUR TEMPERATURE I
TEMPERATURE (10**4 K)
TIME (10**6 SEC)
2.0
1.5
1.0
0.5
0.0
0.0
1.0
2.0
3.0
4.0
5.0
D1
D2
D3
D4
D5

Figure 5-28

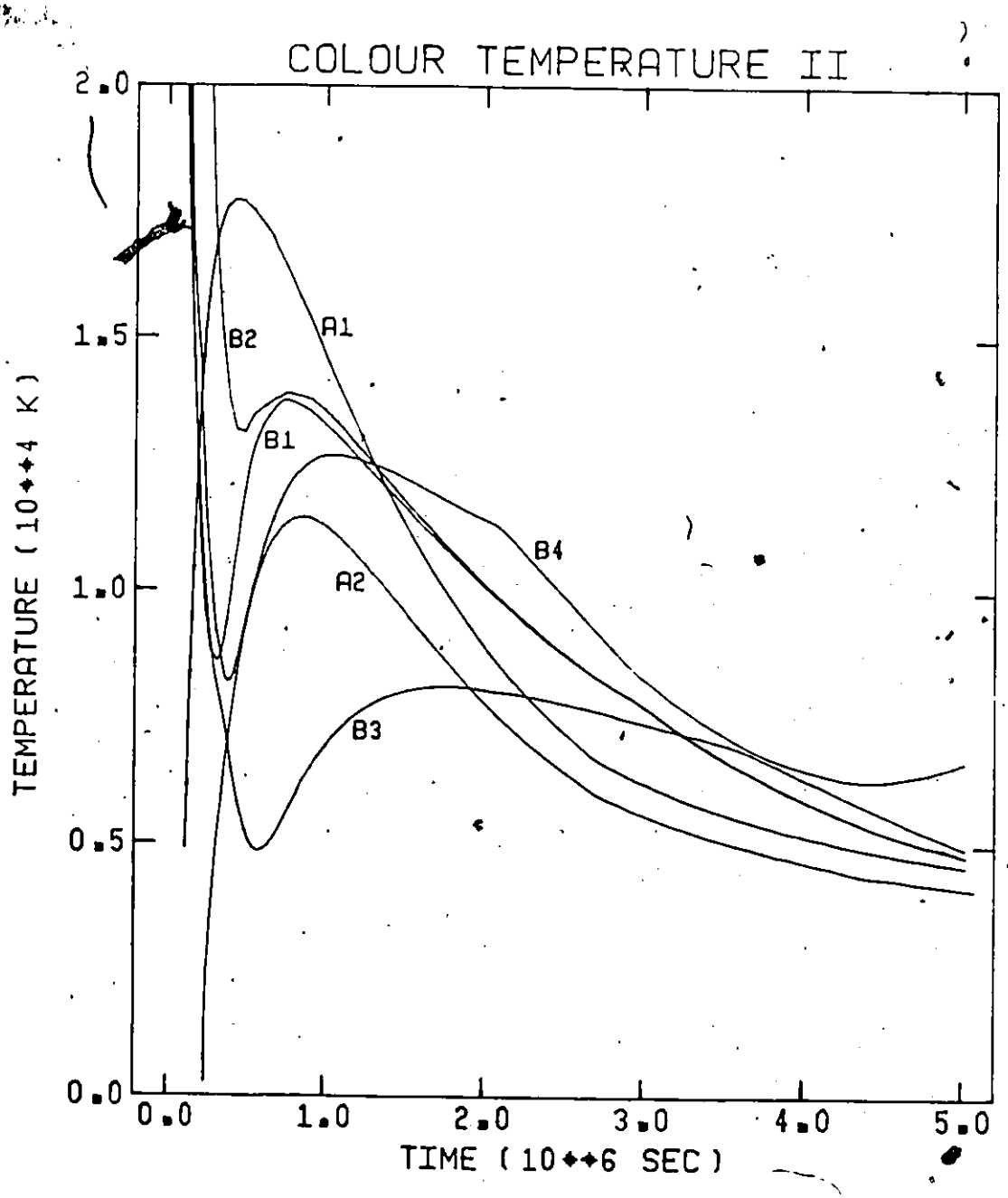
COLOUR TEMPERATURE II
TEMPERATURE (10**4 K)
TIME (10**6 SEC)
2.0
1.5
1.0
0.5
0.0
0.0
1.0
2.0
3.0
4.0
5.0
B2
A1
B1
B4
A2
B3

Figure 5-29

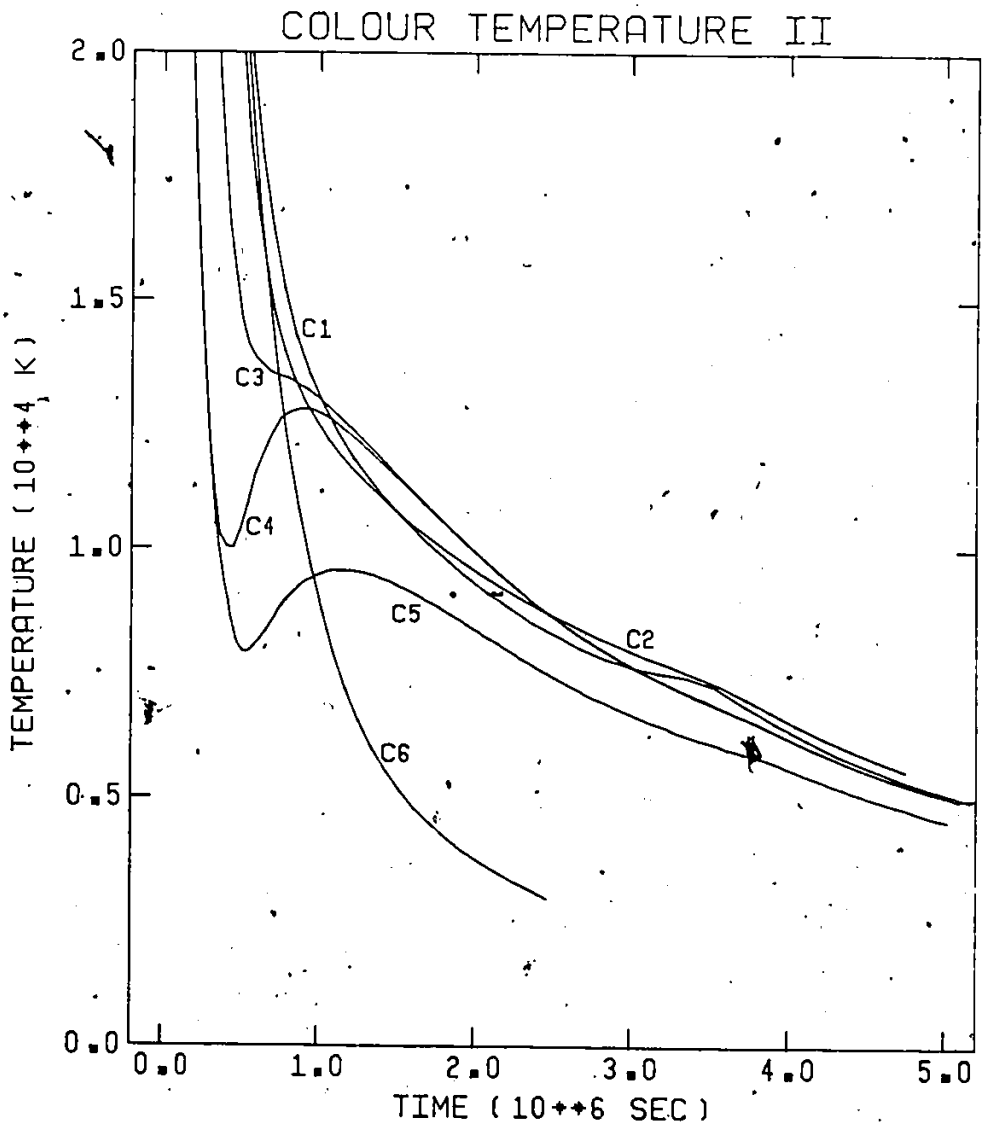
COLOUR TEMPERATURE II
TEMPERATURE (10++4 K)
TIME (10++6 SEC)
2.0
1.5
1.0
0.5
0.0
0.0
1.0
2.0
3.0
4.0
5.0
C1
C2
C3
C4
C5
C6

Figure 5-30

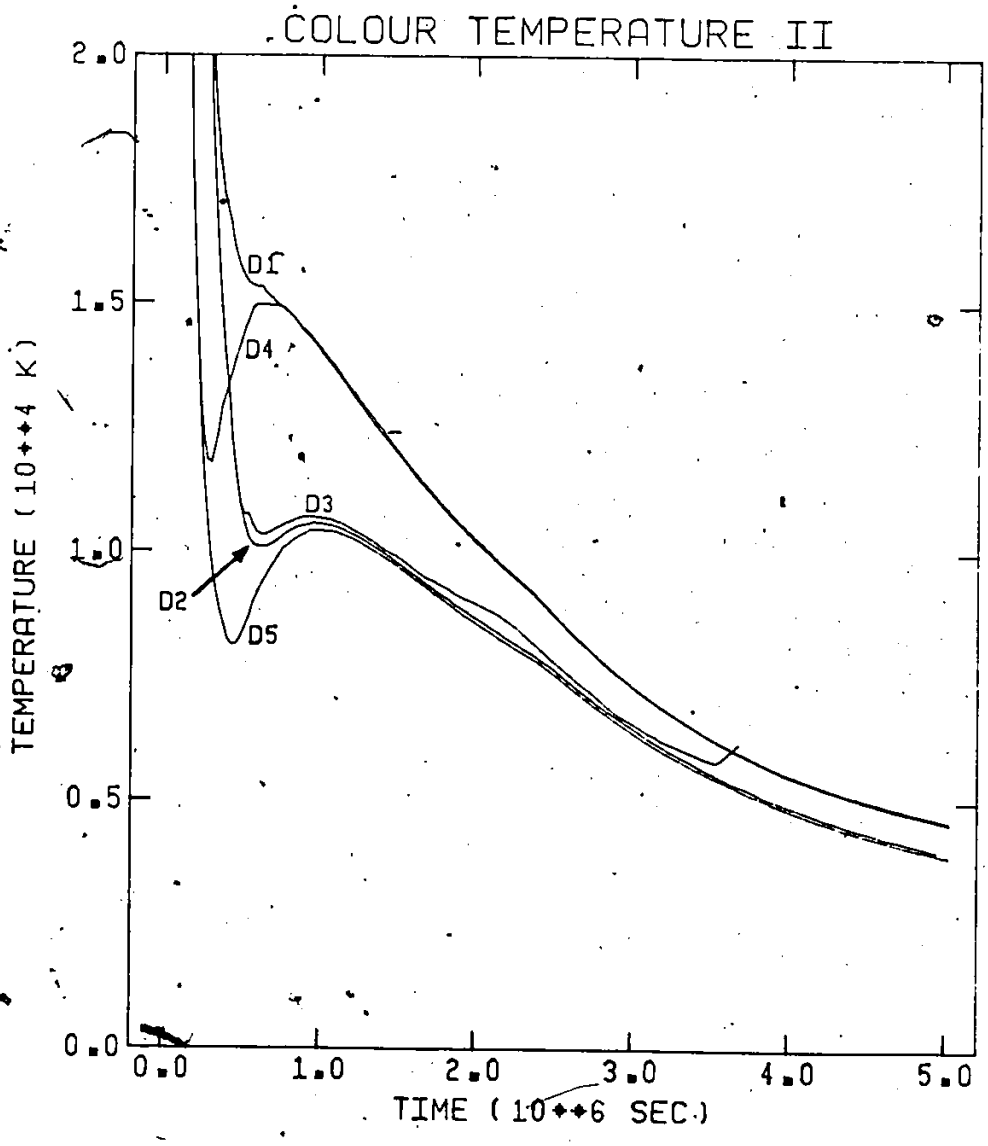
COLOUR TEMPERATURE II
TEMPERATURE (10**4 K)
TIME (10**6 SEC.)
2.0
1.5
1.0
0.5
0.0
0.0
1.0
2.0
3.0
4.0
5.0
D1
D4
D3
D2
D5

Figures 5-31 to 5-33

Bolometric light curves versus time, for each model. As is the case with the luminosity curves (Figures 5-22 to 5-24), the bare white dwarf models are single-peaked, while the envelope models are double-peaked. For most envelope models the first peak (around 10^5 seconds after ignition) is brighter than the subsequent peak ($\sim$ 15 days later), although most of the flux from the first peak would be in the form of X-rays.

Figure 5-31

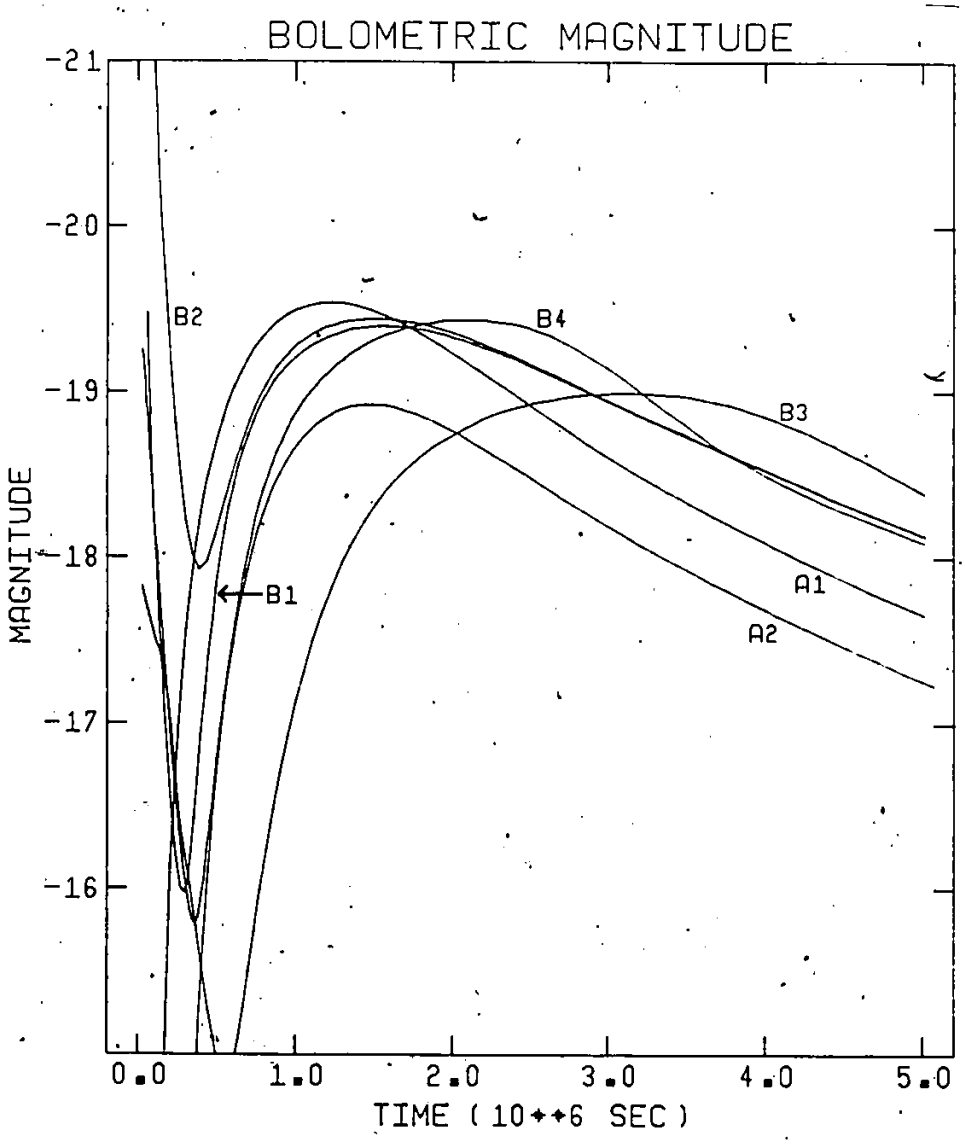
BOLOMETRIC MAGNITUDE
MAGNITUDE
-21
-20
-19
-18
-17
-16
B2
B4
B3
B1
A1
A2
0.0
1.0
2.0
3.0
4.0
5.0
TIME (10**6 SEC)

Figure 5-32

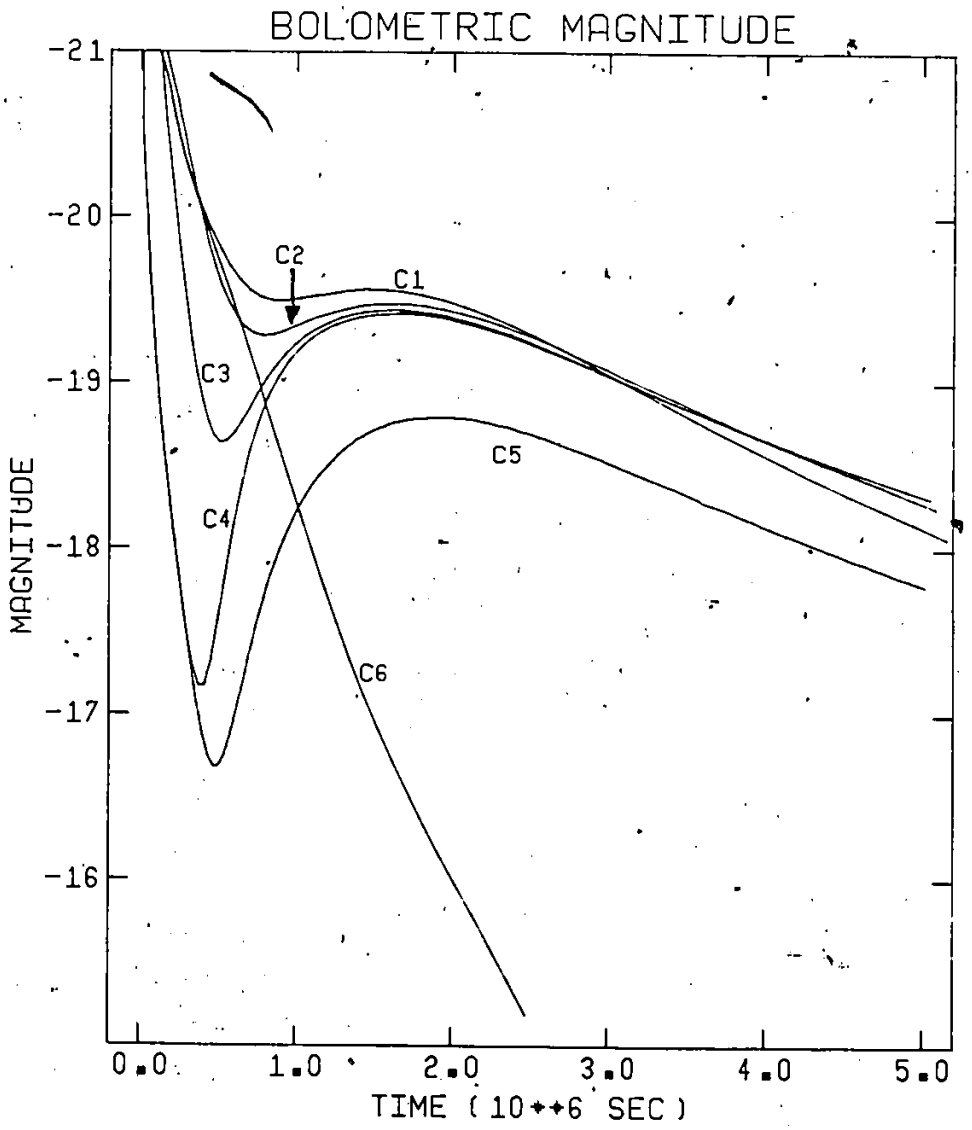
BOLOMETRIC MAGNITUDE
MAGNITUDE
-21
-20
-19
-18
-17
-16
C1
C2
C3
C4
C5
C6
0.0
1.0
2.0
3.0
4.0
5.0
TIME (10**6 SEC)

Figure 5-33

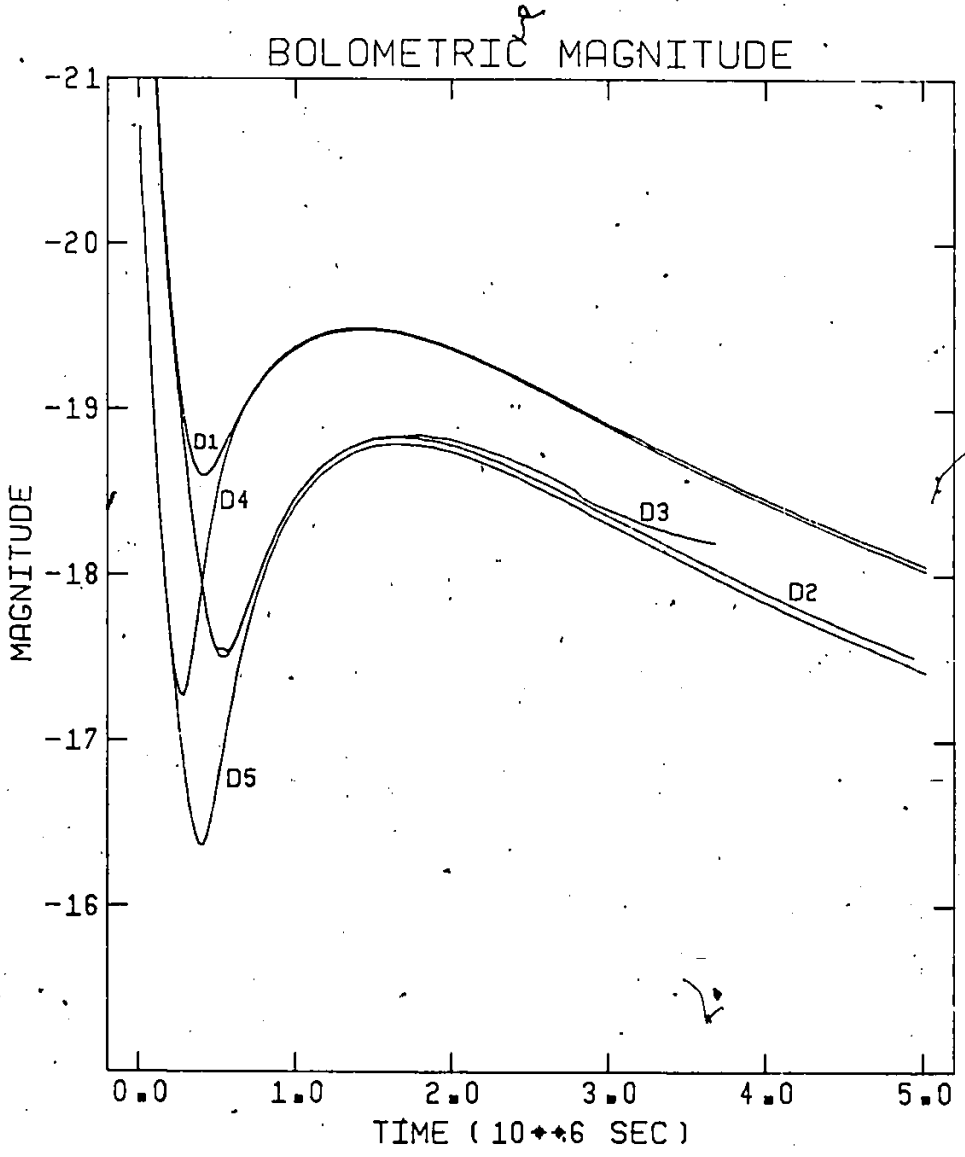
BOLOMETRIC MAGNITUDE
-21
-20
-19
-18
-17
-16
MAGNITUDE
D1
D4
D3
D2
D5
0.0
1.0
2.0
3.0
4.0
5.0
TIME (10**6 SEC)

Figure 5-34 to 5-39

Blue band light curves versus time for each model. As the blue magnitude depends on the colour temperature, two sets of curves are given. Figures 5-34 to 5-36 use the 'untruncated' colour temperatures of Figures 5-25 to 5-27, while Figures 5-37 to 5-39 use the 'truncated' colour temperatures of Figures 5-28 to 5-30. The data points are for SN 1981b, taken from Buta and Turner (1983), assuming supernova ignition at J.D. 2444656.5 and a distance modulus to the host galaxy of 31.5 magnitudes.

Figure 5-34

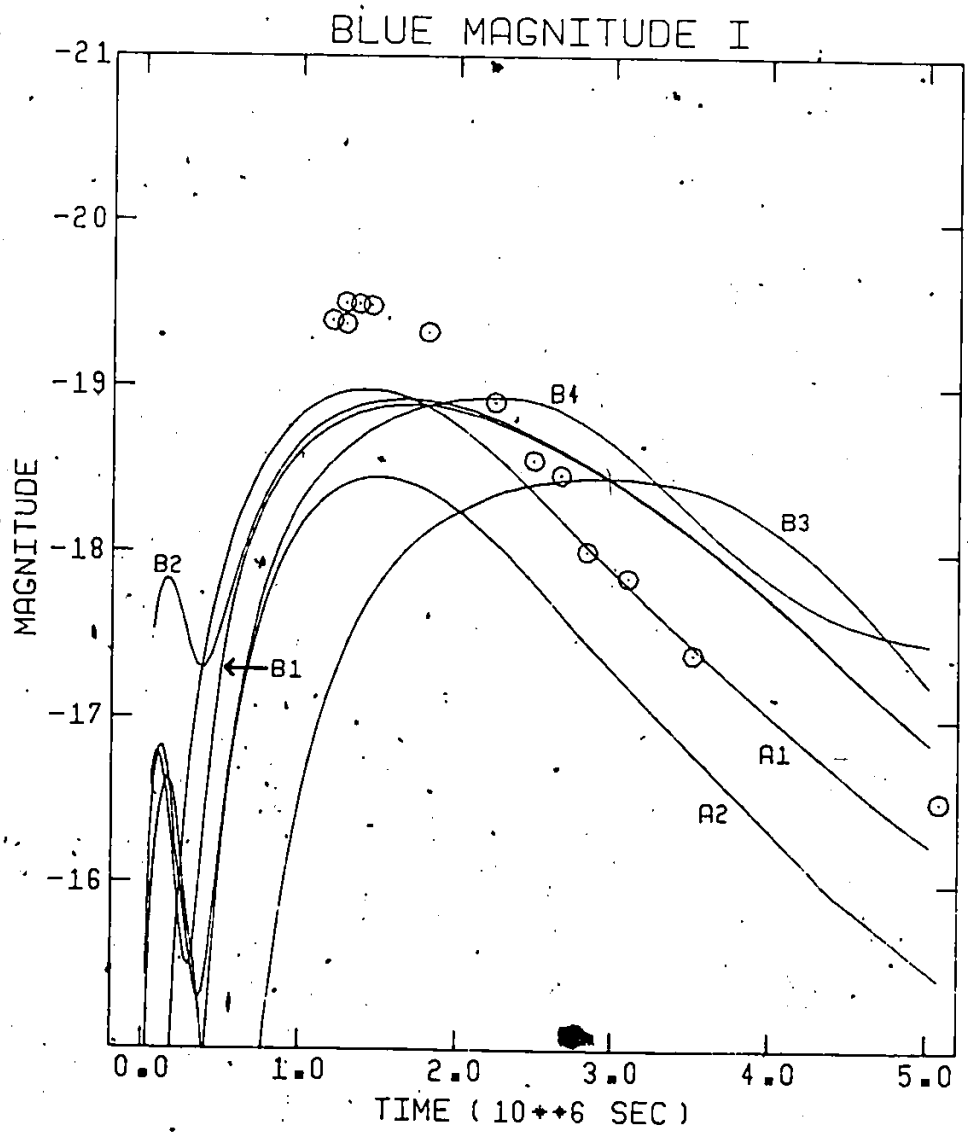
BLUE MAGNITUDE I
MAGNITUDE
-21
-20
-19
-18
-17
-16
B4
B3
B2
B1
A1
A2
0.0
1.0
2.0
3.0
4.0
5.0
TIME (10**6 SEC)

Figure 5-35

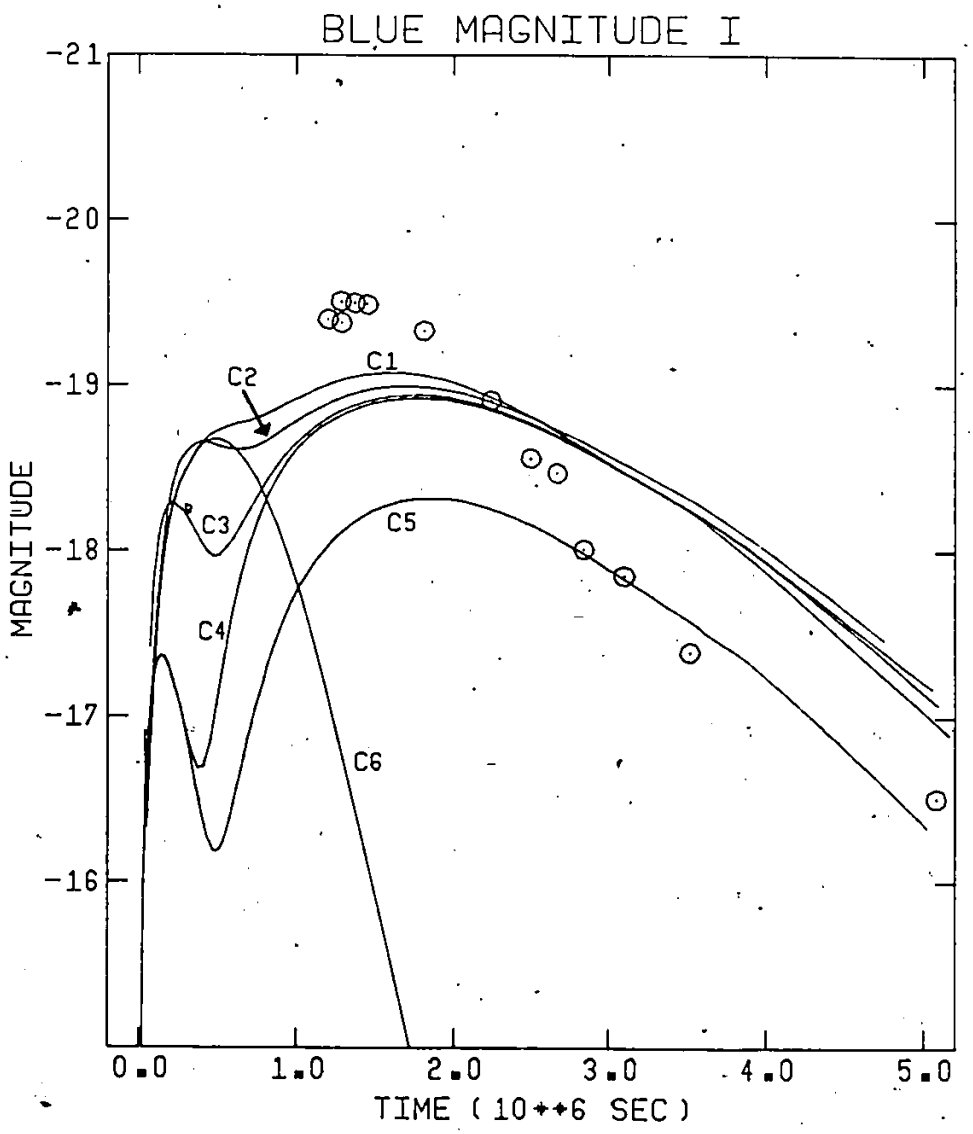
BLUE MAGNITUDE I
MAGNITUDE
-21
-20
-19
-18
-17
-16
C1
C2
C3
C4
C5
C6
0.0
1.0
2.0
3.0
4.0
5.0
TIME (10**6 SEC)

Figure 5-36

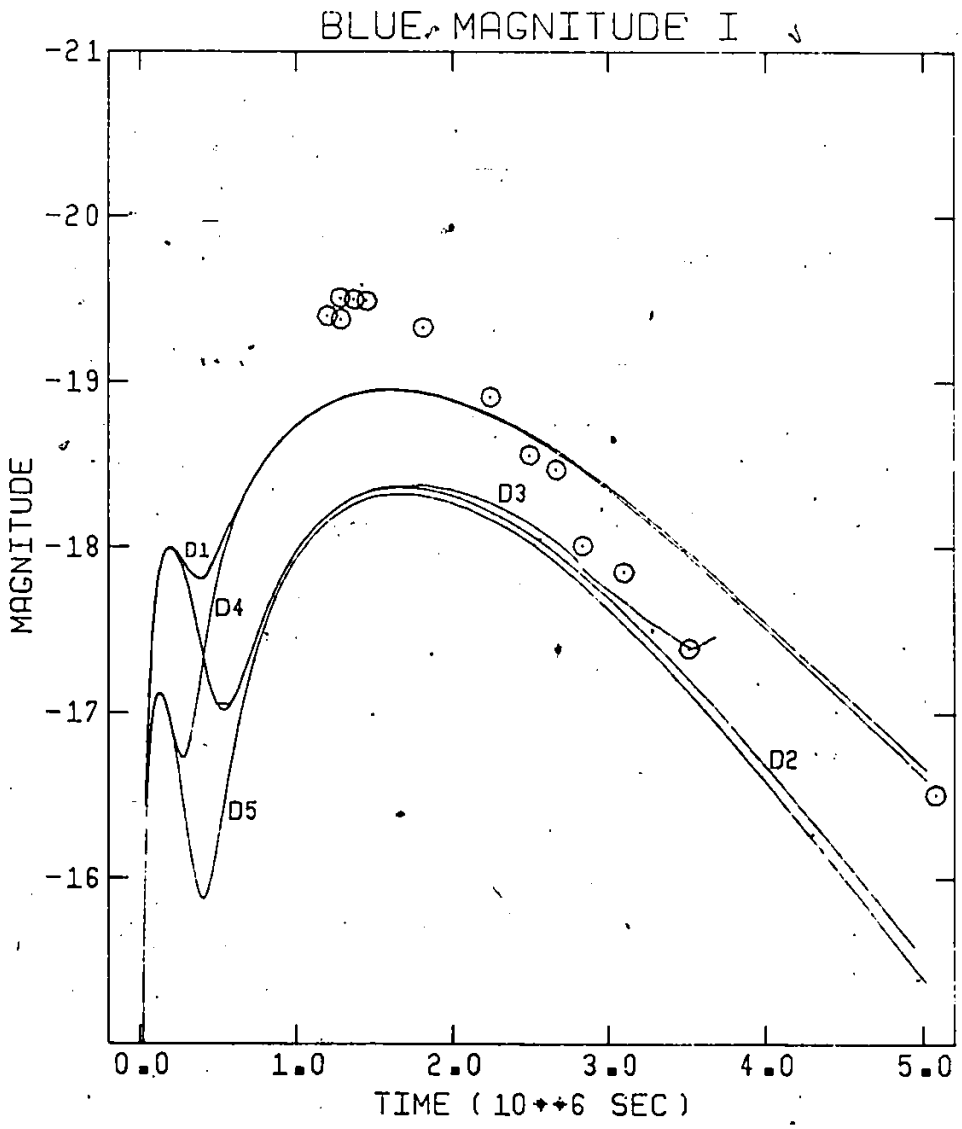
BLUE MAGNITUDE I
MAGNITUDE
-21
-20
-19
-18
-17
-16
D1
D2
D3
D4
D5
0.0
1.0
2.0
3.0
4.0
5.0
TIME (10**6 SEC)

Figure 5-37

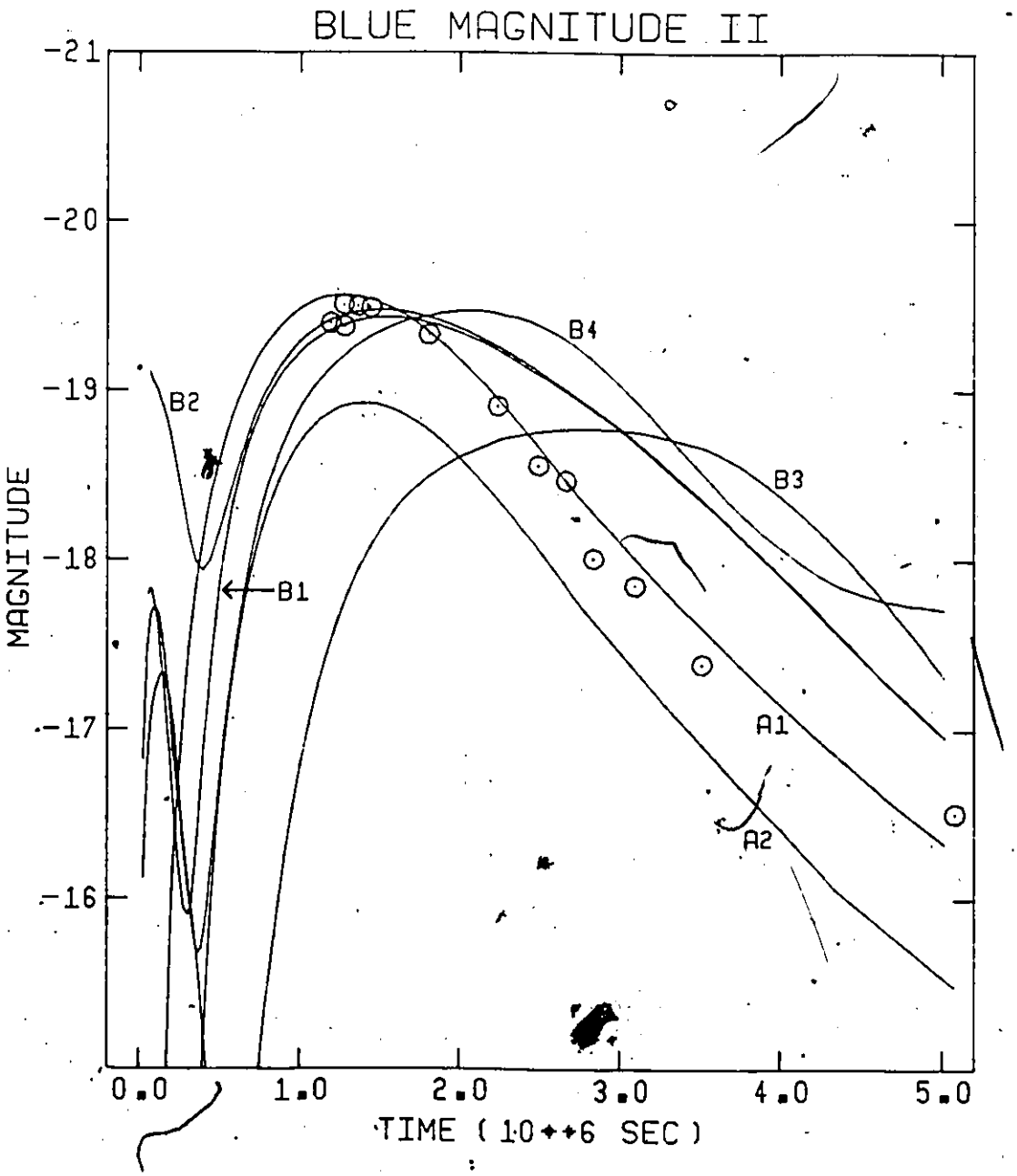
BLUE MAGNITUDE II
-21
-20
-19
-18
-17
-16
MAGNITUDE
B2
B4
B3
B1
A1
A2
0.0
1.0
2.0
3.0
4.0
5.0
TIME (10++6 SEC)

Figure 5-38

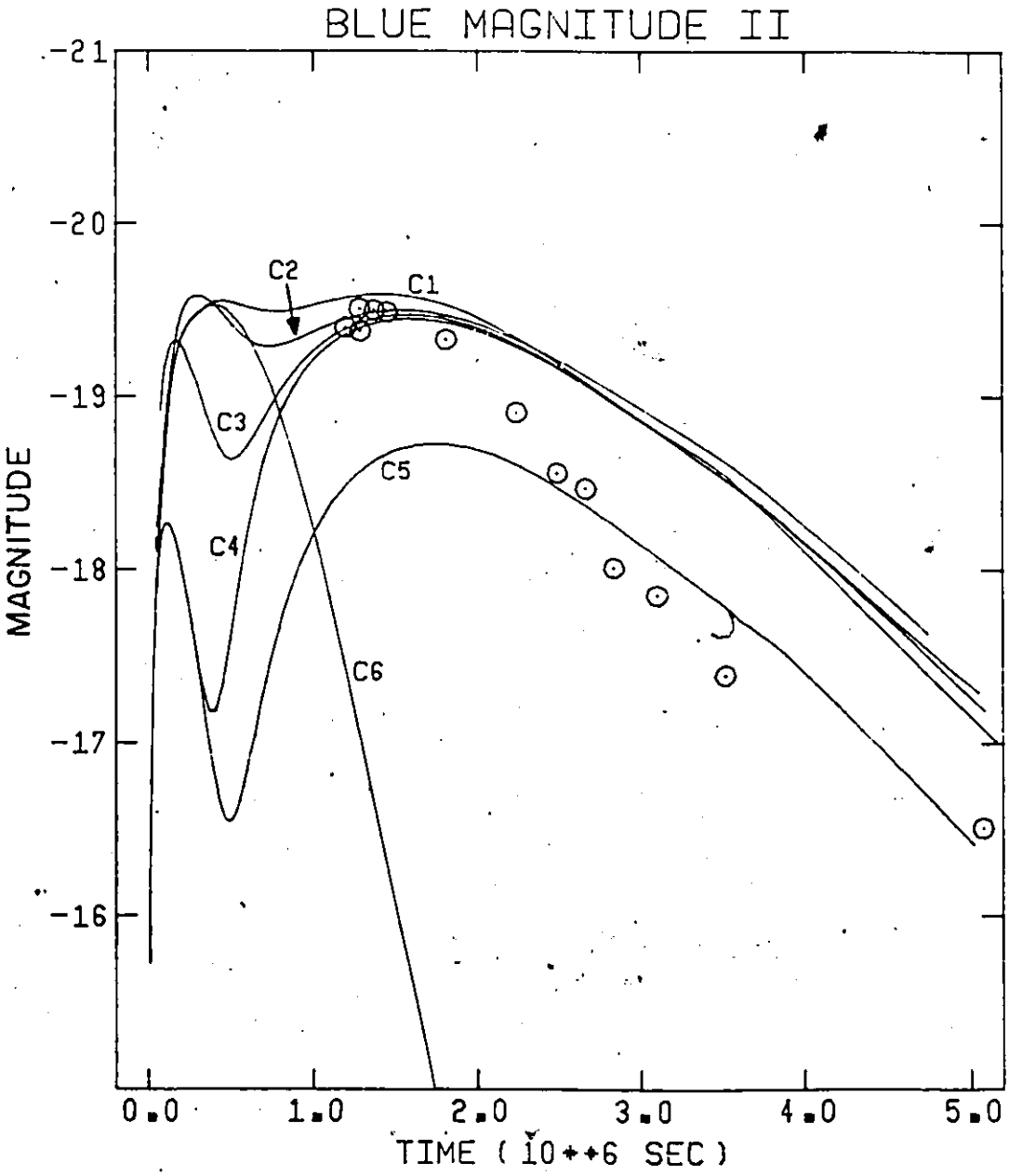
BLUE MAGNITUDE II
MAGNITUDE
-21
-20
-19
-18
-17
-16
C1
C2
C3
C4
C5
C6
0.0
1.0
2.0
3.0
4.0
5.0
TIME (I0++6 SEC)

Figure 5-39

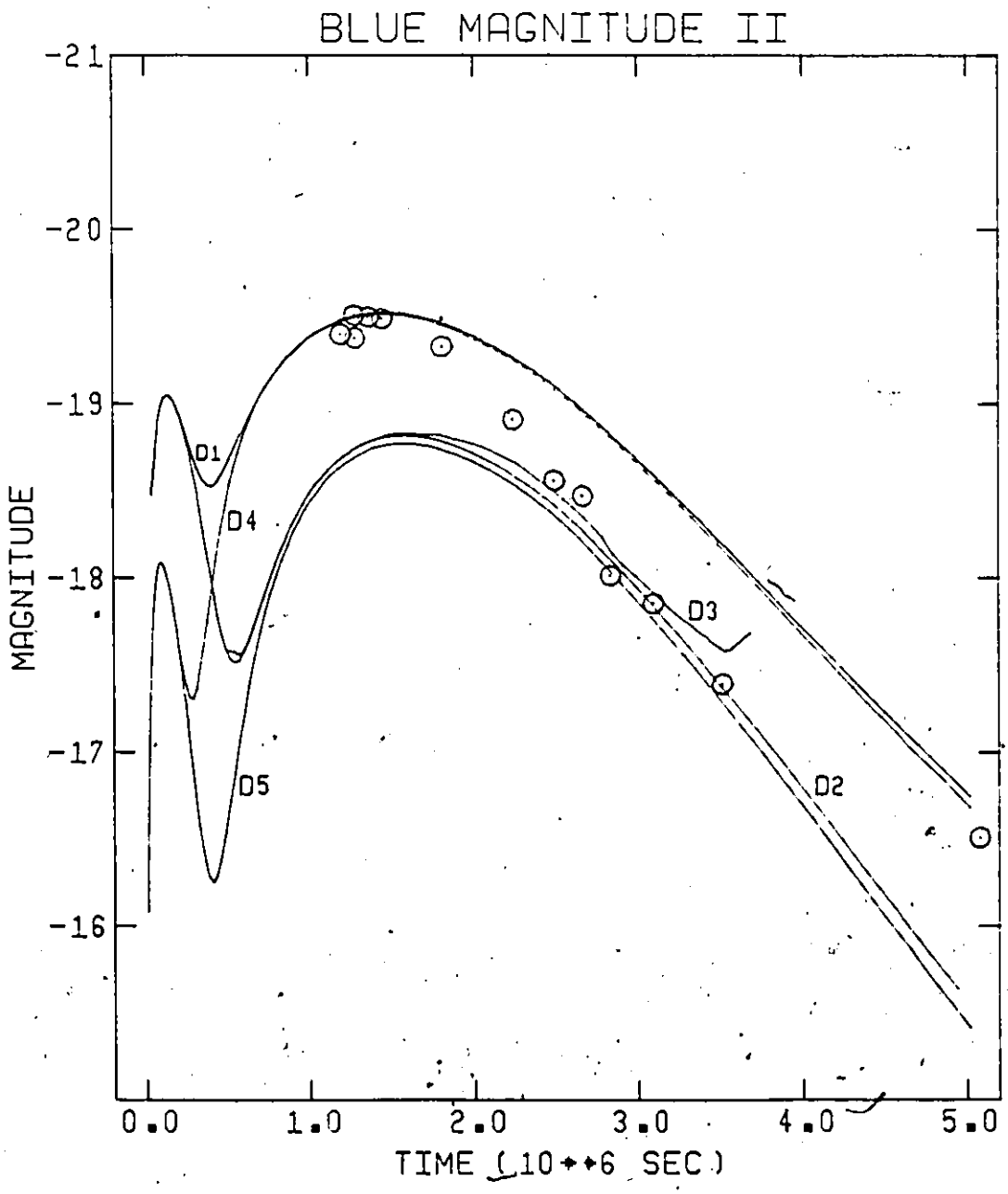
BLUE MAGNITUDE II
-21
-20
-19
-18
-17
-16
MAGNITUDE
D1
D4
D5
D3
D2
0.0
1.0
2.0
3.0
4.0
5.0
TIME (10**6 SEC)

Figures 5-40 to 5-45

Colour index curves versus time, for each model. Figures 5-40 to 5-42 are based on untruncated spectra, while Figures 5-43 to 5-45 are based on spectra truncated at 4000 Å. The data points are for SN 1981b, taken from Buta and Turner (1983).

Figure 5-40

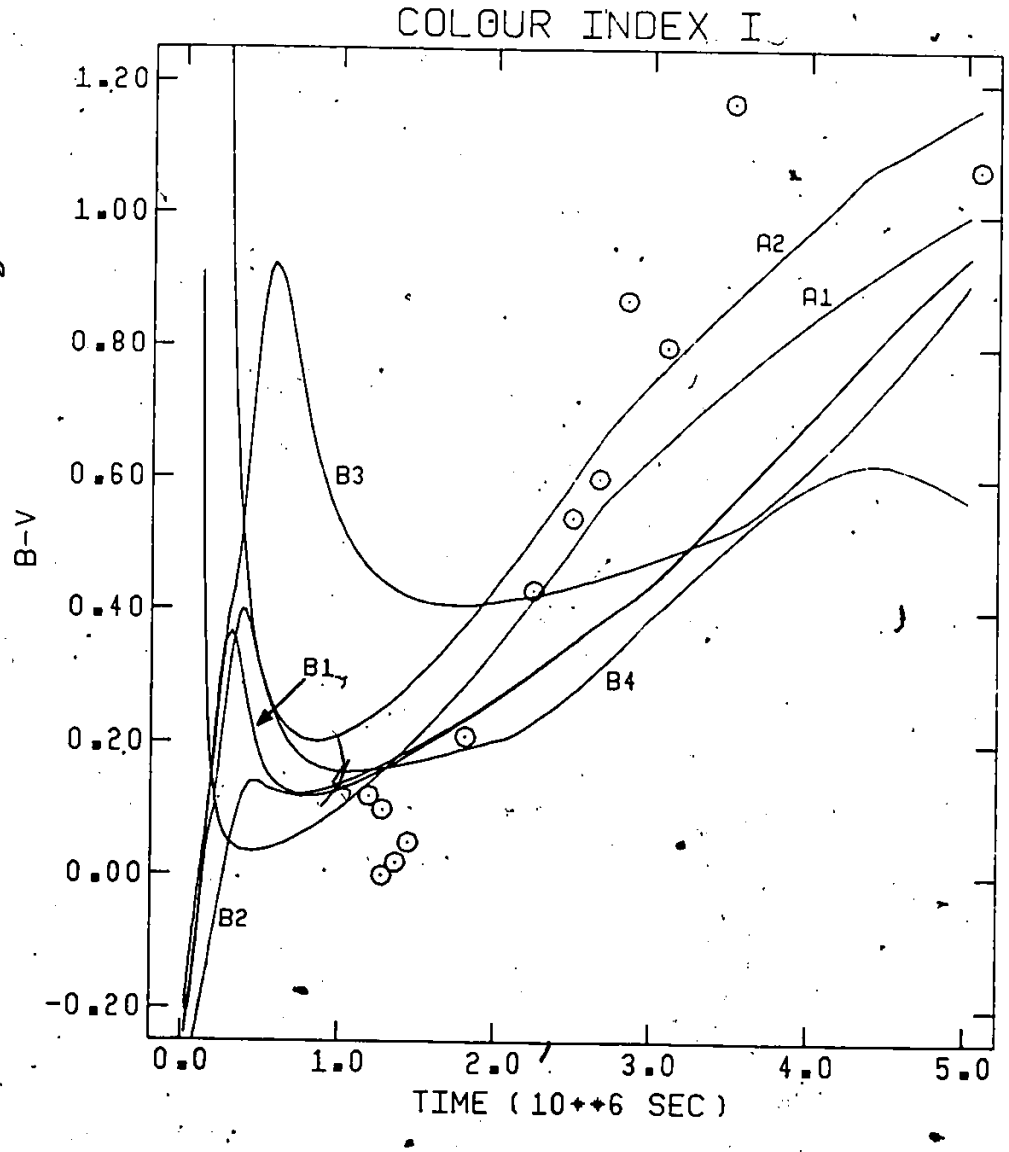
COLOUR INDEX I
B-V
1.20
1.00
0.80
0.60
0.40
0.20
0.00
-0.20
0.0
1.0
2.0
3.0
4.0
5.0
TIME (10**6 SEC)
A2
A1
B3
B1
B4
B2

Figure 5-41

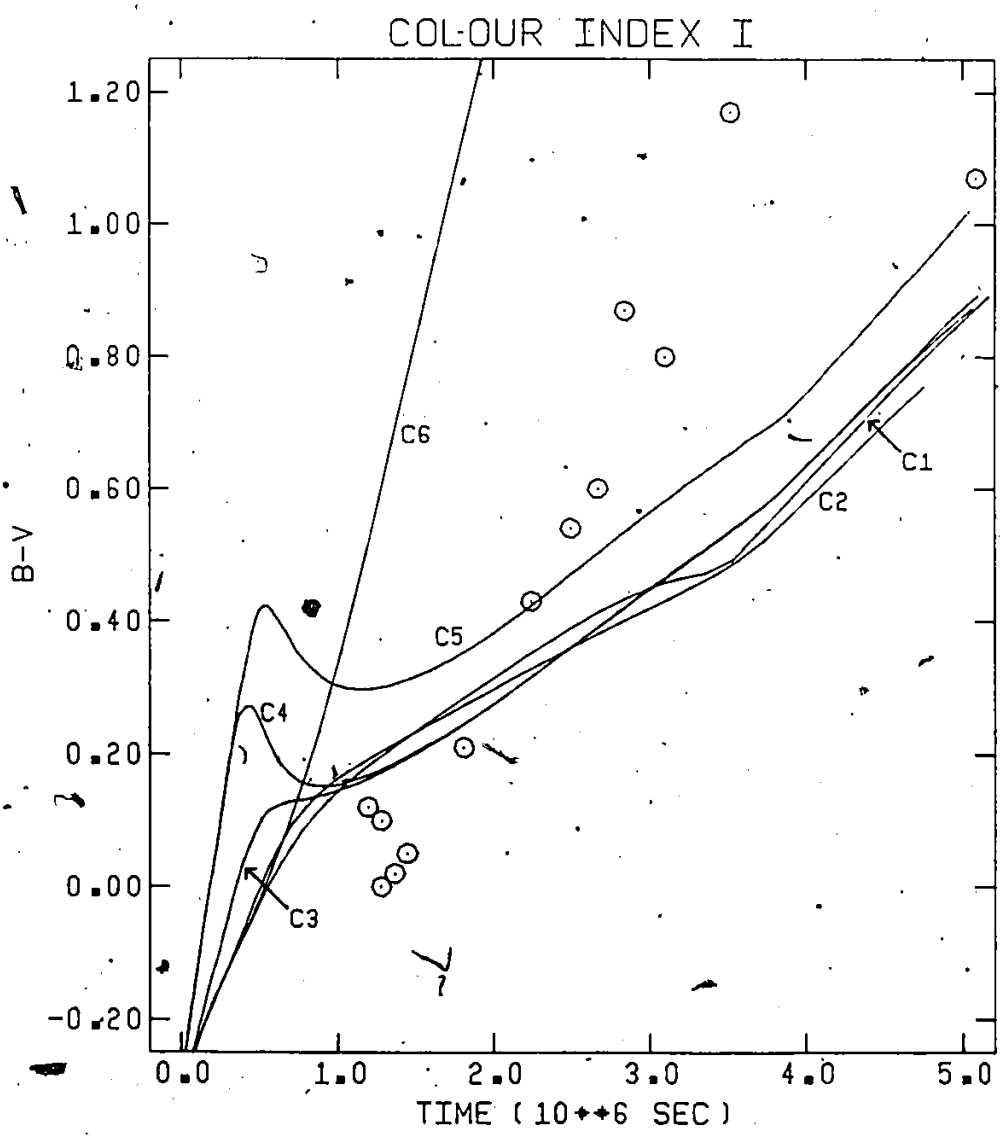
COLOUR INDEX I
B-V
1.20
1.00
0.80
0.60
0.40
0.20
0.00
-0.20
0.0
1.0
2.0
3.0
4.0
5.0
TIME (10**6 SEC)
C1
C2
C3
C4
C5
C6

Figure 5-42

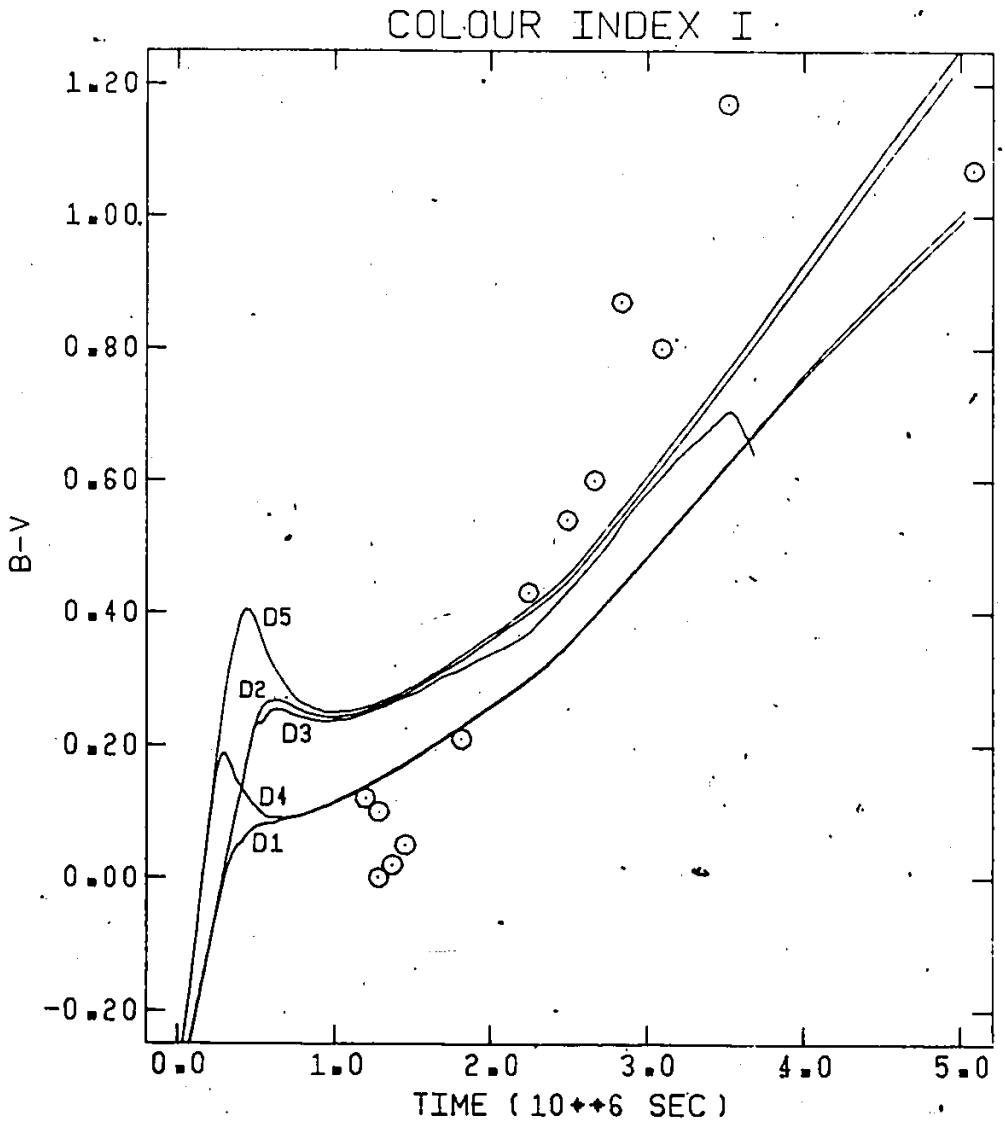
COLOUR INDEX I
B-V
1.20
1.00
0.80
0.60
0.40
0.20
0.00
-0.20
0.0
1.0
2.0
3.0
4.0
5.0
TIME (10++6 SEC)
D5
D2
D3
D4
D1

Figure 5-43

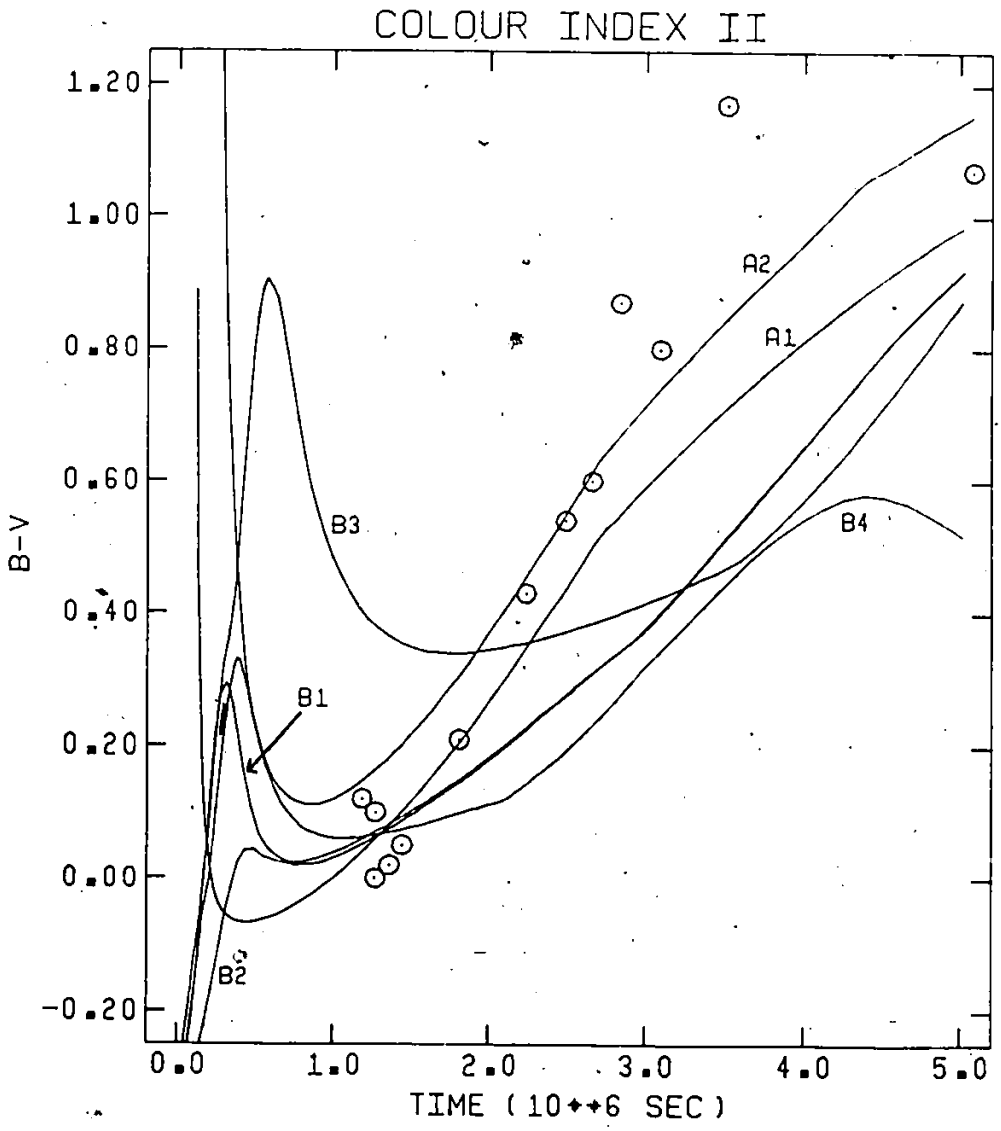
COLOUR INDEX II
1.20
1.00
0.80
0.60
0.40
0.20
0.00
-0.20
B-V
0.0
1.0
2.0
3.0
4.0
5.0
TIME (10++6 SEC)
A2
A1
B3
B4
B1
B2

Figure 5-44

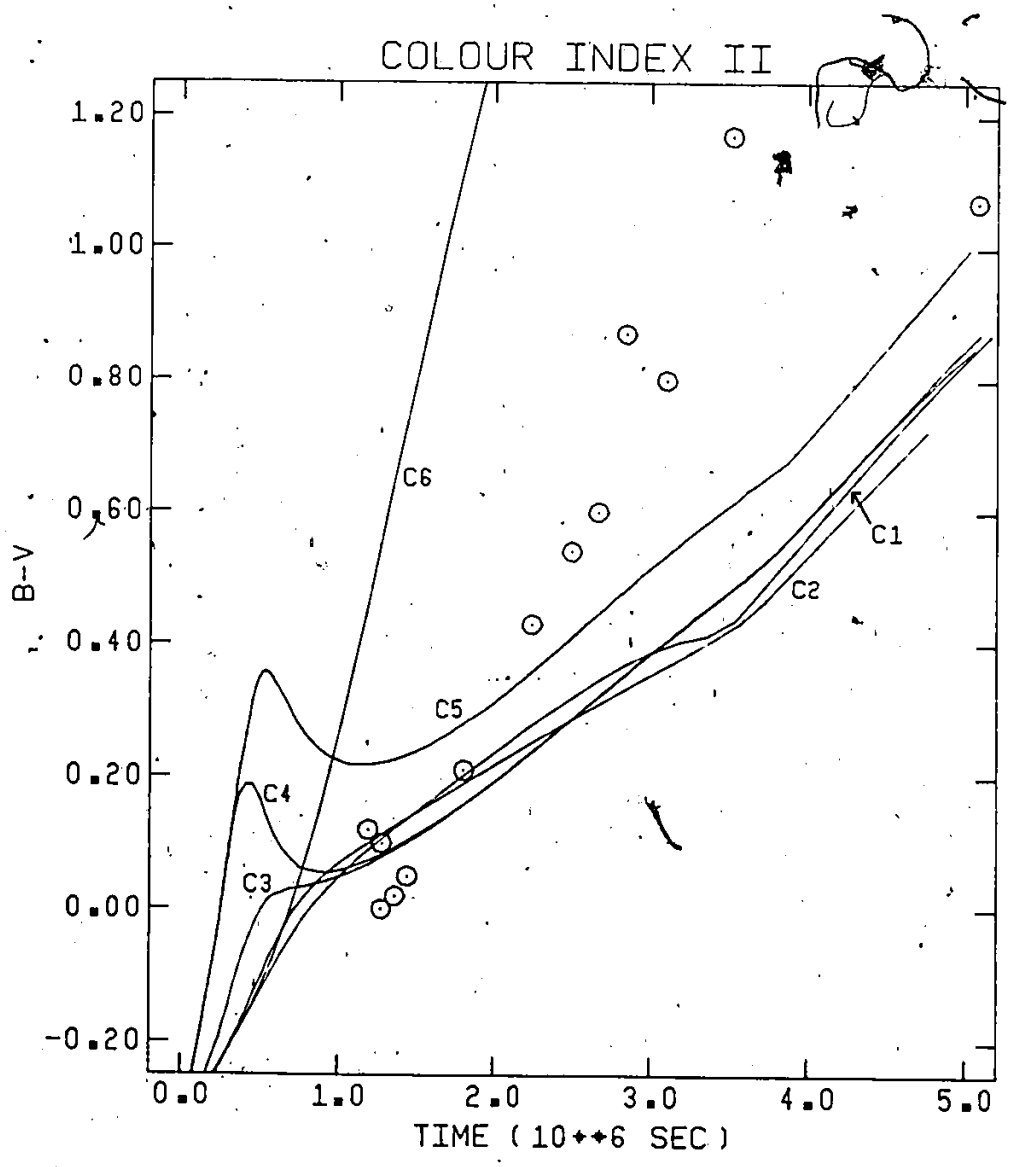
COLOUR INDEX II
1.20
1.00
0.80
0.60
0.40
0.20
0.00
-0.20
B-V
0.0
1.0
2.0
3.0
4.0
5.0
TIME (10**6 SEC)
C6
C1
C2
C5
C4
C3

Figure 5-45

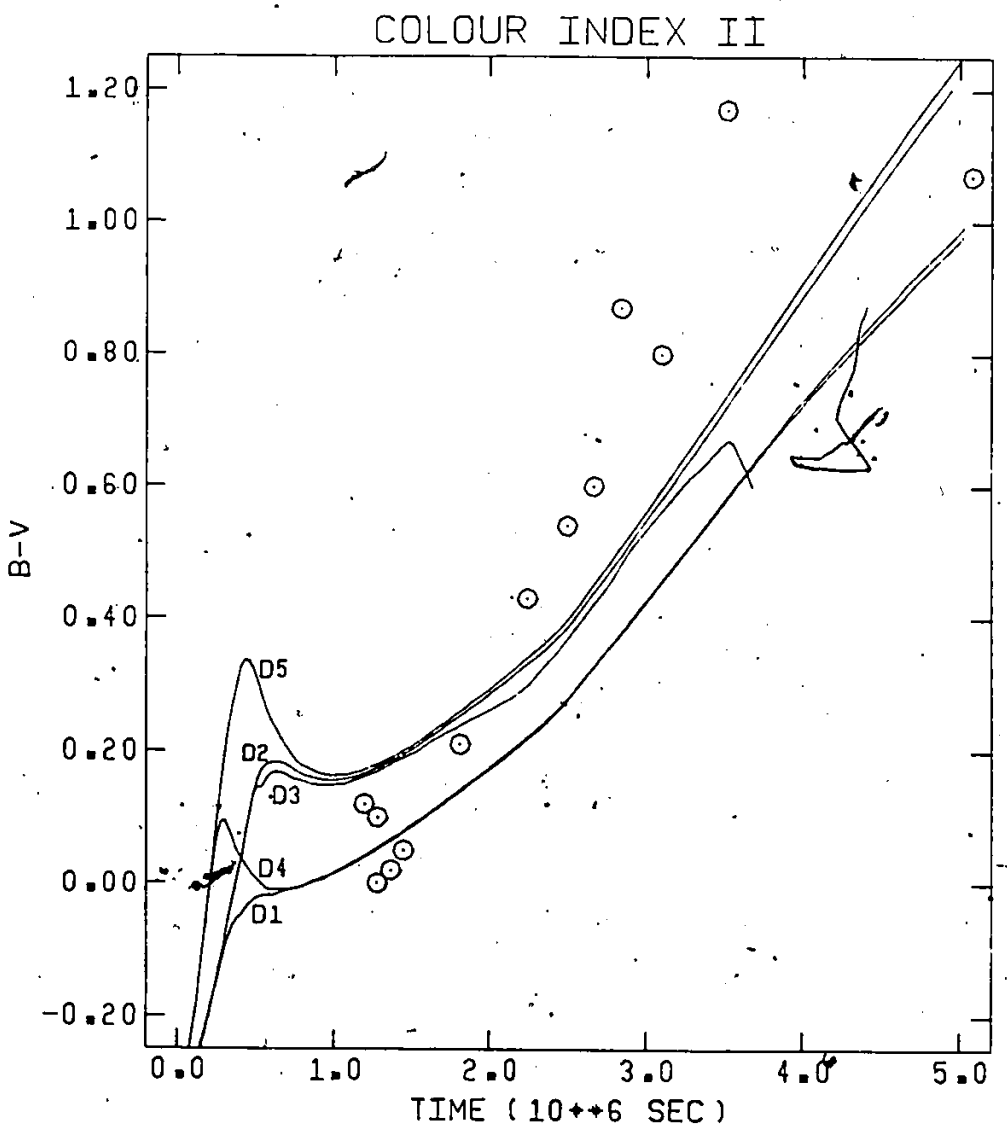
COLOUR INDEX II
1.20
1.00
0.80
0.60
0.40
0.20
0.00
-0.20
B-V
D5
D2
D3
D4
D1
0.0
1.0
2.0
3.0
4.0
5.0
TIME (10**6 SEC)

CHAPTER VI

CONCLUSION

In recent years great advances have been made in the understanding of Type I supernovae. The success of the deflagrating white dwarf model has made it the 'standard picture' in the field. The hypothesis that ^{56}Ni decay is responsible for the late-time light curve is now generally accepted.

The proposition that large helium stars (typified by the class of R Cor Bor stars) might be SN I progenitors was made by Wheeler (1978). Such stars could account for the intrinsic variability of SN I noted by Pskovskii (1977), but the reality of this variability is in doubt (Sandage and Tamann, 1982). Meanwhile, the bare white dwarf models have gained in credibility, causing the alternatives to be largely neglected. Lasher (1975; 1980) showed that shock heating of a large envelope could explain the hump of the SN I light curve, but his models did not include radioactivity and could not explain the tail of the light curve. The present work indicates that radioactivity cannot be combined with a large, shock-heated envelope without insurmountable difficulties. On the other hand the bare white dwarf models considered in this thesis show no serious disagreements with the SN I data. It is possible that further refinement of the input physics will allow these models to satisfy all the observational constraints.

The possibility of the progenitor having a small envelope cannot

be ruled out. Even a small envelope, by changing the mass of the system, would alter the slopes of the colour index curve and the light curve (which is the distinction between the 'fast' and 'slow' types). The 'bare' models themselves require a companion star as a source of accretion matter. It is possible that an accretion disk or envelope might form around the otherwise 'bare' white dwarf.

If R Cor Bor stars do not produce Type I supernova, then what do they produce? It may be that the degenerate core never becomes massive enough to trigger a supernova, or it could be that these stars produce relatively rare, atypical supernovae that do not fit into the standard Type I category.

In the next few years the nature of the progenitors of Type I supernovae may well be resolved. Understanding of Type II supernovae is also proceeding apace. Nevertheless, accumulating statistics suggest that there may be further classes of supernovae, which someday will also demand our theoretical understanding.

APPENDIX A

TIME CENTERING IN THE DIFFUSION EQUATIONS

The supernova ejecta became radiation dominated typically about 10^4 seconds after the start of the explosion. The leading term in the internal energy is then $E = aT^4V$, and the radiation diffusion equation (3.6) may be written as

$$L = -\sigma \frac{\partial E}{\partial m} \quad , \qquad \text{where } \sigma = \frac{(4\pi r^2)^2 \rho c}{3\kappa} \quad . \tag{A.1}$$

Neglecting the (small) PdV term, equation (3.13) is then

$$\frac{\partial E}{\partial t} = \frac{\partial}{\partial m} \sigma \frac{\partial E}{\partial m} + \Sigma \quad . \tag{A.2}$$

This is a standard heat flow equation with a source term. Such equations are discussed in detail by Richtmeyer and Morton (1967), hereafter RM. The stability of equation (A.2) is the same as for the homogeneous version with $\Sigma = 0$ (see section 8.4 of RM).

The form of equations (3.16) and (3.25) correspond to finite difference scheme 5 in Table 8.1 of RM. For the choice of $\theta = 0$ this scheme is explicit but must satisfy the stability criterion

$$2\sigma \, \Delta t < (\Delta m)^2 \quad . \tag{A.3}$$

For the choice $\theta \geq \frac{1}{2}$ the equations are always stable but are implicit (i.e. a matrix must be diagonalized).

Define a diffusion time t_d (across one zone of width r) as

$$t_d = \frac{\kappa\rho}{c}(\Delta r)^2 = \frac{(\Delta m)^2}{3\sigma} . \qquad (A.4)$$

Define also a zone light-crossing time $t_c = \Delta r/c$. The stability criterion (A.3) for $\theta = 0$ is then simply $\Delta t \leq \frac{3}{2} t_d$. The flux limiter effectively limits diffusion by substituting t_c for t_d if $t_c > t_d$. In actual supernova calculations this happens after about eight days at which time $t_d = t_c \leq 100$ seconds. Continuing the calculations out to fifty days using this criterion ($\Delta t < \frac{3}{2} t_c$) is prohibitive as it would require perhaps a further fourteen thousand iterations. Alternatively, the implicit scheme with $\theta = \frac{1}{2}$ has no such restriction on the time step and only about fourteen hundred further iterations are necessary.

The choice of $\theta = \frac{1}{2}$ has a further benefit. RM point out that this choice is accurate to second order in the time step Δt whereas other values of θ are only accurate to first order. For these reasons the value $\theta = \frac{1}{2}$ has been adopted for the calculations and a subroutine called DIFFUSE has been written to solve the radiation diffusion equation implicitly.

APPENDIX B

THE EQUATION OF STATE FOR THE ELECTRONS

Given the number density of electrons and the temperature, it is desired to calculate the pressure, energy, and entropy of the electrons. Under the conditions of interest ionisation is virtually complete; the electrons are free and form a Fermi gas. To a good approximation an electron gas is non-interacting, so the equation of state for a non-interacting Fermi gas is developed first; subsequently the corrections due to interactions are added.

In statistical mechanics the thermodynamic properties of a gas are determined by integration over phase space. For a perfect (i.e. non-interacting) gas the distribution function is isotropic in momentum space and for the case of Fermions takes the form

$$f(p) = [1+\exp\{(\varepsilon-\mu)/kT\}]^{-1} \qquad (B.1)$$

where ε is the kinetic energy and μ is the chemical potential (excluding rest mass). The pressure, the particle number density, and the energy density are given by the integrals

$$P = \frac{g}{h^3}\cdot\frac{1}{3}\int_0^\infty pv\cdot 4\pi p^2 f(p)dp \quad , \qquad (B.2)$$

$$n = \frac{g}{h^3} \int_0^\infty 4\pi p^2 f(p) dp \quad , \tag{B.3}$$

$$E = \frac{g}{h^3} \int_0^\infty \epsilon \, 4\pi p^2 f(p) dp \quad , \tag{B.4}$$

where g is the spin multiplicity factor and is two for electrons. Define

$$\alpha \equiv \frac{-\mu}{kT} \quad , \tag{B.5}$$

$$\beta \equiv \frac{kT}{mc^2} \quad , \tag{B.6}$$

$$x = \frac{\epsilon}{kT} \quad , \tag{B.7}$$

$$\lambda \equiv \frac{4\pi}{h^3} (2mkT)^{3/2} \quad , \tag{B.8}$$

where m is the electron mass. With the aid of the above definitions and the distribution function (B.1) one obtains

$$P = \frac{2}{3} \lambda kT \cdot G(\alpha,\beta) \quad , \tag{B.9}$$

$$n = \lambda \cdot H(\alpha,\beta) \quad , \tag{B.10}$$

$$E = \lambda kT \cdot I(\alpha,\beta) \quad , \tag{B.11}$$

where

$$G(\alpha,\beta) = \int_0^\infty \frac{x^{3/2}(1+\frac{1}{2}\beta x)^{3/2}}{1+\exp(\alpha+x)} dx \quad , \tag{B.12}$$

$$H(\alpha,\beta) = \int_0^\infty \frac{x^{1/2}(1+\frac{1}{2}\beta x)^{1/2}(1+\beta x)}{1+\exp(\alpha+x)}\,dx\,, \qquad (B.13)$$

$$I(\alpha,\beta) = \int_0^\infty \frac{x^{3/2}(1+\frac{1}{2}\beta x)^{1/2}(1+\beta x)}{1+\exp(\alpha+x)}\,. \qquad (B.14)$$

Since n, β and λ are known, equation (B.10) may be solved for the parameter α. The pressure and energy can then be evaluated using equations (B.9) and (B.11). Unfortunately, the integrals (B.12) to (B.14) cannot be analytically solved; hence various approximation schemes have been developed to evaluate them. To this purpose the (α,β) plane is divided into four regions: i) non-degenerate ($\alpha \gg 0$); ii) very degenerate ($\alpha \ll 0$); iii) low temperature, intermediate degeneracy ($\beta \ll 1$, $\alpha \sim 0$); and (iv) the remainder ($\beta \sim 1$, $\alpha \sim 0$). These regions are each considered in turn.

i) Non-degenerate regime ($\alpha \gg 0$)

In practice the boundary to this region is taken to be

$$H(\alpha,\beta) < 0.016 + 0.04\beta \quad (\text{i.e. } \alpha \geq 4)\,. \qquad (B.15)$$

The integrals (B.12) to (B.14) may be expanded in powers of $\exp(-\alpha-x)$ and then integrated term by term to yield

$$G(\alpha,\beta) = \frac{3}{8^{1/2}} \sum_{j=1}^{\infty} \frac{(-)^{j+1} e^{-\alpha j}}{j^{5/2}}\, z^{1/2} e^z K_2(z)\,, \qquad (B.16)$$

$$H(\alpha,\beta) = \frac{1}{2^{\frac{1}{2}}} \sum_{j=1}^{\infty} \frac{(-)^{j+1} e^{-\alpha j}}{j^{3/2}} z^{\frac{1}{2}} e^{z} K_2(z) , \qquad (B.17)$$

$$J(\alpha,\beta) = \frac{1}{2^{\frac{1}{2}}} \sum_{j=1}^{\infty} \frac{(-)^{j+1} e^{-\alpha j}}{j^{5/2}} z^{\frac{1}{2}} e^{z} [zK_3(z) - K_2(z) - zK_2(z)] , \qquad (B.18)$$

where $z = j/\beta$. The K's are modified Bessel functions, and may be expanded in asymptotic series (see Abramowitz and Stegun, 1964) to yield

$$f_1 = 1 + \frac{15}{8}\beta + \frac{105}{128}\beta^2 - \frac{315}{1024}\beta^3 + \cdots , \qquad (B.19)$$

$$f_2 = 1 + \frac{15}{16}\beta + \frac{105}{512}\beta^2 + \cdots , \qquad (B.20)$$

$$e^{-\alpha} = \frac{2H(\alpha,\beta)}{\pi^{\frac{1}{2}} f_1} + \frac{2^{\frac{1}{2}}[H(\alpha,\beta)]^2 f_2}{\pi \cdot f_1^3} , \qquad (B.21)$$

$$f_3 = \frac{3}{2} + \frac{75}{16}\beta + \frac{735}{256}\beta^2 - \frac{2835}{2048}\beta^3 + \cdots , \qquad (B.22)$$

$$f_4 = \frac{3}{2} + \frac{75}{32}\beta \frac{735}{1024}\beta^2 - \cdots . \qquad (B.23)$$

Hence

$$P = nkT\left(1 + \frac{H(\alpha,\beta)}{(8\pi)^{\frac{1}{2}}} \cdot \frac{f_2}{f_1^2}\right) \qquad (B.24)$$

and

$$E = nkT \frac{f_3}{f_1}\left(1 + \frac{H(\alpha,\beta)}{(8\pi)^{\frac{1}{2}}} \cdot \frac{f_4}{f_3 f_1}\right) . \qquad (B.25)$$

Note that equations (B.19) to (B.23) involve power series in the parameter β. For accuracy, β should not exceed ~ 0.1 or so. This is assured in practice by restricting the applicability of these results to the regime satisfying ($\rho < 1000$ g-cm^{-3}) as well as condition (B.15).

The regime ($\rho > 1000$ g-cm^{-3}, $\alpha > 4$) is treated as in section (iv).

ii) Very degenerate regime ($\alpha \ll 0$)

In practice the boundary of this regime is

$$H(\alpha,\beta) > .14 + 140\,\beta + 60\,\beta^2 \quad \text{(i.e. } \alpha \leq -8\text{)}. \tag{B.26}$$

The integrals (B.12) to (B.14) may be expanded using Sommerfeld's lemma (see e.g. Chandrasekhar 1939). After some lengthy algebra one obtains

$$G(\alpha,\beta) \simeq (5\cdot 2^{\frac{1}{2}}\,\beta^5)^{-\frac{1}{2}}\{(2x-3+4\pi^2\beta^2)(x^2+x)^{\frac{1}{2}} + 3\ell n(x^{\frac{1}{2}}+(x+1)^{\frac{1}{2}}) + \frac{7}{15}\,\pi^4\beta^4(2x-1)\left(\frac{x+1}{x^3}\right)^{\frac{1}{2}}\} \tag{B.27}$$

$$H(\alpha,\beta) = \frac{1}{18^{\frac{1}{2}}}\left(\frac{x}{\beta}\right)^{3/2}\{1 + \left(\frac{\pi\beta}{x}\right)^2\left(x+\frac{1}{2}\right) + \frac{7}{40}\left(\frac{\pi\beta}{x}\right)^4\}\,, \tag{B.28}$$

$$I(\alpha,\beta) = \frac{x^{3/2}}{2^{\frac{1}{2}}\beta^{5/2}}\{\frac{(x+1)^{\frac{1}{2}}}{4} + \frac{(x+1)^{\frac{1}{2}}}{8x} - \frac{1}{8x^{3/2}}\,\ell n(x^{\frac{1}{2}} + (x+1)^{\frac{1}{2}}) + \left(\frac{\pi\beta}{x}\right)^2 \cdot \frac{(x+1)^{\frac{1}{2}}}{6}(3x+1) + \frac{7}{120}\left(\frac{\pi\beta}{x}\right)^4(2x^2-x+1)(x+1)^{\frac{1}{2}}\}\,, \tag{B.29}$$

where x is now defined as

$$x = \alpha^2\beta^2 + |2\alpha\beta|\,. \tag{B.30}$$

Equation (B.28) may be solved iteratively for x as H and β are given; a good initial estimate is

$$x = \left(\frac{h}{mc}\right)^2\left(\frac{3n}{8\pi}\right)^{2/3}. \tag{B.31}$$

This expression is correct in the extreme degeneracy limit.

At densities below $\rho = 10^5$ g-cm^{-3} both x and β are small and equations (B.27) and (B.29) are difficult to evaluate due to numerical inaccuracies. The following forms are then preferable

$$G(\alpha,\beta) = (512)^{-1/2}\left(\frac{x}{\beta}\right)^{5/2}\left\{\frac{8}{5} - \frac{4x}{7} + \frac{x^2}{3} - \frac{5x^3}{22} + \cdots + 4\left(\frac{\pi\beta}{x}\right)^2 (x+1)^{1/2}\right.$$
$$\left. + \frac{7}{15}\left(\frac{\pi\beta}{4}\right)^4 (2x-1)(x+1)^{1/2}\right\} , \qquad (B.32)$$

$$I(\alpha,\beta) = (512)^{-1/2}\left(\frac{x}{\beta}\right)^{5/2}\left\{\frac{8}{5} - \frac{2x}{7} + \frac{x^2}{9} - \frac{5x^3}{88} + \cdots + \left(\frac{\pi\beta}{x}\right)^2\left(4 + \frac{11x}{3} - \frac{5x^2}{6}\right.\right.$$
$$\left.\left. + \frac{19}{48}x^3 + \cdots\right) - \frac{7}{15}\left(\frac{\pi\beta}{x}\right)^4\left(1 - \frac{11x}{4} - \frac{19x^2}{8} + \frac{45x^3}{64} + \cdots\right)\right\} . \qquad (B.33)$$

iii) Intermediate degeneracy, low temperature regime ($\beta < 0.01$)

The integrals (B.12) to (B.14) are expanded in powers of β yielding

$$G(\alpha,\beta) = \int_0^\infty xf(\alpha,x)dx + \frac{3\beta}{4}\int_0^\infty x^2 f(\alpha,x)dx + \frac{3\beta^2}{32}\int_0^\infty x^3 f(\alpha,x)dx + \cdots , \qquad (B.34)$$

$$H(\alpha,\beta) = \int_0^\infty f(\alpha,x)dx + \frac{5\beta}{4}\int_0^\infty xf(\alpha,x)dx + \frac{7\beta^2}{32}\int_0^\infty x^2 f(\alpha,x)dx + \cdots , \qquad (B.35)$$

$$I(\alpha,\beta) = \int_0^\infty xf(\alpha,x)dx + \frac{5\beta}{4}\int_0^\infty x^2 f(\alpha,x)dx + \frac{7\beta^2}{32}\int_0^\infty x^3 f(\alpha,x)dx + \cdots , \qquad (B.36)$$

where

$$f(\alpha,x) = x^{1/2}[1+\exp(\alpha+x)]^{-1} . \qquad (B.37)$$

The integrals in equations (B.34) to (B.36) are functions of α only and have been tabulated for the range $-9 < \alpha < 5$, in steps of $\alpha = 0.1$. Equation (B.35) is solved for α using quadratic interpolation, whereupon G and I and hence the pressure and energy can be evaluated.

iv) Remaining regime ($\alpha > -8$, $\beta > 0.1$, $\rho > 1000$ g-cm^{-3})

The integrals (B.12) to (B.14) have been evaluated numerically at an array of points in the (log ρ, log T) plane, spaced ten points per decade in ρ and fifteen points per decade in T. The contributions from electron-positron pairs (see Appendix C) are also included. (In the other three regimes described above a negligible number of electron-positron pairs are formed and so their effects are omitted.) The pressure, energy, and entropy of the electrons are found directly by interpolation in this table.

Such a tabulated equation of state is of course conceptually simpler than the cumbersome approximations used for the other three regimes. The table could in principle be extended over the entire (ρ,T) plane but this is not practical due to the vast number of integrals that would have to be evaluated and stored. Furthermore, the expansions used in the other three regimes offer much greater accuracy than does the table, and are thus preferable.

To check the correctness and accuracy of the formulae used in the four different regimes the numerical discontinuities in the pressure and energy at the regime boundaries have been measured. Typically the discontinuities are only about one part in 10^4, which is remarkably good

under the circumstances. Emphasis is placed on accuracy in part because derivatives such as $\frac{\partial P}{\partial T}$ and $\frac{\partial E}{\partial T}$ are evaluated numerically (e.g. $\frac{\partial P}{\partial T}$ is determined by evaluating the pressure at two temperatures differing by 0.5%). Relatively small errors in the pressure or energy can result in much larger errors in the numerical derivatives.

Once the pressure and energy are evaluated as detailed above (for a non-interacting system), corrections for the interactions may be added. The most prominent are the Coulomb, the Thomas-Fermi and the exchange interactions; these effects are parametrised as a multiplicative factor 'f', defined by

$$f = 1.00116-4.56\times10^{-3}z-1.78\times10^{-5}z^2-0.03674(z^{1.515}-1.37)W^{\phi} \quad (B.38)$$

where

$$z \equiv \left(\frac{\mu_i}{\mu_e}\right)^{2/3} \quad (B.39)$$

and

$$W = \min\left(\frac{1}{2}V\mu_e, 10^{-4}\right) \quad (B.40)$$

and

$$\phi = 0.7670+0.2286z-0.01674z^2+(-0.1186+ + 0.002248z-0.01642z^2)\cdot\log_{10}W \; . \quad (B.41)$$

This expression for 'f' is a fit to the calculation of Salpeter (1961). His results are valid for an electron gas at zero temperature and a density greater than 10^4 g-cm^{-3}. The zero temperature assumption is adequate for degenerate electrons, but it is extended here to non-degenerate electrons merely for convenience. Also, f is taken to be density independent below $\rho = 10^4$ g-cm^{-3}. This is incorrect, but the

electron pressure is not dynamically significant at such densities. Furthermore at low density the radiation is the dominant source of pressure. For similar reasons the reduction in electron pressure due to recombination has also been omitted.

Once the pressure and energy have been determined the electron entropy is calculated. It follows from the Gibbs free energy

$$G = E + PV - TS = \mu N \quad . \tag{B.42}$$

This equation may be solved directly for S. The entropy is then converted to a dimensionless entropy per baryon by

$$\sigma = \frac{S}{R} \quad . \tag{B.43}$$

Hence

$$\sigma_e = \frac{E_e + P_e V}{RT} + \frac{\alpha_e}{\mu_e} \quad . \tag{B.44}$$

APPENDIX C

THE DENSITY OF ELECTRON-POSITRON PAIRS

At temperatures near 10^{10} K the typical photon energy is comparable to the electron rest mass energy. Hence the reaction

$$\gamma + \gamma \rightleftharpoons e^+ + e^- \tag{C.1}$$

will reach an equilibrium with a non-zero number of electron-positron pairs. At equilibrium the chemical potentials balance

$$2\mu_\gamma = \mu_e + \mu_p \tag{C.2}$$

where μ is the relativistic chemical potential

$$\mu = mc^2 - \alpha kT \tag{C.3}$$

The subscripts e and p refer to electrons and positrons respectively. Definitions (B.5) and (B.6) are used here for α and β. Equation (C.2) may be rearranged as

$$\alpha_e + \alpha_p = \frac{2}{\beta} \tag{C.4}$$

Let n_0 represent the density excess of electrons over positrons. This quantity is independent of the number of pairs created and follows from the mass density.

$$n_0 = \frac{\rho}{\mu_e m_{pr}} \tag{C.5}$$

where m_{pr} is the proton mass. Including the electron-positron pairs,

$$n_e = n_o + n_p \tag{C.6}$$

and since $n \propto H(\alpha,\beta)$ (from equation (B.10)), this implies

$$H(\alpha_e,\beta) = H(\alpha_o,\beta) + H(\alpha_p,\beta) \tag{C.7}$$

Equations (C.4) and (C.7) are a set of two equations in three unknowns (the three α's). α_o can be determined using the method of Appendix B, (i.e. by evaluating the electron equation of state in the absence of pairs). Equations (C.4) and (C.7) may then be solved. There are three regimes of interest.

i) Non-degenerate regime ($\alpha_o > 4$, $\beta^{-1} > 4$)

In this regime $H(\alpha,\beta) \propto \exp(-\alpha)$. Thus equation (C.7) becomes

$$\exp(-\alpha_e) = \exp(-\alpha_o) + \exp(-\alpha_p) \tag{C.8}$$

With the use of equation (C.4) this reduces to

$$\alpha_e = \beta^{-1} - \sinh^{-1}[\tfrac{1}{2}\exp(\beta^{-1}-\alpha_o)]$$

$$\alpha_p = \beta^{-1} + \sinh^{-1}[\tfrac{1}{2}\exp(\beta^{-1}-\alpha_o)]$$

ii) Very degenerate regime ($\alpha_o < -8$)

Since $n_e > n_o$ then $\alpha_e < \alpha_o$, i.e. $\alpha_e < -8$. Therefore by equation (C.4)

$$\alpha_p > 2\beta^{-1} + 8 . \tag{C.10}$$

Thus $\alpha_p >> \alpha_0$ and hence $n_p << n_0$. Therefore $n_e \simeq n_0$ and $n_p \simeq 0$. This may be explained conceptually as follows: The electron from a newly created pair must be added to the top of the Fermi sea, but since the electron gas is very degenerate, $kT << \epsilon_F$. Since the typical photon energy is of order kT, very few photons will exceed the threshold for pair production.

iii) Intermediate degeneracy

In this regime equations (C.4) and (C.7) are solved iteratively. A reasonable first approximation is

$$\alpha_e = \min(\alpha_0, \beta^{-1}) \quad . \tag{C.11}$$

Once α_e and α_p are found then the electron (and positron) pressure and energy are evaluated using equations (B.9) and (B.11).

APPENDIX D

NUCLEAR STATISTICAL EQUILIBRIUM

Consider the reaction

$$j\alpha \rightleftharpoons (j-1)\alpha + \alpha \qquad (D.1)$$

in which a nucleus compounded of j alpha particles dissociates by emitting one alpha particle (gamma-rays are also produced, but are not of concern here). The equilibrium number densities of the participating nuclei follow from the Saha equation (see for example Clayton, 1968)

$$\frac{n_{(j-1)\alpha} n_\alpha}{n_{j\alpha}} = \frac{(2\pi\mu kT)^{3/2}}{h^3} \frac{G_{(j-1)\alpha} G_\alpha}{G_{j\alpha}} e^{-Q_j/KT} , \qquad (D.2)$$

where

$$Q_j = (M_{(j-1)\alpha} + M_\alpha - M_{j\alpha})c^2 , \qquad (D.3)$$

and

$$\mu = \frac{M_{(j-1)\alpha} M_\alpha}{M_{j\alpha}} \simeq \left(\frac{j-1}{j}\right) M_\alpha . \qquad (D.4)$$

Define

$$x_j = \frac{n_{(j+1)\alpha}}{n_{j\alpha} n_\alpha} \qquad (D.5)$$

Hence

$$n_{j\alpha} = n_\alpha n_{(j-1)\alpha} x_{j-1} = n_\alpha^2 n_{(j-2)\alpha} x_{j-1} x_{j-2} = \cdots$$

$$= n_\alpha^j \prod_{i=1}^{j-1} x_i . \qquad (D.6)$$

The matter density ρ is given by

$$\rho = \sum_j M_{j\alpha} n_{j\alpha} = M_\alpha \sum_j j n_\alpha^j \prod_{i=1}^{j-1} x_i \quad . \qquad (D.7)$$

The partition functions $G_{j\alpha}$ may be taken to be unity for all the relevant nuclides as they all have spin zero ground states and no low energy excited states. Hence the Saha equation (D.2) reduces to

$$x_j = (2\pi M_\alpha kT/h^2)^{-3/2} \left(\frac{j+1}{j}\right)^{3/2} \exp(Q_{j+1}/kT) \quad . \qquad (D.8)$$

For a given temperature and density equation (D.7) may be solved implicitly for n_α (since the x_j are all known). The $n_{j\alpha}$ then follow from equation (D.6).

The results (including the total binding energy) have been tabulated at an array of points in the (ρ,T) plane, and are interpolated as is necessary.

APPENDIX E

THE JUMP CONDITIONS AT A SHOCK FRONT

Consider a one-dimensional coordinate system attached to (i.e. comoving with) and normal to the shock surface. Let subscripts 1 and 2 refer to pre-shock and post-shock conditions respectively.

The conservation equations at the shock front are (see e.g. Landau and Lifshitz 1959)

mass flux $$\rho_1 v_1 = \rho_2 v_2 \tag{E.1}$$

momentum flux $$P_1 + \rho_1 v_1^2 = P_2 + \rho_2 v_2^2 \tag{E.2}$$

energy $$E_1 + P_1 V_1 + \frac{1}{2} v_1^2 = E_2 + P_2 V_2 + \frac{1}{2} v_2^2 . \tag{E.3}$$

Consider the fluid to consist of radiation plus a gas of non-degenerate particles. Then

$$P = AT^4 + BT/V \tag{E.4}$$

and

$$E = 3AT^4 V + \frac{3}{2} BT . \tag{E.5}$$

The constant A is one-third of the Stephan-Boltzmann constant and B is the effective gas constant for the ions and the electrons:

$$B = R\mu_e^{-1} + R\mu_i^{-1} \tag{E.6}$$

Define Δ as the velocity discontinuity

$$\Delta \equiv v_1 - v_2 . \tag{E.7}$$

Assume that all pre-shock conditions (subscript 1) are known. With the specification of one more parameter (e.g. Δ) equations (E.1) through (E.3) may be solved for the post-shock conditions. From equations (E.1) and (E.2) it follows that

$$\Delta^2 = (P_2-P_1)(V_1-V_2) \tag{E.8}$$

and

$$v_1^2-v_2^2 = (P_2-P_1)(V_1+V_2) . \tag{E.9}$$

From equations (E.3) and (E.5) follows

$$8AT_1^4V_1 + 5BT_1 - 8AT_2^4V_2 - 5BT_2 + V_1P_2 + V_2P_2 - V_1P_1 - V_2P_1 = 0 . \tag{E.10}$$

The pressures may be eliminated using equation (E.4). Equations (E.8) and (E.10) form a set of two equations in two unknowns. Eliminating V_2 results in

$$\begin{aligned} &18A^2BV_1T_2^9 + 6A^2V_1(8AT_1^4V_1 + 5BT_1+\Delta^2)T_2^8 + 9AB^2T_2^6 \\ &+ 18AB(2P_1V_1+\Delta^2)T_2^5 - A(96A^2T_1^8V_1^2 + 132ABT_1^5V_1 + 45B^2T_1^2 \\ &+ 68AT_1^4V_1\Delta^2 + 44BT_1\Delta^2 + 7\Delta^4)T_2^4 + 15B^2P_1T_2^2 - BP_1(54AT_1^4V_1 \\ &+ 30BT_1 + 2\Delta^2)T_2 + P_1(48A^2T_1^8V_1^2 + 54ABT_1^5V_1 + 15B^2T_1^2 \\ &- 2\Delta^2P_1V_1 - \Delta^4) = 0. \end{aligned} \tag{E.11}$$

This is a polynomial equation in the variable T_2 and the root may be found in a straightforward fashion. Of course, equation (E.11) may have more than

one root so it is of interest to verify that any spurious roots lie in the unphysical region $T_2 < T_1$. (This region is unphysical since a shock can never lower the temperature; this would violate the second law of thermodynamics by decreasing the entropy.) In fact, spurious roots to equation (E.11) with $T_2 < T_1$ do exist.

Define the following dimensionless parameters

$$x = (T_2 - T_1)/T_1 \ , \tag{E.12}$$

$$\alpha = BT_1/AT_1^4V_1 \ , \tag{E.13}$$

$$\beta = \Delta^2/BT_1 \ . \tag{E.14}$$

Then equation (E.11) may be written as

$$f(x) = \sum_{i=0}^{9} a_i x^i = 0 \tag{E.15}$$

with

$$\begin{aligned}
a_9 &= 18\alpha \\
a_8 &= 6\alpha\beta + 192\alpha + 48 \\
a_7 &= 48\alpha\beta + 888\alpha + 384 \\
a_6 &= 9\alpha^2 + 168\alpha\beta + 2352\alpha + 1344 \\
a_5 &= 18\alpha^2\beta + 90\alpha^2 + 336\alpha\beta + 3984\alpha + 2688 \\
a_4 &= -7\alpha^2\beta^2 + 4\alpha^2\beta + 270\alpha^2 + 352\alpha\beta + 4416\alpha + 3264 \\
a_3 &= -28\alpha^2\beta^2 + 4\alpha^2\beta + 360\alpha^2 + 64\alpha\beta + 3024\alpha + 2304 \\
a_2 &= 15\alpha^3 - 42\alpha^2\beta^2 - 84\alpha^2\beta + 240\alpha^2 - 240\alpha\beta + 1056\alpha + 768 \\
a_1 &= -2\alpha^3\beta - 28\alpha^2\beta^2 - 88\alpha^2\beta - 224\alpha\beta \\
a_0 &= -\alpha^3\beta^2 - 4\alpha^3\beta - 8\alpha^2\beta^2 - 32\alpha^2\beta - 64\alpha\beta \ .
\end{aligned} \tag{E.16}$$

In the following argument the domain of x is restricted to $(0,\infty)$, corresponding to the physically permissible region $T_2 \geq T_1$. Now since both parameters α and β are positive it follows that the coefficients a_0 and a_1 are always negative whereas a_5 through a_9 are always positive. Since $a_9 > 0$ both $f(x)$ and $f'(x)$ (the derivative with respect to x) are positive for sufficiently large x, whereas clearly both $f(0)$ and $f'(0)$ are negative. Thus both $f(x)$ and $f'(x)$ have at least one root each. Label the roots of $f(x)$ sequentially from smallest to largest by $x_1, x_2, \ldots, x_n$; similarly label the roots of $f'(x)$ by $x_1', x_2', \ldots, x_m'$. Since a_0 and a_1 are negative, it follows that $x_1' < x_1$. Also, for any two roots of $f(x)$ there must be a root of $f'(x)$ between them (Rolle's Theorem), hence $m \geq n$.

Consider first the possibility $a_3 \geq 0$. Then $a_4 > 0$ since $a_4 > a_3/4$. Thus the third derivative $f'''(x)$ is positive definite, hence $f'(x)$ is concave upwards and has only one root ($m = 1$). Hence $n = 1$ and $f(x)$ has a unique root.

Consider now the case $a_3 < 0$, $a_2 < 0$. Since the fifth derivative $f^{v}(x)$ is positive definite then $f'''(x)$ is concave upwards and has only one root (since $f'''(0) < 0$). Then since $f''(0) < 0$, it follows that $f''(x)$ has only one root. Similarly, as a_0 and a_1 are negative it follows that both $f'(x)$ and $f(x)$ have unique roots.

Consider finally the case $a_3 < 0$, $a_2 \geq 0$. Necessary conditions for these two inequalities which follow simply from equations (E.16) are

$$\beta > 3.65 \qquad \text{(E.17)}$$

and

$$\alpha > 6\beta + 20 \,. \qquad \text{(E.18)}$$

Define

$$h(x) = a_2x^2 + a_1x + a_0 \quad , \tag{E.19}$$

$$g(x) = f(x) - h(x) \quad . \tag{E.20}$$

From these definitions along with the coefficients given by (E.16) the following implications may be derived:

$$h(x) \geq 0 \Rightarrow h(y) > 0 \quad , \quad \text{for all } y > x \quad ; \tag{E.21}$$

$$h(x) \geq 0 \Rightarrow h'(y) > 0 \quad , \quad \text{for all } y \geq x \quad ; \tag{E.22}$$

$$g(x) \geq 0 \Rightarrow g(y) > 0 \quad , \quad \text{for all } y > x \quad ; \tag{E.23}$$

$$g(x) \geq 0 \Rightarrow g'(y) > 0 \quad , \quad \text{for all } y \geq x \quad ; \tag{E.24}$$

$$g'(x) \geq 0 \Rightarrow g'(y) > 0 \quad , \quad \text{for all } y > x \quad ; \tag{E.25}$$

$$g'(x) \geq 0 \Rightarrow g''(y) > 0 \quad , \quad \text{for all } y \geq x \quad . \tag{E.26}$$

Assume $n \geq 2$. Then $m \geq 2$ and hence x_2' exists and $x_2' > x_1$. Thus

$$\begin{aligned} g(x_1) \geq 0 &\Rightarrow g'(x_1) > 0 \Rightarrow g'(x_2') > 0 \Rightarrow h'(x_2') < 0 \\ &\Rightarrow h'(x_1') < 0 \Rightarrow g'(x_1') > 0 \\ &\Rightarrow g''(x) > 0 \quad \text{for all } x \geq x_1' \\ &\Rightarrow g'(x_2') > g'(x_1') \\ &\Rightarrow h'(x_2') < h'(x_1') \\ &\Rightarrow h''(x) < 0 \quad \text{for some } x > x_1' \end{aligned} \tag{E.27}$$

But $a_2 \geq 0$ by assumption, hence $h''(x) = 2a_2 \geq 0$. Therefore $g(x_1) < 0$ and hence

$$h(x_1) > 0. \tag{E.28}$$

Now

$$h(x_1) > 0 \Rightarrow h'(x) > 0 \quad \text{for all } x \geq x_1$$

$$\Rightarrow h(x_2) > h(x_1)$$

$$\Rightarrow g(x_2) < g(x_1)$$

$$\Rightarrow g'(x) < 0 \quad \text{for some } x > x_1 \,. \tag{E.29}$$

Now by direct evaluation of $g'(x)$ and $h(x)$ using conditions (E.17) and (E.18) one finds:

$$h(\beta/3) < 0 \tag{E.30}$$

and

$$g'(\beta/3) > 0 \,. \tag{E.31}$$

Conditions (E.21), (E.28) and (E.30) imply $x_1 > \beta/3$, whereas conditions (E.25), (E.29) and (E.31) imply $x_1 < \beta/3$. Hence the assumption $n \geq 2$ is invalid for the case $a_3 < 0$ and $a_2 \geq 0$.

Thus the root of $f(x)$ is unique regardless of the values of the parameters α and β, hence one may solve equation (E.11) numerically without the danger of encountering a spurious root.

REFERENCES

Abramowitz, M., and Stegun, I.A. (1964), (eds.) Handbook of Mathematical Functions (New York: Dover) p. 377.

Allen, C.W. (1976), Astrophysical Quantities, third edition (London: Athlone) p. 197.

Alme, M.L., and Wilson, J.R. (1974), Ap. J. 194, 147.

Arnett, W.D. (1969), Ap. Space Sci. 5, 180.

Arnett, W.D. (1979), Ap: J. (Letters) 230, L37.

Arnett, W.D. (1982), Ap. J. 253, 785.

Ashworth, W. (1980), Bull. Am. Astron. Soc. 11, 660.

Axelrod, T.S. (1980), in Proceedings of the Texas Workshop on Type I Supernovae, ed. J.C. Wheeler (Austin: University of Texas) p. 80.

Baade, W. (1943), Ap. J. 97, 119.

Baade, W. (1945), Ap. J. 102, 309.

Baade, W., and Zwicky, F. (1934), Phys. Rev. 46, 76.

Barbon, R. (1980), in Proceedings of the Texas Workshop on Type I Supernovae, ed. J.C. Wheeler (Austin: University of Texas) p. 16.

Barbon, R., Chiatti, F., Rosino, L. (1973), Astron. Ap. 25, 241.

Becker, R.H., Holt, S., Smith, B.W., White, N.E., Boldt, E.A., Mushotzky, R.F., and Serlemitsos, P.J. (1980), Ap. J. (Letters) 235, L5.

Bethe, H.A. (1982) in Supernovae: A Survey of Current Research, ed. M.J. Rees and R.J. Stoneham (Dordrecht: Reidel) p. 13.

Biermann, P., and Tinsley, B.M. (1974), Pub. Astron. Soc. Pac. 86, 791.

Blair, W.P. (1982), in Supernovae: A Survey of Current Research, ed. M.J. Rees and R.J. Stoneham (Dordrecht: Reidel) p. 475.

Blandford, R.D. (1982), in Supernovae: A Survey of Current Research, ed. M.J. Rees and R.J. Stoneham (Dordrecht: Reidel) p. 459.

Branch, D. (1980a), in Supernova Spectra, ed. R. Meyerott and G.H. Gillespie (New York: American Institute of Physics) p. 39.

Branch, D. (1980b), in Proceedings of the Texas Workshop on Type I Supernovae, ed. J.C. Wheeler (Austin: University of Texas) p. 66.

Branch, D. (1981), Ap. J. 248, 1076.

Branch, D. (1982), in Supernovae: A Survey of Current Research, ed. M.J. Rees and R.J. Stoneham (Dordrecht: Reidel) p. 267.

Branch, D. (1985), in Supernovae as Distance Indicators, ed. N. Bartel (Berlin: Springer-Verlag) p. 138.

Branch, D., Lacy, C.H., McCall, M.L., Sutherland, P.G., Uomoto, A., Wheeler, J.C., and Wills, B.J. (1983), Ap. J. 270, 123.

Branch, D., and Tull, R.G. (1979), Astron. J. 84, 1837.

Brown, G.E. (1982), in Supernovae: A Survey of Current Research, ed. M.J. Rees and R.J. Stoneham (Dordrecht: Reidel) p. 13.

Bruenn, S.W. (1972), Ap. J. Suppl. 24, 283.

Buta, R., and Turner, A. (1983), Pub. Astron. Soc. Pac. 95, 72.

Chandrasekhar, S. (1931), Ap. J. 74, 81.

Chandrasekhar, S. (1939), An Introduction to the Study of Stellar Structure (Chicago: Dover) p. 389.

Chevalier, R.A. (1981), Ap. J. 246, 267.

Clark, D.H., and Stevenson, F.R. (1982), in Supernovae: A Survey of Current Research, ed. M.J. Rees and R.J. Stoneham (Dordrecht: Reidel) p. 355

Clayton, D.D. (1968), Principles of Stellar Evolution and Nucleosynthesis, (New York: McGraw-Hill).

Colgate, S.A., and McKee, C. (1969), Ap. J. 157, 623.

Colgate, S.A., Petschek, A.G., and Kriese, J.T. (1980), Ap. J. (Letters) 237, L81.

Colgate, S.A., and White, R.H. (1966), Ap. J. 143, 626.

Davidson, K., Gull, T.R., Maran, S.P., Stecher, T.P., Fesen, R.A., Parise, R.A., Harvel, C.A., Kafatos, M., and Trimble, V.L. (1982), Ap. J. 253, 696.

Dopita, M.A. (1982), in Supernovae: A Survey of Current Research, ed. M.J. Rees and R.J. Stoneham (Dordrecht: Reidel) p. 483.

Ergma, E.V., and Tutukov, A.V. (1976), Acta Astr. 26, 69.

Falk, S.W., and Arnett, W.D. (1977), Ap. J. Suppl. 33, 515.

Fugimoto, M.Y., and Sugimoto, D. (1982), Ap. J. 257, 291.

Fugimoto, M.Y., and Taam, R.E. (1982), Ap. J. 260, 249.

Glen, G., and Sutherland, P. (1980), Ap. J. 239, 671.

Harnden, F.R., Hertz, P., Gorenstein, P., Grindlay, J., Schreier, E., and Seward, F. (1979a), Bull. Am. Astron. Soc. 11, 424.

Harnden, F.R., Buehler, B., Giacconi, R., Grindlay, J., Hertz, P., Schreier, E., Seward, F., Tanabaum, H., and Van Speybroeck, L. (1979b), Bull. Am. Astron. Soc. 11, 789.

Helfand, D.J., and Long, K.S. (1982), in Supernovae: A Survey of Current Research, ed. M.J. Rees and R.J. Stoneham (Dordrecht: Reidel) p. 529.

Holm, A.V., Wu, C.-C., and Caldwell, J.J. (1974), Pub. Astron. Soc. Pac. 86, 296.

Hoyle, F., and Fowler, W.A. (1960), Ap. J. 132, 565.

Huebner, W.F., Merts, A.L., Mogee, N.H.Jr., and Argo, M.F. (1977), Astrophysical Opacity Library, Report #UC-346, Los Alamos Scientific Laboratory, unpublished.

Jeffery, D., and Sutherland, P. (1985), Ap. Space Sci. 109, 277.

Karp, A.H., Lasher, G., Chan, K.L., and Salpeter, E.E. (1977), Ap. J. 214, 161.

Kirshner, R.P., and Oke, J.B. (1975), Ap. J. 200, 574.

Kirshner, R.P., Oke, J.B., Penston, M.V., and Searle, S. (1973), Ap. J. 185, 303.

Landau, L.D., and Lifshitz, E.M. (1959), Fluid Mechanics, (Reading, Mass: Addison-Wesley).

Lasher, G. (1975), Ap. J. 201, 194.

Lasher, G. (1980), in Supernova Spectra, ed. R. Meyerott and G.H. Gillespie (New York: American Institute of Physics) p. 1.

Lederer, C.M., and Shirley, V.S. (1978), (eds.), Table of Isotopes, seventh edition (New York: Wiley).

Lyne, A.G. (1982), in Supernovae: A Survey of Current Research, ed. M.J. Rees and R.J. Stoneham (Dordrecht: Reidel) p. 405.

Maza, J., and van den Bergh, S. (1976), Ap. J. 204, 519.

Mazurek, T.J., and Wheeler, J.C. (1980), Fundamentals of Cosmic Physics, 5, 193.

Mihalas, D. (1978), Stellar Atmospheres, second edition (San Francisco: Freeman) p. 60.

Minkowski, R. (1938), Ap. J. 89, 156.

Minkowski, R. (1941), Pub. Astron. Soc. Pac. 53, 224.

Müller, E., and Arnett, W.D. (1982), Ap. J. (Letters), 261, L109.

Müller, E., and Arnett, W.D. (1984), MPA 108, Max-Planck Institut für Physik und Astrophysik (preprint).

Nomoto, K. (1982a), Ap. J. 253, 789.

Nomoto, K. (1982b), Ap. J. 257, 780.

Nomoto, K. (1984), in Proceedings of the Erice Conference on Stellar Nucleosynthesis, ed. C. Chiosi and A. Renzini (Dordrecht: Reidel).

Nomoto, K., Sugimoto, D., and Neo, S. (1976), Ap. Space Sci. 39, L37.

Nomoto, K., and Tsuruta, S. (1981), Ap. J. (Letters) 250, L19.

Oemler, A., and Tinsley, B.M. (1979), Astron. J. 84, 985.

Pskovskii, Y.P. (1977), Sov. Astron. 21(6), 675.

Rees, M.J., and Stoneham, R.J. (1982), (eds.) Supernovae: A Survey of Current Research (Dordrecht: Reidel).

Richtmeyer, R.D., and Morton, K.W. (1967), Difference Methods for Initial-Value Problems (New York: Wiley).

Saio, H. (1983), private communication.

Saio, H., and Wheeler, J.C. (1983), Ap. J. (Letters) 272, L25.

Salpeter, E.E. (1961), Ap. J. 134, 669.

Salpeter, E.E., and Van Horn, H.M. (1969), Ap. J. 155, 183.

Sandage, A., and Tamann, G.A. (1982), Ap. J. 256, 339.

Sandage, A., and Tanmann, G.A. (1985), in Supernovae as Distance Indicators, ed. N. Bartel (Berlin: Springer-Verlag) p. 1.

Schatzman, E. (1963), in Star Evolution, ed. L. Gratton (New York: Academic Press) p. 389.

Schurmann, S.R. (1983), Ap. J. 267, 779.

Seward, F.D. (1982), in Supernovae: A Survey of Current Research, ed. M.J. Rees and R.J. Stoneham (Dordrecht: Reidel) p. 519.

Shapiro, S.L., and Teukolsky, S.A. (1983), Black Holes, White Dwarfs, and Neutron Stars (New York: Wiley) p. 332.

Shull, J.M. (1982), Ap. J. 262, 308.

Sugimoto, D., and Nomoto, K. (1980), Space Science Review 25, 155.

Sutherland, P.G., and Wheeler, J.C. (1984), Ap. J. 280, 282.

Szymkowiak, A.E. (1980), in Proceedings of the Texas Workshop on Type I Supernovae, ed. J.C. Wheeler (Austin: University of Texas) p. 32.

Tamann, G.A. (1982), in Supernovae: A Survey of Current Research, ed. M.J. Rees and R.J. Stoneham (Dordrecht: Reidel) p. 371.

Tinsley, B.M. (1980), in Proceedings of the Texas Workshop on Type I Supernovae, ed. J.C. Wheeler (Austin: University of Texas) p. 196.

Twarog, B.A., and Wheeler, J.C. (1982), Ap. J. 261, 636.

Van Riper, K.A., and Lamb, D.Q. (1981), Ap. J. (Letters) 244, L13.

Weaver, T.A., Axelrod, T.S., and Woosley, S.E. (1980), in Proceedings of the Texas Workshop on Type I Supernovae, ed. J.C. Wheeler (Austin: University of Texas) p. 113.

Weiler, K.W., Sramek, R.A., van der Hulst, J.M., and Panagia, N. (1982), in Supernovae: A Survey of Current Research, ed. M.J. Rees and R.J. Stoneham (Dordrecth: Reidel) p. 281.

Wheeler, J.C. (1978), Ap. J. 225, 212.

Wheeler, J.C. (1980), in Proceedings of the Texas Workshop on Type I Supernovae, ed. J.C. Wheeler (Austin: University of Texas) p. 1.

Wheeler, J.C. (1981), Reports on Progress in Physics 44, 85.

Wheeler, J.C. (1982), in Supernovae: A Survey of Current Research, ed. M.J. Rees and R.J. Stoneham (Dordrecht: Reidel) p. 167.

Whelan, J., and Iben, I.Jr. (1973), Ap. J. 186, 1007.

Woosley, S.E., Weaver, T.A., and Taam, R.E. (1980), in Proceedings of the Texas Workshop on Type I Supernovae, ed. J.C. Wheeler (Austin: University of Texas) p. 96.

Zwicky, F., Berger, J., Gates, H.S., and Rudnicki, K. (1963), Pub. Astron. Soc. Pac. 75, 236.